Alma Mater Studiorum - Università di Bologna

Dipartimento di Fisica e Astronomia

Corso di Laurea Magistrale in Astrofisica e Cosmologia

Investigating the origin of radio emission from the intra-cluster bridge A399-A401

Tesi di Laurea

Presentata da:
Matteo Vincenzi

Relatore:
Prof. Franco Vazza

Correlatore:
Dott. Gianfranco Brunetti

Anno Accademico 2021/2022

Contents

Abstract

The study in the radio band of large scale structures, complemented by their formation and evolution, can lead the exploration of new frontiers on particle acceleration processes in the Cosmic Web and in our Universe. The largest gravitationally bound structures are galaxy clusters. However, the discovery of large filamentary structures connecting pairs of clusters of galaxies in a pre-merger state has left us wondering what the origin of this recently observed class of phenomena might be. They are usually referred to as radio bridges.

In this work, I will focus my effort on what may be the most prominent example of this new class of phenomena, a radio bridge that spans over the 3 Mpc scale connecting the clusters Abell 399 and Abell 401. The nature of this bridge may be of great relevance, since it could represent an initial portion of a Cosmic Web filament, that up until the recent LOFAR observations has remained undetected in the radio band. Therefore, understanding the mechanisms that generate the emission and properties of the population of particles that resides in the region can allow us to derive the properties of particle acceleration in a poorly explored density regime, in particular regarding the formation of structures, since Abell 399 and Abell 401 are two clusters in a pre-merger phase.

Mostly using a semi-analytical approach, my Thesis will focus on constraining the plausible mechanisms for the formation of this radio bridge, in particular by confronting different model's predictions on the Inverse Compton emission from this region, which up until now has remained undetected.

From the detection of synchrotron emission in the region of the bridge, I derive different models that revolve around the presence of a relativistic population of Cosmic Rays electrons (CRe), emitting in radio. These electrons can be accelerated to higher relativistic energies via Fermi I or Fermi II processes, if we assume them to undergo shock or turbulent (re-)acceleration respectively. In particular, if the acceleration model for the CRe population is a Fermi I (re-)acceleration by weak shocks, then we are considering a system in which the emission of the bridge is caused by the overlapping of multiple shocks along the line of sight.

My Thesis is mostly concerned about constraining whether a Fermi I model can describe the observed synchrotron emission from the bridge while, at the same time, estimating the Inverse Compton emission that falls under the observational limit associated with our current instrumental possibilities, thus justifying the undetection of the emission.

Of particular importance in my modelling are the roles of the magnetic field distribution and strengths, the spectral index of the electron population, and the fraction

of the volume that is responsible for the emission of synchrotron radiation, since they are closely linked parameters for the Fermi I (re-)acceleration model that are in a degeneracy. I will consider how different combinations of these parameters may produce a suitable Inverse Compton emission and under which combination the values for these parameters are likely or not.
All this considered, in this work I will use statistical magnetic field models of increasing realism to describe the 3D distribution of magnetic fields in the bridge volume, in a variety of volume filling factors. Then I will compute the Inverse Compton luminosities predicted by the different models, and I will confront them with current observational constraints to see if a weak shock (re-)acceleration model can describe the emission from the A399-A401 bridge or whether other scenarios are required to explain its observation. Among the most important findings of my work, from the unreasonably large values of magnetic fields and filling factors for shocks required for the Fermi I model not to exceed the available IC limits, it can be inferred that this model is unlikely to describe the emission from the bridge, and thus that other particle acceleration mechanisms should be at play here.
My Thesis work is organized as follows:

- In Chapter (1) I introduce the physical background of interest for this work, in particular I write about large scale structure formation, galaxy clusters, emission mechanisms in the Intra-Cluster Medium and Cosmic rays in large scale structures;

- In Chapter (2) I talk about the scientific case of radio bridges, their main characteristics and some of the attempted models used to describe them, with a particular interest for the A399-A401 bridge;

- In Chapter (3) I compute the Inverse Compton emission for the bridge A399-A401 produced by a Fermi I (re-)acceleration model under various combinations of magnetic field distribution, filling factor and radio spectral index;

- In Chapter (4) I report the results of my work and I give my final remarks on the likelihood of a Fermi I model being able to describe the emission from the bridge;

- In Appendix (A)-(B) I show two examples for the codes that I have created to produce the graphs in Chapter (3), where from this two examples some modifications to them would allow to reproduce the majority of the graphs seen in that Chapter.

Riassunto

Lo studio di strutture su larga scale nella banda radio, insieme alla loro formazione ed la loro evoluzione, può condurre all'esplorazione di nuove frontiere per i processi di accelerazione delle particelle nel Cosmic Web e nel nostro Universo. Le più grandi strutture gravitazionalmente legate sono gli ammassi di galassie. Tuttavia la scoperta di grandi strutture filamentari che connettono coppie di ammassi di galassie in una fase di pre-merger ci ha portato a interrogarci su quale potrebbe essere l'origine di questa nuova classe di fenomeni recentemente osservata. Sono di solito chiamati radio bridges.

In questo elaborato, concentrerò i miei sforzi su quello che potrebbe essere l'esempio più prominente di questa nuova classe di fenomeni, un ponte radio che si estende oltre i 3 Mpc connettendo gli ammassi Abell 399 e Abell 401. La natura di questo ponte potrebbe essere di grande importanza, visto che potrebbe essere una porzione iniziale di un filamento del Cosmic Web, un tipo di fenomeno che è rimasto invisibile nella banda radio fino a recenti osservazioni LOFAR. Perciò, capire i meccanismi che generano l'emissione e le proprietà delle popolazioni di particelle che risiedono in quella regione può permetterci di derivare le proprietà dell'accelerazione di particelle in quello che è un regime di densità scarsamente esplorato, in particolare riguardo alla formazione di strutture, visto che Abell 399 e Abell 401 sono due cluster in una fase di pre-merger.

Usando un approccio semi-analitico, il mio lavoro di Tesi si concentrerà sul vincolare il possibile meccanismo di formazione di questo radio bridge, in particolare confrontando le predizioni di differenti modelli con l'emissione Inverse Compton da questa regione, che fino ad oggi è rimasta inosservata.

Dall'osservazione dell'emissione di sincrotrone nella regione del bridge derivo diversi modelli riguardanti la presenza di una popolazione di Cosmic Ray electrons (CRe) relativistici, che emettono nel radio. Questi elettroni possono essere accelerati a più alte energie relativistiche tramite processi Fermi I o Fermi II, se assumiamo che vadano incontro a una (ri-)accelerazione tramite shock o turbolenta, rispettivamente. In particolare, se il modello di accelerazione per la popolazione di CRe è una (ri-)accelerazione Fermi I da shock deboli, allora stiamo considerando un sistema nel quale l'emissione dal bridge è causata dalla sovrapposizione di vari shock lungo la linea di vista.

La mia Tesi è principalmente focalizzata sul determinare se un modello Fermi I possa descrivere l'emissione di sincrotrone osservata dal bridge e se, allo stesso tempo, possa predire un'emissione Inverse Compton che sia al di sotto del limite osservativo associato con le nostre attuali possibilità strumentali, e dunque giustificando la sua

non detezione.
Di un'importanza particolare per i miei modelli sono i ruoli che rivestono la distribuzione e l'intensità dei campi magnetici, l'indice spettrale della popolazione e la frazione di volume responsabile per l'emissione di sincrotrone, siccome sono parametri strettamente collegati per il modello di (ri-)accelerazione Fermi I, per il quale sono in una degenerazione. Considererò come differenti combinazioni di questi parametri possano produrre un'adeguata emissione Inverse Compton e per quali combinazioni i valori di questi parametri siano plausibili o no.
Ciò detto, in questo elaborato userò modelli statistici di distribuzione dei campi magnetici che siano di crescente realismo, in modo da descrivere la distribuzione 3D dei campi magnetici nel volume del bridge, con una varietà di fattori di riempimento del volume totale. Poi calcolerò le luminosità Inverse Compton predette dai vari modelli e le confronterò con gli attuali vincoli osservativi per controllare se un modello di (ri-)accelerazione con shock deboli possa descrivere l'emissione dal bridge A399-A401 o se altri scenari siano richiesti per spiegare la sua osservazione.
Tra i risultati più importanti del mio lavoro, dagli elevati ed inspiegabili valori dei campi magnetici e dei fattori di riempimento che sono richiesti affinchè gli shock per il modello Fermi I non facciano eccedere i limiti Inverse Compton disponibili, è possibile evincere che sia improbabile che questo modello descriva l'emissione dal bridge e che dunque altri meccanismi per l'accelerazione delle particelle dovrebbero avere un loro ruolo nel bridge.
Il mio lavoro di tesi è organizzato come segue:

- Nel Capitolo (1) introduco il background fisico di interesse per questo elaborato, in modo particolare scrivo riguardo alla formazione di strutture su larga scale, ad ammassi di galassie, ai meccanismi di emissione nell'Intra-Cluster Medium e ai raggi cosmici in strutture su larga scala;

- Nel Capitolo (2) parlo del caso scientifico dei radio bridge, le loro principali caratteristiche e alcuni dei modelli con cui si è tentato di descriverli, con un interesse particolare per il bridge A399-A401;

- Nel Capitolo (3) calcolo l'emissione Inverse Compton per il bridge A399-A401 prodotta da un modello a (ri-)accelerazione Fermi I sotto varie combinazioni di distribuzioni di campi magnetici, fattori di riempimento e indice spettrale radio;

- Nel Capitolo (4) riporto i risultati del mio elaborato e fornisco i miei commenti finali sulla plausibilità che un modello Fermi I sia capace di descrivere l'emissione dal bridge;

- Nelle Appendici (A)-(B) mostro due esempi per i codici che ho ideato per produrre i grafici nel Capitolo (3), dove alcune modifiche a partire da questi due esempi permetterebbero di riprodurre la maggior parte dei grafici visti in quel Capitolo.

Chapter 1

Introduction

In this introduction I will give a quick review on the basic concepts of cosmology, and in particular the model Λ Cold Dark Matter (ΛCDM) and the nature of the Cosmic Web, of galaxy clusters and their characteristics and finally on the ICM, with a particular attention to particle acceleration models. In later Chapters, I will move on to study how exactly each model that may describe bridge A399-A401 withstands the comparison with our observational constraints.

1.1 Large scale structure formation

In all of my analysis I have assumed a cosmology of the model ΛCDM so a universe that has a flat geometry composed by dark matter, baryonic matter, radiation and dark energy. A universe of this kind is currently undergoing accelerated expansion because of the dominant presence of dark energy over the other components.
There are several fundamental cosmological parameters for which I have to assign a certain value to conduct this work, some of the most important ones are the Hubble constant $H(t) = \dot{a}/a$, where a is the expansion factor, and the density parameters for each component of the universe, represented by $\Omega = \rho/\rho_{crit}$, where ρ_{crit} is the critical value of density, a discriminant for whether or not our universe is open, closed or flat. When I want to express these quantities at the present time ($t = 0$) I can write them as a_0, H_0, Ω_0 and so on.
The difference between flat, open or closed geometry manifests, amongst other phenomena, into the measures of distance at cosmological scales, therefore making it extremely crucial to not only cosmological studies to discern in what type of universe we have found our home.
There are two very significant ways in which we can define distance, and those are luminosity [Eq. (1.1)] or angular [Eq. (1.2)] distance, as written in the equations below

$$d_L = a_0 r(1 + z) \tag{1.1}$$

that we obtain with standard candles, and

$$d_A = ar \tag{1.2}$$

that we obtain with standard rulers; since by definition $1 + z = a_0/a$, we have the duality relation $d_A/d_L = 1/(1 + z)^2$.
These distances differ in their results as a direct consequence from our use of the metric of Robertson-Walker-Friedmann (RWF), that we will not discuss here, and the duality relation is a strong test to check if we can indeed apply RWF to the entirety of the universe. In this work I use luminosity distances, even if the bridge A399-A401 is close enough to us such that no major difference would occur.
For consistency with the discovery paper by F. Govoni and al. (2019), the cosmological parameters chosen for this work are:

- $H_0 = 72\ km\ s^{-1} Mpc^{-1}$,
- $\Omega_{0,m} = 0.258$
- $\Omega_{0,\Lambda} = 0.742$

while the redshifts of A399 and A401 are respectively 0.071806 and 0.073664 (F. Govoni and al. 2019).

1.1.1 Structure formation and growth

The consensus view of structure formation in an evolving universe is that a hierarchical model of galaxy and galaxy cluster formation, that means to assume that small perturbations in the dark matter field of density grow at a certain pace, creating potential wells that in turn facilitate the accretion of perturbation of barionic matter, inside these pre-existing wells, forming the various structures of our universe. In particular, a hierarchical scenario states that small objects and structures are the first things formed and then via merger bigger and bigger structures are formed, like galaxies and clusters of galaxies. Each kind of component of the universe grows in a different way at different rates, and those same ways vary accordingly to which epoch we are considering. Here I give a quick overview of what are the main behaviours of each component in different time periods, specifically: before the equivalence ($t < t_{eq}$), between the equivalence and decoupling ($t_{eq} < t < t_{dec}$) and after decoupling ($t > t_{dec}$). For each of these periods I consider spatial scales bigger than the horizon ($\lambda > R_H$) and between the horizon and Jeans scale ($R_J < \lambda < R_H$), that are the only ones that allow a perturbation to grow.
If $\delta = \delta\rho/\bar{\rho}$ represents a general perturbation in a density field then with δ_B, δ_R and δ_{DM} we are considering the perturbations in the density fields of baryons, radiation and dark matter, respectively. In Tab. (1.1) I display the trends of each component.

Table 1.1: Perturbation growth of various cosmological components

	$t < t_{eq}$	$t_{eq} < t < t_{dec}$	$t > t_{dec}$
$\lambda > R_H$	δ_B,δ_R,δ_{DM} α a^2	δ_B,δ_R,δ_{DM} α a	δ_B,δ_R,δ_{DM} α a
$R_J < \lambda < R_H$	δ_R oscillates δ_B oscillates δ_{DM} stagnates	δ_R oscillates δ_B oscillates δ_{DM} α a	δ_{DM} α a, $\delta_B = \delta_{DM}(1 - \frac{a_{dec}}{a})$

I am particularly interested in what happens after the decoupling time of matter and radiation, since before that time matter and radiation perturbations could not grow but instead oscillated, so they simply propagated through space without increasing in amplitude. The role of dark matter is important because before the equivalence its perturbations could not grow indefinitely but between t_{eq} and t_{dec} they were the only ones able to grow proportionally to $a(t)$, therefore creating potential wells into which baryons, after decoupling, could fall into; in fact, their trend after decoupling is called *baryon catch up* since baryon perturbations rapidly catch up to the dark matter ones, allowing the formation of galaxies and their later on evolution and merging processes that will result in clusters of galaxies.

1.1.2 Cosmic web

How exactly perturbations form and then grow in their non-linear stage is best modelled by the means of cosmological simulations, nonetheless the majority of them results in a pattern of nodes and filaments commonly called *Cosmic Web*, shown in Fig. (1.1).

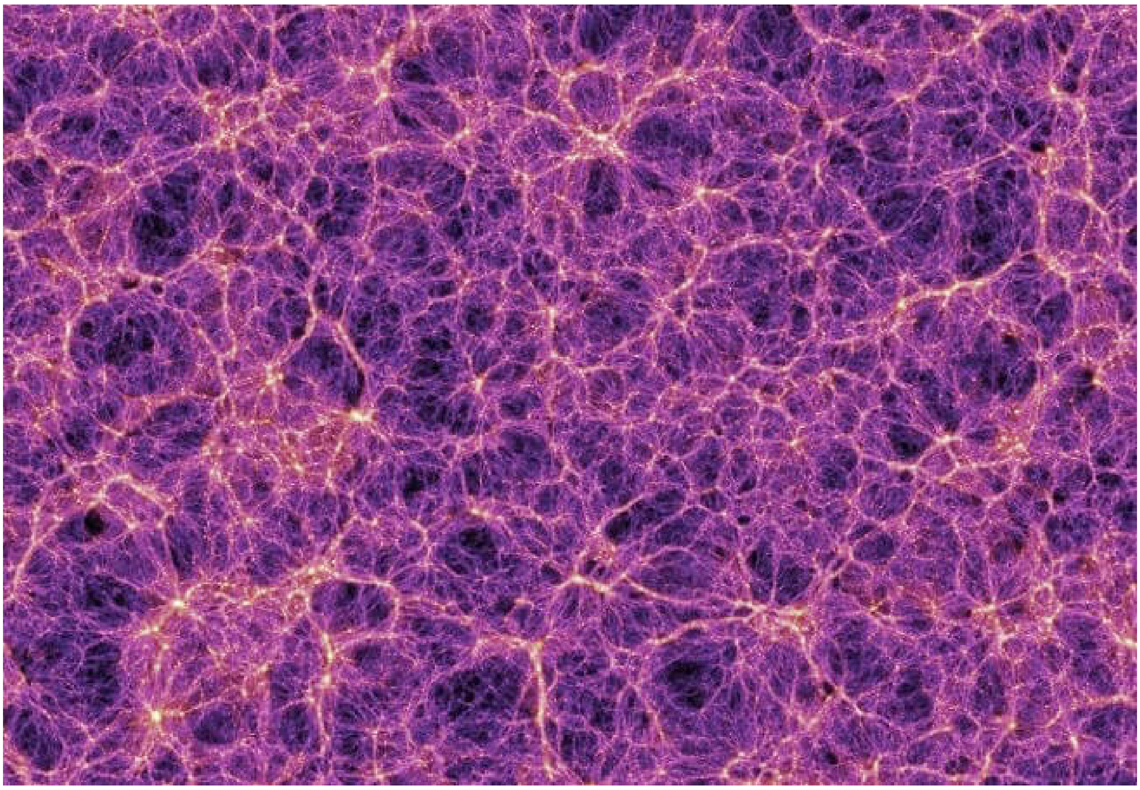

Figure 1.1: Cosmic web; Credit: V.Springel, Max-Planck Institut für Astrophysik;

Every node in the cosmic web represents a cluster of galaxies, while the filaments joining them are composed by gas and galaxies. The usual finding is that dark matter potential wells form fist, thus causing filaments of dark matter, and then barionic matter falls into the pre-formed filaments leading to the formation of structures.
There are many ways to describe the evolution of perturbations, meaning also how

the Cosmic Web comes to be, in particular it is important to consider a non linear regime of perturbations, so when δ in not much less than 1; in this regime there are analytical theories in weakly non linear regimes, Gaussian's peak theory, Zel'Dovich's approximation and cosmological simulations. The last ones obviously require significant time and computational power, yet they can address in a better way the need to deal with several bodies interacting with each other, and occasionally colliding when a merger event happens.
It is of particular interest to us the concept of Cosmic Web, since A399-A401 could possibly be the tip of the iceberg of the filamentary distribution of gas matter and magnetic fields in the Cosmic Web, and it would be one of the first to be observed in radio and measured in its quantities. There are however more recent detection of Cosmic Web filaments, that we can see in Fig. (1.2)-(1.3), that have been obtained via different routes.

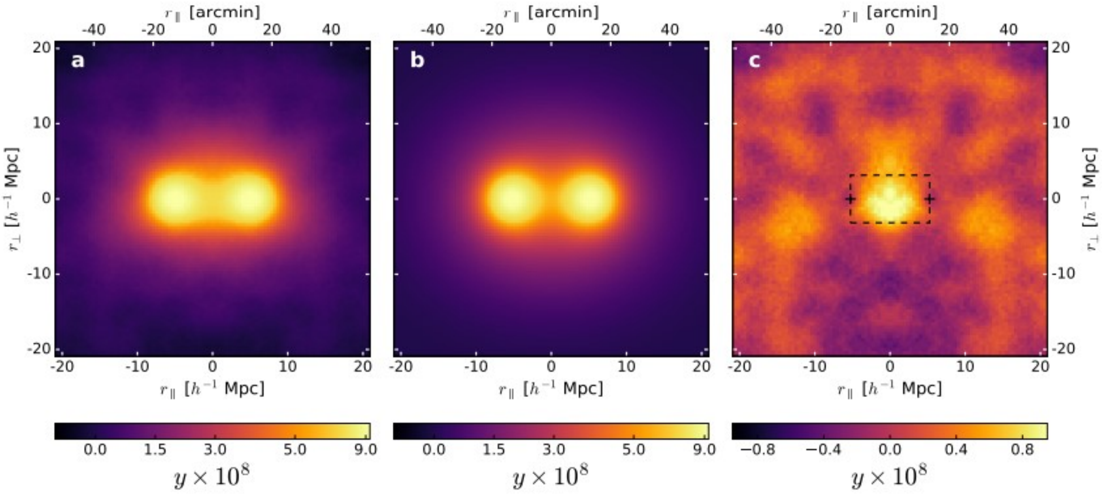

Figure 1.2: In the left panel the data obtained from the stacking of millions of close pairs of galaxies; in the middle panel the model for said pairs, which does not have the bridge present in the left panel; in the right panel the observed filament is highlighted; (A. de Graaff and al. 2019)

In Fig. (1.2) there is an example of a detection of a Cosmic Web statistical filamentary emission through stacking of the *Planck* Compton-y map of the thermal Sunyaev-Zel'Dovich effect for several pairs of galaxies; in particular, this has allowed to find that up to $28 \pm 12\%$ of the missing baryon fraction in the universe might be found in Cosmic Web filaments (A. de Graaff and al. 2019).
A similar result was obtained through X-ray stacking of Chandra, ROSITA and XMM-Newton data for stacking of 15165 filaments already identified by SDSS where emission at significance 4σ was observed around 1 keV (H. Tanimura and al. 2020).
In Fig. (1.3) I show the difference in count-rate for the stacked data and an average profile from random sampling; we can easily see that the presence of filaments appears necessary to explain the differences between data and simulations.
Radio stacking of red galaxies as tracers for cluster pairs has also been attempted, however the radio signal is higher than the predictions from cosmological simulations, indicating that the filaments have sufficient CR and magnetic field strength

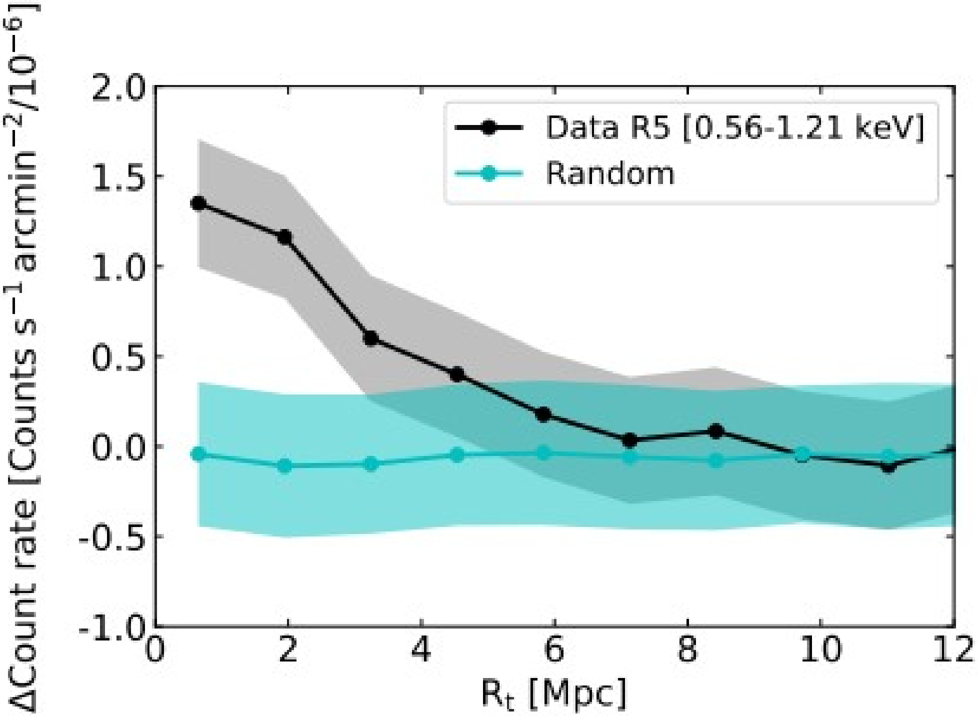

Figure 1.3: In black the average radial profile of stacked filaments in the ROSAT band $0.56 - 1.21\ keV$; in blue the average radial profile of 1000 random sampling (H. Tanimura and al. 2020);

to produce detectable synchrotron radiation (T. Vernstrom and al. 2021).

1.2 Galaxy clusters

Galaxy clusters are the biggest gravitationally bound structures in the universe and they are thought to be formed when several galaxies reach virial equilibrium, together with the gas surrounding them. Clusters of galaxies are composed of many galaxies, mainly elliptical, hot thermal gas called Intra-Cluster Medium (ICM), Cosmic Rays (CR) and dark matter.
The main characteristics of galaxy clusters typically consist in:

- 100-1000 galaxies
- velocity dispersion of 1000 km/s
- $1 - 5\ Mpc$ scale
- crossing time-scale $\approx 1\ Gyr$, implying plenty of mergers between its galaxies have taken place
- $10^{14} - 10^{15}\ M_{\odot}$

where the typical mass ratios are $1-5\%\ M_{tot}$ for galaxies, $10-16\%\ M_{tot}$ for the ICM and $84-90\%\ M_{tot}$ for dark matter, making galaxy clusters some of the best probes to study dark matter via gravitational lensing. They are also excellent cosmological probes because they allow us to track how matter is distributed in the universe (A. Cimatti 2020).

1.2.1 Optical, X-ray and radio observations

Observations in various bands have been performed, and here I show only a few examples of how galaxy clusters appear at different wavelengths. Galaxies mainly emit in the optical band, as seen in Fig. (1.4), however they are not the main baryonic components of the clusters, that would be the ICM. We can therefore study with optical observations stellar formation, scale relations, distribution and mass of galaxies, amongst other applications. To look at the ICM we have to observe the

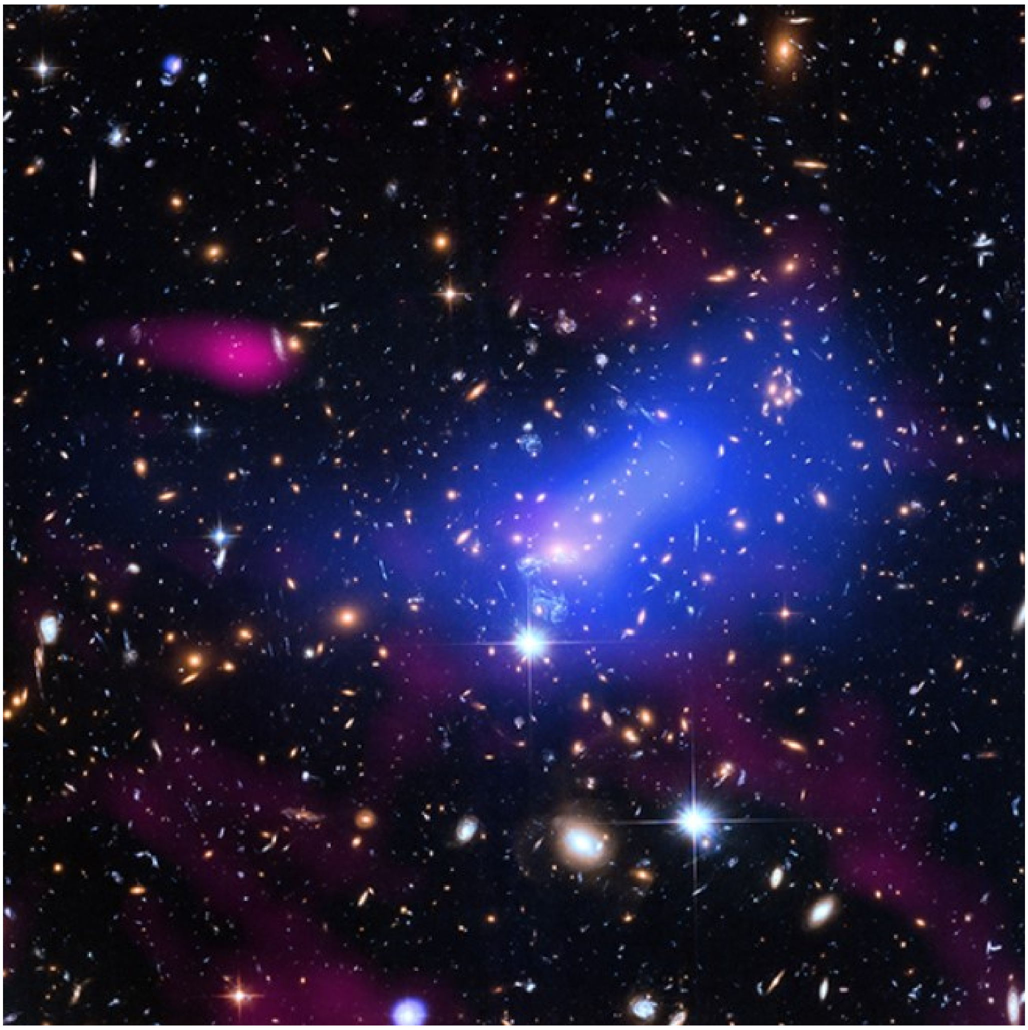

Figure 1.4: Galaxy cluster MACS J1149.5+2233; this image is the combination of X-ray (blue), optical and radio (red) observations (Credit: X-ray: NASA/CXC/SAO; Optical: NASA/STScI; Radio: NSF/NRAO/AUI/VLA)

clusters in the X band, this way we can study it through bremsstrahlung emission (free-free), recombination (free-bound), line emission (bound-bound) and IC. In particular, gas in the ICM has typical temperatures of $10^7 - 10^8$ K that are reached by gravitational and shock heating, while the CR component is non-thermal and it is made of relativistic electrons (CRe) and protons (CRp), however the presence of CRp in the ICM is not clear as the γ-rays produced as a byproduct of hadronic decay of said CRp have yet to be observed, with an hypothesized upper limit of roughly a percentage of the thermal energy of the ICM (G. Brunetti and T. W. Jones 2014).

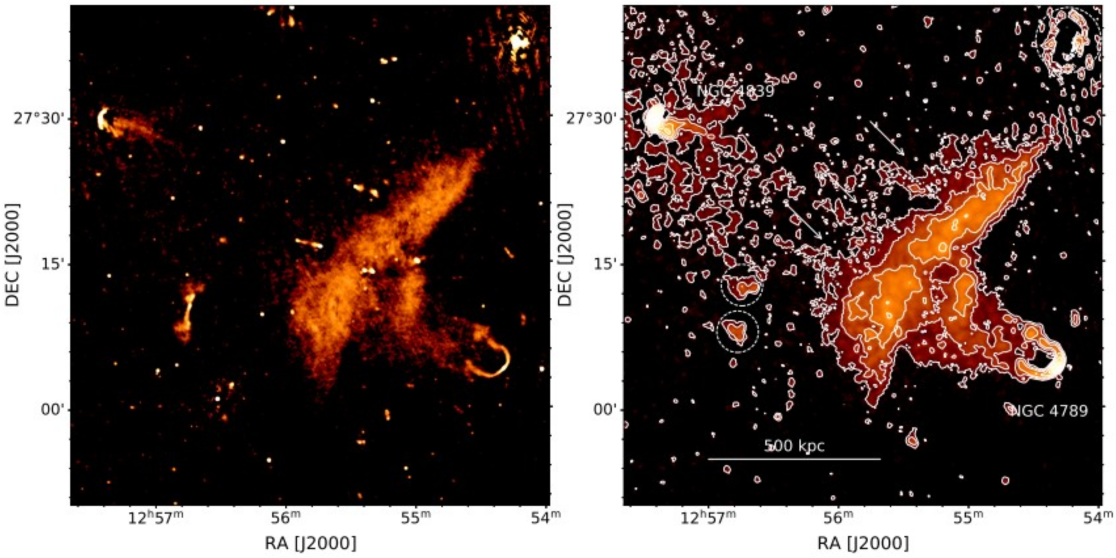

Figure 1.5: Radio relic in Coma cluster, where the white contours are at $3\sigma_{rms}$ (A. Bonafede and G. Brunetti 2022).

In the radio band we can study how CR populating the ICM behave, especially when we have synchrotron emission, since it allows us to inquire about the magnetic fields that fill the region and influence the dynamics of the ICM and CRe. Also we look at radio halos, radio relics and occasionally radio jets from AGN. All of these different phenomena can span the sky at spatial scales comparable to the cluster scale itself. The main source of emission is synchrotron radiation and this may include radio lobes caused by AGN jets interacting with the ICM and CRe interacting with the magnetic fields that fill the region of the cluster, amongst the various other sources. The latter are particularly interesting to this work because CRe emitting in synchrotron should also emit in IC, therefore giving us a way to double-check the origin of the radiation of the bridge A399-A401 and the nature of magnetic fields in the region; the CRe are likely already relativistic and they may reach even higher energies via shock (re-)acceleration and turbulence in the ICM, also these processes likely contribute to an amplification of magnetic fields, that can roughly be of the magnitude of the μG.

A radio halo is a class of diffuse radio emission located in the center of the cluster, mainly filling the same space of the ICM, where particle (re-)acceleration is likely due to the mechanisms spatially distributed over the ICM and it can be associated with turbulent re-acceleration or the production of secondary CRe due to the decay of primary CRe through what is called the hadronic mechanism. Radio relics are extended radio sources with a power-law spectrum and highly polarized emission that are likely the aftermath of a merger between clusters. They are often symmetrical to the merger axis with two radio relics parallel to the equatorial plane and two following ones perpendicular to it. In Fig. (1.5) we may see an example of a radio relic in the famous Coma cluster, showing the elongated shape of the structure.

1.2.2 Scaling relations for galaxy clusters

Figure 1.6: Bullet cluster; in blue is where the mass of the two clusters is concentrated, in pink is where the ICM (or baryonic mass in general) is; Credit: X-ray: NASA/CXC/CfA/M.Markevitch et al.; Optical: NASA/STScI; Magellan/U.Arizona/D.Clowe et al.; Lensing Map: NASA/STScI; ESO WFI; Magellan/U.Arizona/D.Clowe et al.

Galaxy clusters are the biggest virialized structures in the universe, this means that after billions of years the merging process occurring between the ensemble of galaxies has led the system to reach an approximate virial equilibrium, a balance between gravity and pressure due to the velocity dispersion of galaxies, as given by Eq. (1.3)

$$M = \frac{3\sigma_v r_g}{G} = 10^{15}\ (\frac{\sigma_v}{1000\ km/s})^2\ (\frac{r_{vir}}{1\ Mpc})\ M_\odot \tag{1.3}$$

where σ_v is the velocity dispersion of galaxies and r_{vir} the virial radius. However, the use of the virial theorem is but one of the methods with which it can be possible to measure the mass of a cluster, the others use the hydrostatic equilibrium between the X-ray and SZ emission of the ICM and the gravitational lensing (A. Cimatti 2020). That being said, Eq. (1.3) tells us that a typical value for the mass of a cluster is of the order of $10^{15}\ M_{\odot}$, which can only be explained with a significant presence of dark matter, if the hypothesis of virial equilibrium stands. A simple check that might be done is the measurement of the mass of the cluster with gravitational lensing; a test that up until now has been consistent with the presence of dark matter.
The hydrostatic equilibrium is another important relation to keep in mind, in fact by assuming it we can estimate the mass of the ICM and we can also define a gradient in temperature and density of the gas.
Assuming hydrostatic equilibrium allows us to define also a gradient in mass, as expressed in Eq. (1.4)

$$M(r) = \frac{k_b}{G\mu m_H}\frac{r^2}{\rho}(-T\frac{d\rho}{dr} - \rho\frac{dT}{dr}) \tag{1.4}$$

where μ is the chemical potential of the gas, m_h the mass of hydrogen and $\rho(r)$ and $T(r)$ are, respectively, the density and the temperature of just the ICM gas, excluding the dark matter component, obtained by observing the cluster in the X-ray band. The gas is colder in the center of the cluster than in its outskirts for $cool - core$ clusters, and viceversa for $non - cool - core$ clusters.
Density gradients for barionic and dark matter are more difficult to measure, in fact not being able to see directly the dark matter component is, of course, a grave obstacle; however, various models and simulations have been proposed, like NFW or Einasto or King, even if the occurrence of a merger between clusters greatly complicates the picture, take for example the Bullet cluster, in Fig. (1.6).
The stark contrast between the distribution of baryonic matter and matter in general, measured with gravitational lensing, makes clear that the majority of the mass in a cluster of galaxies is dark, and that in a merger event like the Bullet cluster the distribution of matter cannot be inferred by observing only ordinary matter but it is necessary to account for the predominant presence of dark matter.
However, we show here, in Eq. (1.5), NFW's model, as it is one of the most simple models to describe a dark matter halo and it can give us an understanding on what is the general distribution of cold dark matter when virialized and assumed non-collisional, in a cluster

$$\rho(r) = \frac{4\rho_s}{(\frac{r}{r_s})(1+\frac{r}{r_s})^2} \tag{1.5}$$

where ρ_s and r_s are scale quantities for each dark matter halo. This model is characterized by a central density cusp and is fit to describe clusters of galaxies, while at smaller scales gravitational lensing measures seem to find it more lacking (A. Cimatti 2020).

1.2.3 ICM

The gas constituting the ICM is perhaps the most ideal plasma that may be found in Nature, since it is so rarefied that it can be considered almost perfectly collisionless.

For a system to be collisionless it must be that all of its dynamics' time-scales are less then or of the same magnitude of the relaxation time-scale of the system, defined as the time-scale necessary for the system to become virialized, written in Eq. (1.6)

$$t_{relax} \approx \frac{0.1N}{lnN} t_{cross} \tag{1.6}$$

where N is the number of particles of our system and $t_{cross} = R/\sigma_v$ is the crossing time-scale of the system, with σ_v being in our case the velocity dispersion of particles in the ICM (J. Binney and S. Tremaine 2008). After one relaxation time the system has no memory of the initial conditions and its particles are subjected to a smooth gravitational potential, rather than one generated by a collection of mass points (ibidem).

The ICM is an almost perfect gas ionized plasma and this means that it is an electrically conductive gas fluid with mean-free-path $l_v = 1/(n\sigma_v)$, where n is the density of the absorbing medium into which the particle travels (G. B. Rybicki and A. P. Lightman 1985). Being collisionless, the ICM does not have many events of this kind, except maybe in shock events, allowing us to see the ICM primarily by other types of emissions, like bremsstrahlung, IC and synchrotron, that we will see later on in this introduction. However, due to the effects of the magnetic field on the particles, the ICM becomes weakly collisional, meaning that collisions between particles happens through the collective mediation of the plasma; magnetic fields also inhibit heat conduction, mixing of gas, propagation of CR and other transport processes (R. J. van Weeren and al. 2019). I will talk more about magnetic fields, in particular the methods used to estimate them, in later paragraphs.

1.3 Thermal and non-thermal observables of the ICM

A399-A401 was first found because of an excess in Sunyaev-Zel'Dovich radiation in the region and then synchrotron radiation was observed with LOFAR, however it is not the only phenomena that might interest us in this region (Planck Collaboration and al. 2012). IC emission is the other main one, with bremsstrahlung, however it is also worth to talk about Faraday Rotation as it is strictly related to in-situ magnetic fields.

In this Section, I will give a quick overview on what may be the main emission mechanisms in the ICM, as they are also likely to play a role in the production of emission in the bridge A399-A401. Bremsstrahlung emission has not been observed in the region, however, for completeness I report its main characteristics, while Faraday rotation has been used to estimate the strength of magnetic fields in the bridge.

1.3.1 Bremsstrahlung (or free-free) emission

Bremsstrahlung emission, or breaking or free-free emission, happens when unbound charged particles undergo a deceleration due to the presence of other charged particles in the nearby region. Depending on the regime in which we are we may study

bremsstrahlung radiation only with classical effects or with quantistic effects.
Let us first consider the case of an electron with charge e moving inside the Coulomb field of an ion with charge Ze, as represented in Fig. (1.7),

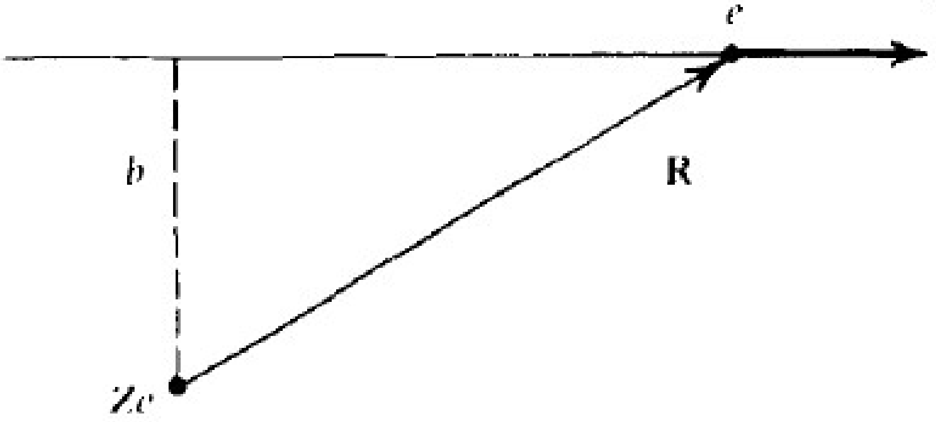

Figure 1.7: Electron moving inside the Coulomb field of an ion (G. B. Rybicki and A. P. Lightman 1985);

where b is the *collision parameter*, useful in order to define the collision timescale $\tau = b/v$. This configuration implies an acceleration $\vec{a} = -e\vec{E}/m_e$ on the electron, which it can be inserted inside Larmor's equation and in turn produce the expression for bremsstrahlung radiation in Eq. (1.7)

$$\frac{dE}{dt} \approx \frac{Z^2 e^6}{24\pi^3 \epsilon_0^3 c^3 m_e \hbar} ln(\frac{b_{max}}{b_{min}}) \tag{1.7}$$

where b_{max} and b_{min} are, respectively, the maximum and the minimum collision parameter of the system. Eq. (1.7) is an approximated equation at low frequencies, as it has a simpler notation and it is not our purpose to define in detail this type of radiation; at high frequencies energy losses have an exponential decrement with frequency. The first one is rather difficult to define, as it is arbitrary to decide where the influence of the ion is negligible on the electron, however it is of the order of v/ω so we will assign b_{max} that value. On the other hand, b_{min} is the maximum value between its classical or quantistic definition. In particular in Eq. (1.8)

$$b_{min,c} = \frac{Ze^2}{8\pi\epsilon_0 m_e v^2} \tag{1.8}$$

we see the form b_{min} takes when classical orbit's physics has a predominant role, while Eq. (1.9)

$$b_{min,q} = \frac{\hbar}{2m_e v} \tag{1.9}$$

ought to be used when the uncertainty principle becomes more relevant.
A combination of b_{max} and b_{min} can be seen in Eq. (1.10), and it results in a parameter

$$g_{ff} = \frac{\sqrt{3}}{\pi} ln(\frac{b_{max}}{b_{min}}) \tag{1.10}$$

called Gaunt factor, which depends on the energy of the electrons and frequency of emission, crucial to define the time-scale of losses (G. B. Rybicki and A. P. Lightman 1985).

If we want to consider a stream of electrons, we may describe it as having a maxwellian distribution of velocities that, when taken into account, provides energy losses, of the form shown in Eq. (1.11)

$$\frac{dE}{dt} \approx Z^2 N N_e \bar{g_{ff}} T^{1/2} \tag{1.11}$$

where $\bar{g_{ff}} = 1.2$ is the mean value of the Gaunt factor over all frequencies and for which we only showed the general behaviour, that being that free-free losses scale with the square root of the temperature of the gas.

Therefore, as written in Eq. (1.12), we can find that the cooling time for bremsstrahlung emission is approximately

$$t_{cool} \approx \frac{6\ 10^3}{n_e \bar{g_{ff}}} T^{1/2}\ yrs \tag{1.12}$$

in a classical regime.

However, the CR in the ICM move at relativistic speeds, making it worthwhile to analyse what is the behaviour of free-free emission when we find ourselves in a relativistic regime. In particular, Eq. (1.13) shows the behaviour of free-free losses in this regime

$$\frac{dE}{dt} \approx Z^2 n_e n_i \bar{g_{ff}} T^{1/2} (1 + 4.4 \times 10^{-10} T) \tag{1.13}$$

where the second term in inside the brackets is a relativistic correction to the classical expression of free-free energy losses (G. B. Rybicki and A. P. Lightman 1985). Roughly, the general behaviour between the two regimes is the same, given the general temperatures of ICM, although the relativistic correction may become more relevant for CRe.

1.3.2 Synchrotron emission

When a particle is deflected by a magnetic field at relativistic energies it also loses energy via synchrotron radiation; it is of particular interest for this work since it is the kind of emission that was seen in the region of the bridge A399-A401.

If we have a uniform magnetic field $\vec{B}$, an electron motion follows the relation in Eq. (1.14)

$$\frac{d}{dt}(\gamma m \vec{v}) = -\frac{e}{c} \vec{v} \times \vec{B} \tag{1.14}$$

where γ is the common relativistic factor. If we separate the components of the velocity in one that is parallel to $\vec{B}$ ($v_{//}$) and one that is perpendicular to it ($v_\perp$), we find that the modules of them both are constant but, in addition, $v_\perp$ also suffers a uniform acceleration normal to it. Therefore, the motion of relativistic electrons inside a magnetic field is that of a spiral, where the parallel component to $\vec{B}$ is a uniform rectilinear motion and where the perpendicular component to $\vec{B}$ is a uniform circular motion. In Fig. (1.8) we can see a diagram for this particular motion.

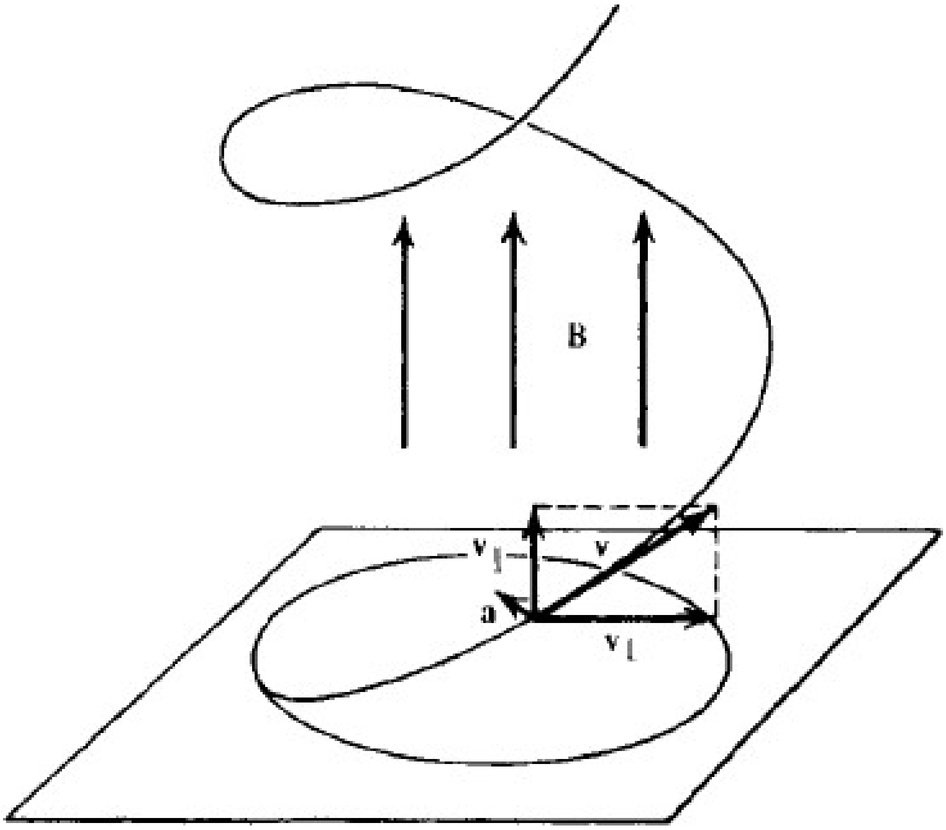

Figure 1.8: Electron moving in a uniform magnetic field (G. B. Rybicki and A. P. Lightman 1985);

The emitted power [Eq. (1.15)] resulting from this motion is

$$\frac{dE}{dt} = \frac{2}{3} r_0^2 c\beta \perp^2 \gamma^2 B^2 \tag{1.15}$$

but if we consider an isotropic distribution of velocity than it is necessary to integrate between all possible pitch angles α, thus resulting in an emitted power in the form of Eq. (1.16)

$$\frac{dE}{dt} = \frac{4}{3} \sigma_T c \beta^2 \gamma^2 U_B \tag{1.16}$$

where σ_T is the Thomson cross-section and $U_B = B^2/(8\pi)$ is the magnetic energy density (G. B. Rybicki and A. P. Lightman 1985). It is also possible to define a critical frequency [Eq. (1.17)] such that

$$\nu_c = \frac{3}{4\pi} \gamma^3 \omega_B sin\phi \tag{1.17}$$

where ϕ is the pitch angle between the magnetic field and the velocity of the particle, and $\omega_B = -\frac{e\vec{B}}{\gamma mc}$ is the pulsation of rotation. This critical frequency marks the point after which the spectrum tends to fall away.

We can extend this concept for a population of non-thermal electrons, for which Eq. (1.18) shows their distribution

$$N(E)dE = kE^{-\delta}dE \tag{1.18}$$

where k is a simple numerical constant depending on the entity of the population and δ defines the particle index of the population and it lets us define $\alpha = (\delta - 1)/2$, the radio spectral index, that it is in the form of a power law too if the population is homogeneous and isotropic. In Eq. (1.19) we show the intensity spectrum $I(\nu)$

$$I(\nu)d\nu = k\nu^{\alpha}d\nu \tag{1.19}$$

that when $\nu < \nu_c$ it has a spectral slope of 5/2 and when instead it has $\nu > \nu_c$ it has a spectral slope α as above mentioned, the latter being the case more fitting for the spectral band in which the region of the bridge has been observed.
Synchrotron radiation is polarized and we can measure the entity of its polarization

$$\Pi(\delta) = \frac{\delta + 1}{\delta + \frac{7}{3}} \tag{1.20}$$

with the polarization parameter in Eq. (1.20), which depends on the population of electrons via the particle index and can reach up to 70% (M. S. Longair 2011).
The cooling time-scale [Eq. (1.21)], which is the time needed for a system to emit all of its energy through a certain emission mechanism, for synchrotron emission is

$$t_{cool} \approx \frac{7.75\ 10^8}{B^2\gamma}\ s \tag{1.21}$$

with B expressed in Tesla, and the usual presence of IC emission in the same region may quicken the losses.

1.3.3 Inverse Compton emission

An event of inelastic collision between a photon and a stationary particle is called *Compton scattering*; this happens when the energy E of the photon is of the same order of magnitude of the rest energy m_ec^2 of the particle, that here we will assume for simplicity to be an electron. Fig. (1.9) gives us a diagram to describe the collision where E and E_1 (ϵ and ϵ_1 in Fig. (1.9)) represent the energy of the incoming photon and the scattered energy of that same photon, and where θ is the scattering angle. In Eq. (1.22) we show how the wavelength of the photon changes with this scattering

$$\lambda - \lambda_0 = \frac{h}{m_ec}(1 - cos\theta) \tag{1.22}$$

in particular, this process always causes a loss of energy for the photon and in Eq. (1.23) we can see how exactly its energy changes

$$E_1 = \frac{E}{1 + \frac{E}{m_ec^2}(1 - cos\theta)}. \tag{1.23}$$

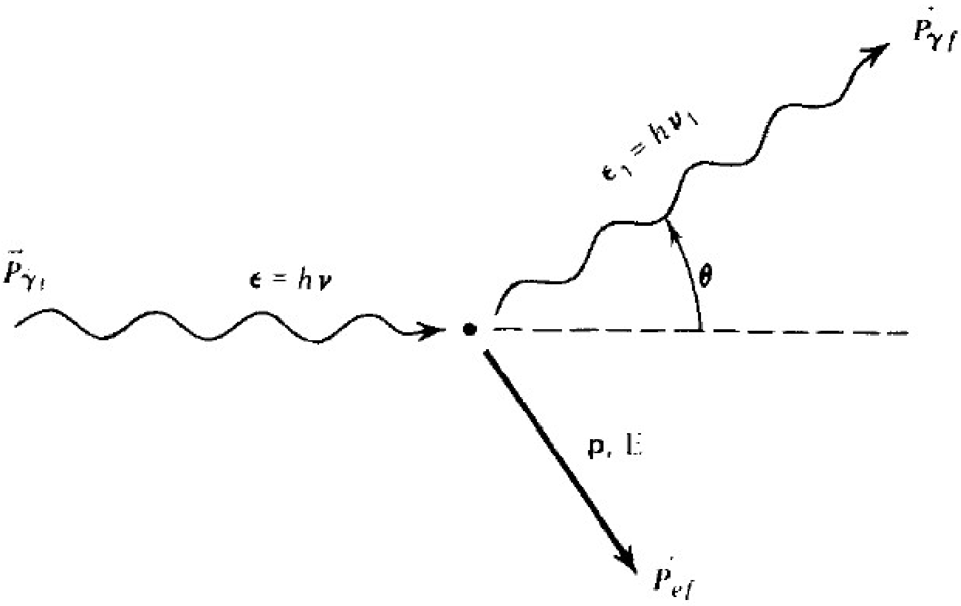

Figure 1.9: A photon and a stationary electron colliding (G. B. Rybicki and A. P. Lightman 1985);

The cross-section for this process is in Eq. (1.24)

$$\sigma_{K-N} = \pi r_e^3 \frac{1}{x}\{[1 - \frac{2(x+1)}{x^2}]ln(2x+1) + \frac{1}{2} + \frac{4}{x} - \frac{1}{2(2x+1)}^2\} \tag{1.24}$$

that is Klein-Nishima cross-section, with $x = \hbar\omega/(m_e c^2)$, that for $x << 1$, so for low energy photons, tends to the Thomson cross-section σ_T (M. S. Longair 2011).
Inverse Compton scattering happens when the energy of the photon is much smaller than that of the particle, because of this it is a phenomenon that usually interests populations of relativistic electrons scattering with a low energy photon field, like CRe, with energies of the order of GeV, in the ICM colliding with CMB photons, with energies of the order of $10^{-4}eV$.
Fig. (1.10) shows how the scattering process takes place in the observer rest frame and the rest frame of the electron.
The scattering in this process still causes a loss of energy in the photon, however the Doppler effect that the photon undergoes twice

$$E' = E\gamma(1 - \beta cos\theta) \tag{1.25}$$

before the scattering and

$$E_1 = E_1'\gamma(1 + \beta cos\theta_1') \tag{1.26}$$

after the scattering, it causes the gains to be much more than the losses (G. B. Rybicki and A. P. Lightman 1985). By substituting Eq. (1.23) in Eq. (1.26) and combining Eq. (1.25)-(1.26) we can see that the scattered photon energy increases by a factor γ^2, reaching even high X-ray energies.
The resulting power spectrum for IC emission [Eq. (1.27)] is

$$\frac{dE}{dt} = \frac{4}{3}\sigma_T c\beta^2\gamma^2 U_{rad} \tag{1.27}$$

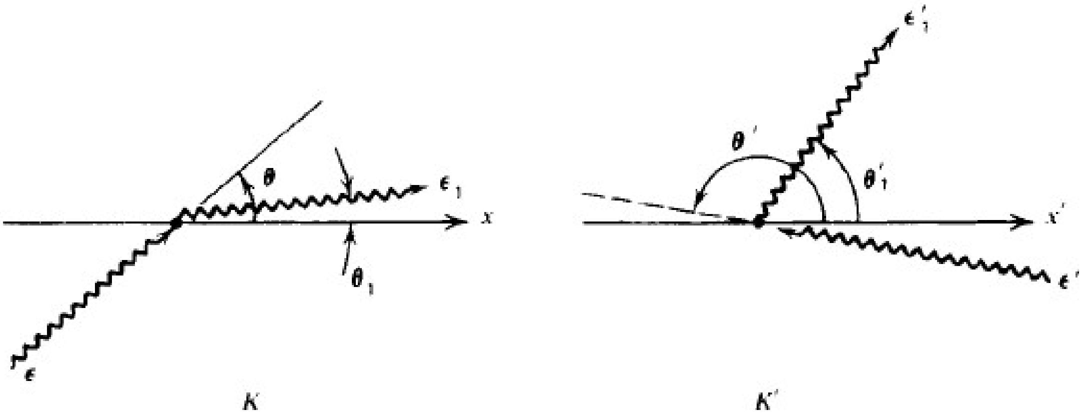

Figure 1.10: A low energy photon and a relativistic electron colliding; to the left is the observer rest frame K, to the right is the electron rest frame K' (G. B. Rybicki and A. P. Lightman 1985);

where $U_{rad} = \int E\nu dE$ is the initial photon energy density (M. S. Longair 2011). Eq. (1.16) and Eq. (1.27), for synchrotron and IC emission, are heavily correlated,

$$\frac{(\frac{dE}{dt})_{syn}}{(\frac{dE}{dt})_{IC}} = \frac{U_B}{U_{rad}} \tag{1.28}$$

and with Eq. (1.28) we can see that the only major difference between the two spectra is the ratio between the density of the magnetic field and the one of the photons; the same stands for the typical timescale of losses for IC, which are related to Eq. (1.21) by the ratio of the two energy densities too. These processes are much alike in their spectrum and their similarity is manifested especially well when we consider that both of them take place in regions with a population a relativistic electrons, ideally with a low density of particles to avoid other kinds of energy losses. Since synchrotron emission has been observed in A399-A401 bridge it is then safe to assume that IC scattering is also happening in the region.

1.3.4 Magnetic field estimates

The nature of the origin of galactic, inter-galactic voids and intra-cluster magnetic fields is still greatly debated and clouded in mystery; two main different types of models attempt to describe the origin of seed magnetic fields, that only later on will be heavily amplified through various processes: a cosmic relic of early universe physics or a product of astrophysical processes in ionized plasma (F. Vazza and al. 2021).
Various structures in the universe are coupled with different typical magnetic field strength, in particular I am interested in the typical strength of magnetic fields in the ICM, as it is the most similar structure to the A399-A401 bridge, and that is of the order of μG or less (F. Govoni and L. Feretti 2004). For the same reason, I am going to limit myself to two methods used to estimate the magnetic field strength in the ICM either directly or indirectly. One of these is based upon the direct observation of synchrotron radiation, which is closely linked to the magnetic field density U_B;

the other one, the indirect approach, is the observation of Faraday rotation in radio sources (M. Murgia and al. 2019).

Equipartition assumption

This assumption is usually applied to determine the strength of the magnetic field from the observation of synchrotron radiation in a radio source, under the assumption that the total energy of a synchrotron source, that being $E_{tot} = E_e + E_p + E_B$, is minimized, where E_e and E_p are the energies of electrons and protons and where, in Eq. (1.29), E_B is the energy of the magnetic field inside a volume V

$$E_B = U_B \phi V = \frac{B^2}{8\pi} \phi V \tag{1.29}$$

with ϕ as the filling factor, the fraction of the volume occupied by the magnetic field (F. Govoni and L. Feretti 2004).
The electron energy can be related to synchrotron luminosity L_{syn} in Eq. (1.30)

$$L_{syn} = \frac{dE_e}{dt} = V \int_{E_1}^{E_2} (-\frac{dE}{dt}) N(E) dE = c_2 (B sin\theta)^2 V N_0 \int_{E_1}^{E_2} E^{-\delta+2} dE \tag{1.30}$$

if $sin\theta = 1$ and VN_0 is discarded to ease the notation then

$$E_e = c_{12}(\alpha, \nu_1, \nu_2) L_{syn} B^{-3/2} \tag{1.31}$$

is the electron energy [Eq. (1.31)], where $E_1 = h\nu_1$, $E_2 = h\nu_2$ and where c_{12} is a numerical constant depending on the spectral index and the initial and final frequencies of the energy range of the spectrum, with its values tabulated (F. Govoni and L. Feretti 2004).
Proton energy [Eq. (1.32)] is in turn related to electron energy by a constant

$$E_p = k E_e \tag{1.32}$$

therefore assuming that the same processes influence both electrons and protons, although with different efficiencies.
Combining the expressions for the different kinds of energies, the total energy takes the form of Eq. (1.33)

$$E_{tot} = (1+k) c_{12} L_{syn} B^{-3/2} + \frac{B^2}{8\pi} \phi V \tag{1.33}$$

which can then be minimized to obtain an estimate on the magnetic field. To do so, we assume that the energies of the magnetic fields and of the particles are equal, therefore the minimal energy, written in Eq. (1.34), also called *equipartition energy*, is

$$E_{eq} = \frac{7}{3} E_B \tag{1.34}$$

to which corresponds an *equipartition value* of B, that being

$$B_{eq} = (6\pi(1+k) c_{12} L_{syn} \phi^{-1} V^{-1})^{2/7}. \tag{1.35}$$

In Eq. (1.35) the estimate on B is directly proportional to the entity of synchrotron luminosity in the region, and inversely proportional to the filling factor (F. Govoni and L. Feretti 2004); k, ν_1, ν_2 and the filling factor are quantities linked to a certain amount of difficulties in their measurements, so this method used to estimate the magnetic field strength of a radio source, although simple, is associated with a fair amount of uncertainties.

Faraday rotation

The propagation of synchrotron light inside a magnetized and ionized medium is affected by a rotation of the polarization plane as the two opposite-handed circularly polarized components of the radiation have two different phase velocities (F. Govoni and L. Feretti 2004).

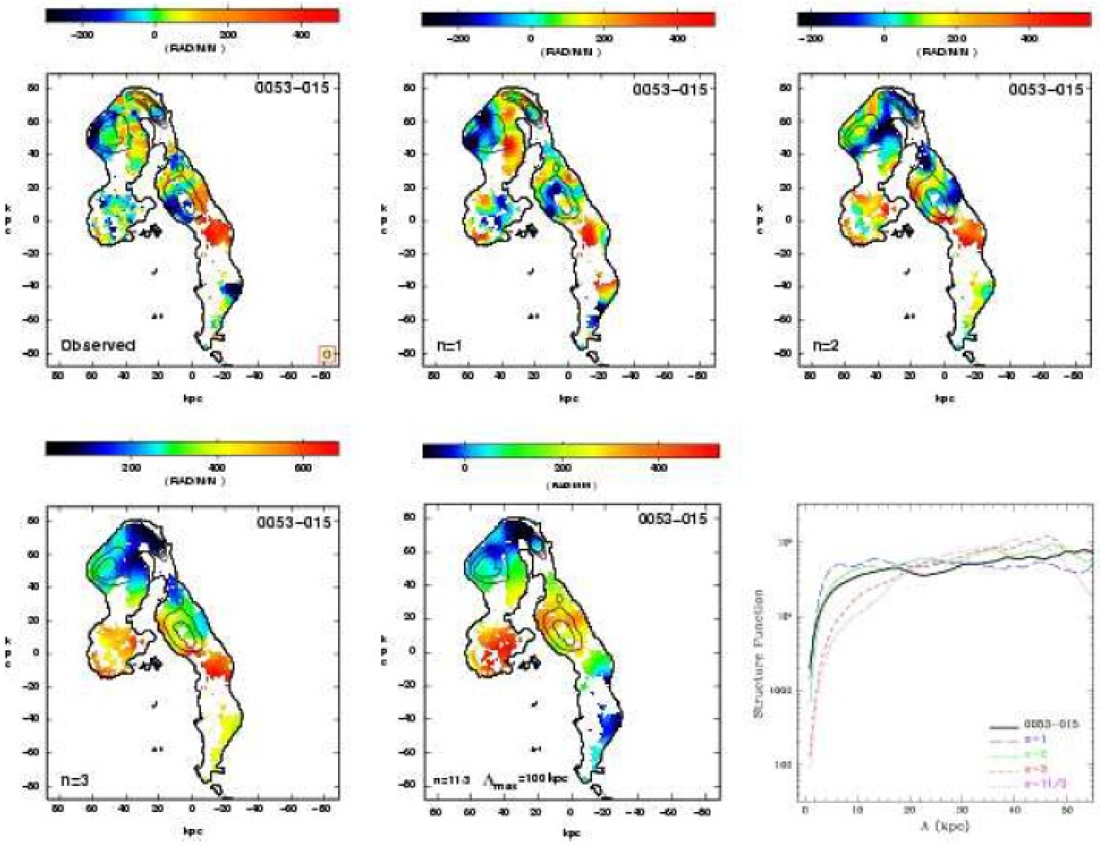

Figure 1.11: A comparison of observed (top left panel) and simulated RM images in the radio source 0053-016 in A119 (M. Murgia and al. 2019);

The observed angle of polarization $\Phi_{Obs}(\nu)$ is

$$\Phi_{Obs}(\nu) = \Phi_{Int} + (c/v)^2 RM \tag{1.36}$$

where Φ_{Int} is the intrinsic polarization angle and RM is the Faraday rotation measure (M. Murgia and al. 2019). The RM is correlated to the component of B

parallel to the line of sight, that being $B_{//}$, and in Eq. (1.37) it takes the form

$$RM = \frac{e^3}{2\pi m_e^2 c^4} \int_0^L n_e(l) B_{//}(l) dl \tag{1.37}$$

where L is the path length of the system, in this case the ICM, and $n_e(l)$ the local density of electrons (F. Govoni and L. Feretti 2004). Because Φ_{Obs} is an observable and it is related to RM by direct proportionality, RM can be obtained by a linear fit of Eq. (1.36), and from that an estimate of $B_{//}$ can be made. There are various complexities associated with this method, par example the fact that every observation is a projection of the magnetic field in the 2D plane of the night sky, the randomness of said magnetic field and the determination of $n_e(l)$; a de-projection of the magnetic field and a measure on the population of electrons can, however, be done with X-ray observations and their comparison with RM images simulations, for which I show an example in Fig. (1.11) in which one of the models ($n = 2$) has shown a remarkable similarity to the RM of the source A399 (M. Murgia and al. 2019).

1.4 Cosmic rays in Large scale structures

Cosmic rays (CR) are highly energetic particles that are accelerated to relativistic energies by a variety of sources and mechanisms, like shock waves, turbulence and ejection currents from compact objects. The composition, the origin and acceleration mechanisms may, in particular, provide a set of categories to better identify them. I briefly summarise here some of the labels that may be applied to a CR particle, whilst I will explain them in more detail later in this Section.

First and foremost if the CR is a proton or an electron then it is called, respectively, CR proton (CRp) or CR electron (CRe) and a population of CR can be usually comprised of both CRe and CRp, the latter typically in the form of secondary products due to the decay of the primary CRp; then the energy of the particle allows us to identify it in CR and Ultra-High Energy CR (UHECR), which belongs to the highest energy CR and, as we will see in shortly, they also differ in origin and acceleration mechanisms.

CR spectrum observed at Earth

Numerous detections of CR particles at different energies, with ground or space detectors, have led to the observation of what is called the CR spectrum, with its composition measured at the top of our atmosphere that is of roughly 98% protons and nuclei, of which 87% are protons, 12% are helium nuclei and 1% are heavier nuclei, and of the remaining 2% electrons (M. S. Longair 2011).

Fig. (1.12) shows an example of the observed spectrum of CR at Earth, a powerlaw type spectrum, with slope and energy range depending on the acceleration mechanism; the spectrum was obtained by combining detections from different experiments.

Some of its most important features are the *knee* around $10^{15} eV$ and the *ankle* around $10^{18} eV$; CR right of the *ankle* are called UHECR. Energies left of the *knee*

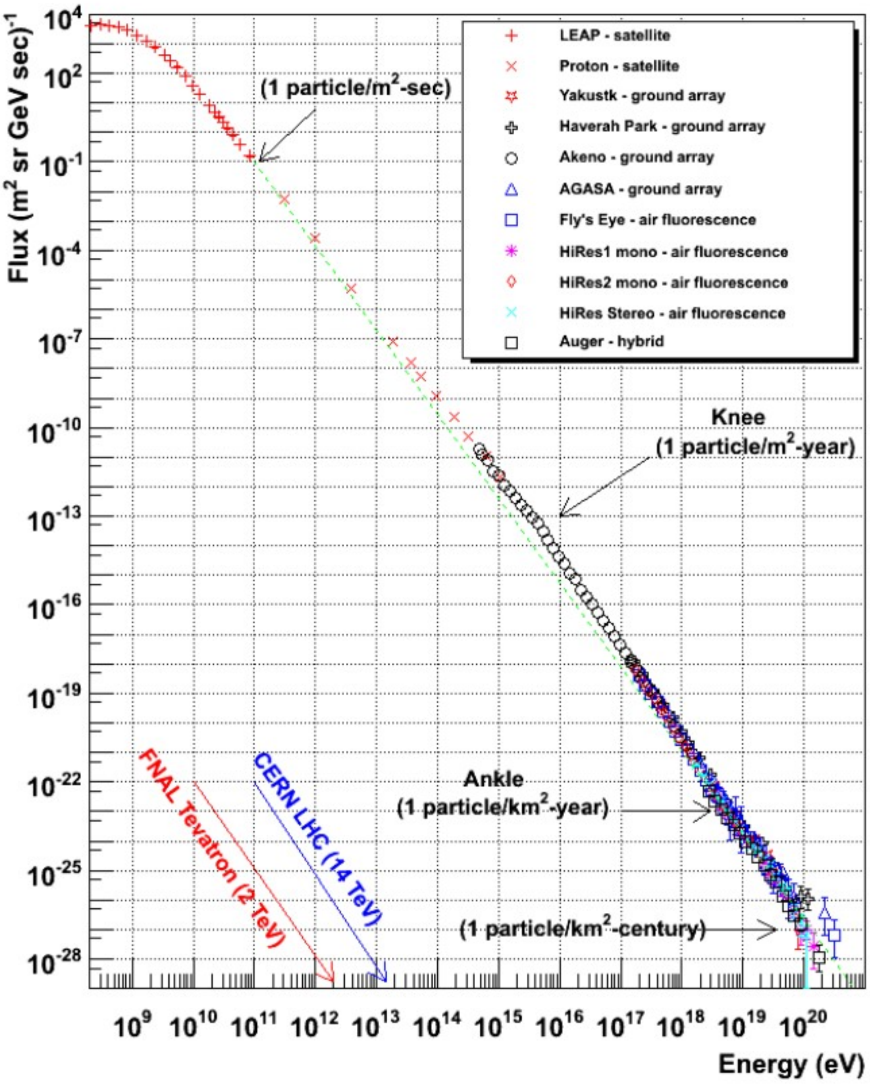

Figure 1.12: Example of powerlaw spectra of CR obtained by the combination of different experiments (W. Hanlon 2008);

usually belong to galactic CR while those right of it usually belong to extra-galactic CR, because the size of our Galaxy is not enough to contain those CR before they can get accelerated to those high energies. The difference between these energy regimes even manifests in deployed detection techniques, as CR left of the *knee* can be observed directly with particle detectors while CR to the right of it can be observed indirectly with an air-shower technique. This technique utilizes the difference between the spectrum of primary or secondary CR, so if the observed radiation comes from a CRe emitting or from a CRp that has decayed, usually in pions, emitting γ-rays, through the hadronic mechanism: this is the production of a cascade of secondary CR originating from the primary CRp that can be measured by the above mentioned air-shower technique.

Also, CRe less than a GeV have a spectrum that can be easily influenced by solar modulation, while CRe from roughly 1 GeV to the order of $10^{11} GeV$ do not feel this effect, even though they can all be described by a powerlaw spectrum (M. S. Longair 2011). Fig. (1.12), ideally, represents all the CR spectra observed from the sky, with a slope of −2.7 left of the *knee* and of −3.1 to the right of it.

CR spectrum from a single source

The spectrum of CR observed at Earth is obtained from the compositions of CR spectra from single sources or populations, in general in the form of powerlaws, with each one that may have very different slopes depending on the system of origin and the acceleration mechanism.

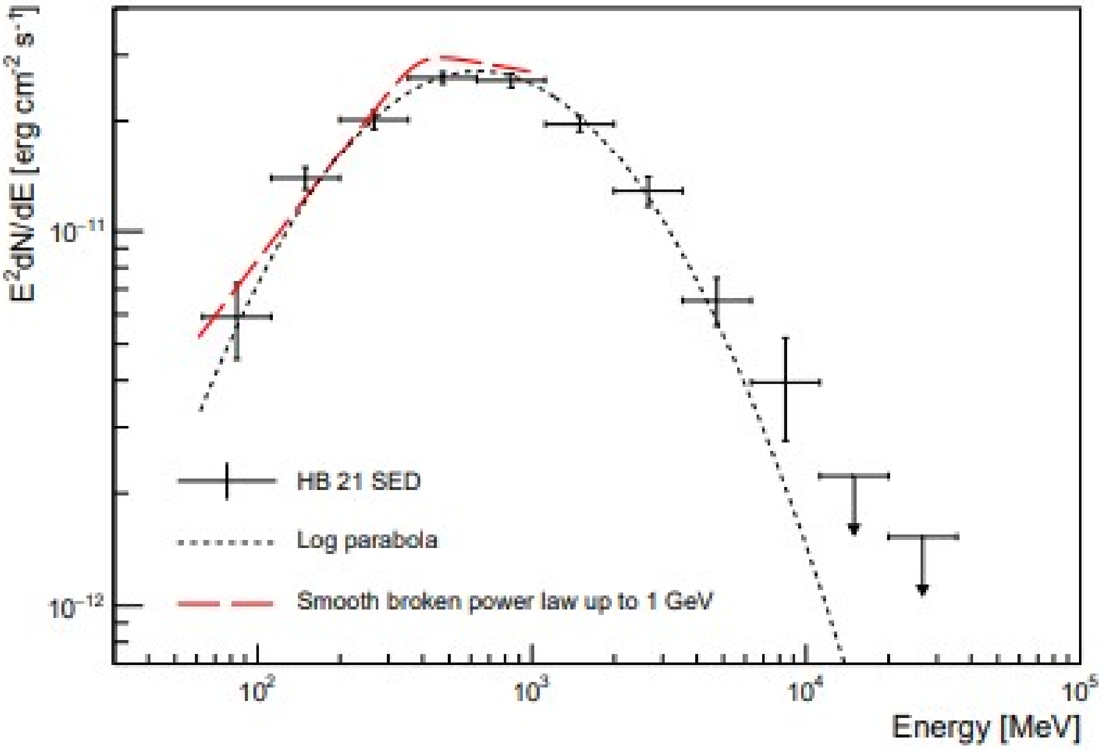

Figure 1.13: Pion bump due to the decay of pions and to bremsstrahlung emission in SNR HB 21 (L. Ambrogi and al. 2019);

CRe populations are usually found with a powerlaw distribution, but CRp spectra are characterized by a different form, due to the decay of CRp signaling the production of secondary CR that produce what is called the the *pion bump*, which is exemplified by Fig. (1.13) that illustrates the CR spectrum of a SuperNova Remnant (SNR) and its *pion bump*.

Now that I have given some general characteristic on CR spectra, I can write about some of the most important aspects that can help define how CR gain energy, propagate and become visible. Those are the maximum energy E_{max} that the CR population can reach with a certain acceleration mechanism, the minimum energy E_{min} that can be affected by said mechanism, since the negative slope of the powerlaw distribution means that the majority of the CR population will have energy close to this one, greatly influencing our understanding of the population, and finally the

cooling processes that oppose the acceleration of CR but nonetheless make them observable.
The maximum energy E_{max} of the CR population is particularly significant because it is the quantity used to confront the typical acceleration (gain) time-scale $\tau_{gain} = E_{max}/(dE/dt)_{gain}$ and cooling (loss) time-scale $\tau_{cool} = E_{max}/(dE/dt)_{cool}$; if $\tau_{gain} \geq \tau_{cool}$ then it means that, in general, the acceleration mechanism used to describe that CR is not likely to be correct, because it would lose its energy before reaching E_{max}; also E_{max} can be roughly estimated by putting $\tau_{gain} \approx \tau_{cool}$. In general, for a hypothesis on the nature of some CR to be plausible it has to have that $\tau_{gain} \leq min(\tau_{cool}, \tau_{age}, \tau_{escape})$, where τ_{age} and τ_{escape} are respectively the age of the source of the CR and the time it takes the particle to escape the acceleration region.

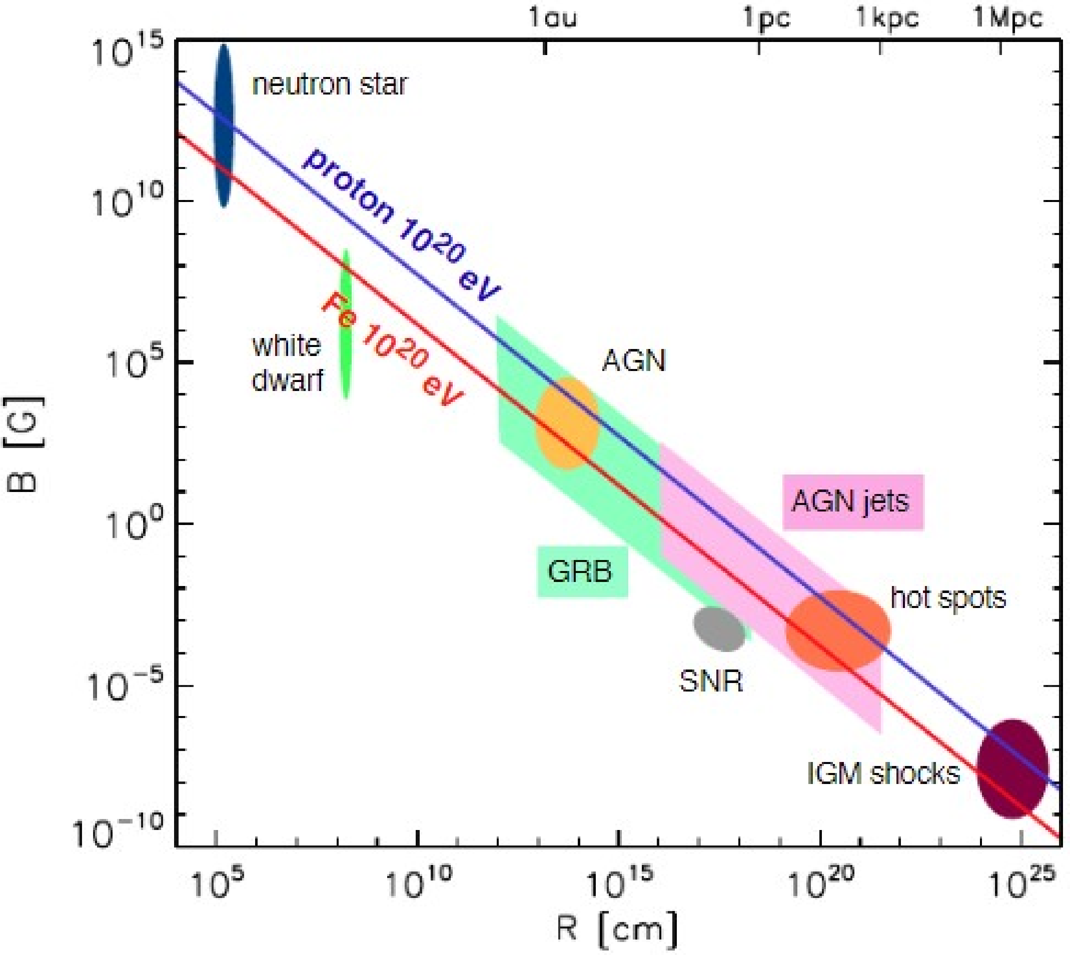

Figure 1.14: *Hillas plot*, that shows what are the magnetic field and size needed so that a source of CR can accelerate them at energies up to $10^{20}eV$ (R. Aloisio 2017);

Since the particles need to remain inside the acceleration region for a sufficient amount of time, the strength of magnetic fields in said region and the size of it are linked, as we can see in an example of an updated *Hillas plot* in Fig. (1.14), where

the colored regions in the graph indicate under what conditions several astrophysical phenomena can confine a CR of certain energy; this plot in particular considers protons or nuclei that are UHECR, while Fermi models and their application to this work affect CR that are 10 order of magnitude less. However the concept of the *Hillas plot* still stands.
Acceleration mechanisms can be either stochastic or systematic, respectively if they are due to a process that involves losses and gain of energy, with the latter that are predominant, or either by processes that only provide a gain of energy. For example, a systematic process may happen through collisions of particles or motions of chunks of plasma, like in Fermi I models, or either a stochastic process may happen through turbulence, like in Fermi II models; an acceleration mechanism can be a mix of these typologies. In particular, I will talk about Fermi I and Fermi II acceleration mechanism and the Diffusive Shock Acceleration, as they are the main processes that may be considered responsible for the acceleration of CR in the bridge A399-A401.

1.4.1 Fermi I and Fermi II models

Fermi introduced in 1949 a stochastic acceleration mechanism that consists in particles colliding with clouds in the interstellar medium, during which the particles gain energy through the collision with moving magnetic fields (E. Fermi 1949). Fermi used this mechanism to try and explain the origin of galactic cosmic rays, even if it was incapable of reaching their required amount of energy. The magnetic fields act like mirrors to the particles, as Fig. (1.15) shows, and the random movements of the magnetic fields ensure a stochastic gain of energy through each interaction, making this model especially fitting to describe turbulent mediums, although the ionization losses are too large to allow this early Fermi II model to reach the energies required

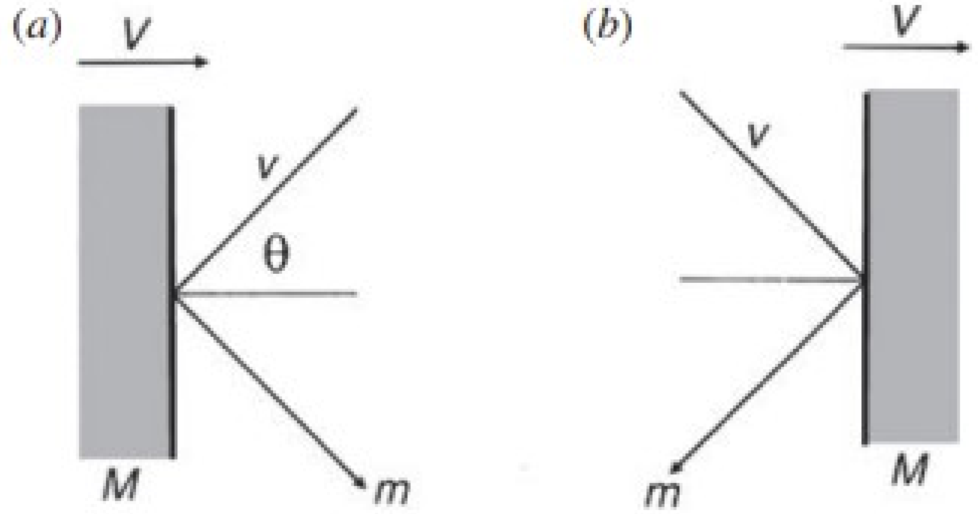

Figure 1.15: Collision between a particle of velocity v and mass m at an angle $theta$ with a cloud of velocity V and mass M; in panel a the collision is $head-on$ while on panel b it is a $following$ collision (M. S. Longair 2011);

to explain the galactic CR. Both modern Fermi I and Fermi II models are based on the same concept of the original Fermi model: a particle gains energy through collisions with a cloud; if the collisions are mono-directional then we are in a Fermi I model, if they are stochastic then we are in a Fermi II model.

I will now explain in more detail the basic mechanism for both the models. Let the momentum and the energy of a particle about to undergo a Fermi acceleration be respectively

$$\vec{p} = \gamma m \vec{v} \tag{1.38}$$

and

$$E = \gamma mc^2 \tag{1.39}$$

with γ being the Lorentz factor. The momentum and energy of the cloud can be expressed in the form of Eq. (1.38)-(1.39) too, and in general we have that $M \gg m$ and $V \ll v$ so that collision with particles can be considered elastic and the velocity of the cloud itself remains the same.

We want to determine the distribution of particles in the acceleration region because that is of key importance to define the spectrum of CR associated with said population. If the initial population is composed of N_0 particles with an energy of E_0 such that $N(E_0) = N_0$ and we assume for simplicity, even if it will not be the case later on, that with each interaction the gain in energy is the same positive fraction β, then after k collisions

$$E = \beta^k E_0 \tag{1.40}$$

is the average energy of the particles. At the same time, after k collisions the number of particles inside the acceleration region is

$$N = P^k N_0 \tag{1.41}$$

where P is the probability of a particle to stay in the system and so to keep on accelerating.

By combining Eq. (1.40)-(1.41) and by using the parameter in Eq. (1.42)

$$\xi = \frac{lnP}{ln\beta} \tag{1.42}$$

a distribution can be defined, in fact

$$N(E) = N_0 (\frac{E}{E_0})^{\xi} \tag{1.43}$$

but since these particles will keep on being accelerated, Eq. (1.43) has the meaning of a cumulative distribution function for the number of particles with energies greater than E, whose differential may be written as

$$N(E)dE \propto E^{-1+\xi} dE = E^{-p} dE \tag{1.44}$$

where $p = 1 - \xi$ is the slope of the powerlaw distribution of particles and Eq. (1.44) is the key result for Fermi acceleration models. The value of p may depend on various factors, those being the galactic or extra-galactic nature of the CR population and the source of acceleration, like a SNR or a shock in the ICM, amongst other factors. The energy gain can be better quantified if we consider the change in momentum of the particle that is inverted from $pcos\theta$ to $-pcos\theta$ in the x direction, where if $cos\theta > 0$ then we have a $head - on$ collision or viceversa, if $cos\theta < 0$. Let us consider the energy and the momentum in the x direction of the particle in the rest frame of the cloud, those are

$$E' = \gamma_V(E + Vpcos\theta) \tag{1.45}$$

and

$$p'_x = \gamma_V(pcos\theta + \frac{VE}{c^2}) \tag{1.46}$$

where Eq. (1.45)-(1.46) have been obtained using Lorentz transformations and $\gamma_V = 1/\sqrt{1 - V^2/c^2}$ is the Lorentz factor of the cloud. After the collision $p'_x = -p'_x$, while the energy remains the same, so by combining Eq. (1.38)(1.39) and by returning to the rest frame of the observer Eq. (1.45) becomes the energy of the particle after the collision [Eq. (1.47)]

$$E'' = \gamma_V^2(E + 2pVcos\theta + \frac{V^2}{c^2}E). \tag{1.47}$$

The fractional energy gain $\beta = \Delta E/E$ is therefore

$$\beta \approx \frac{2vV}{c^2}cos\theta + 2\frac{V^2}{c^2} \tag{1.48}$$

with an approximation at 2^{nd} order.

Now it is possible to lift the simplifying assumption that with each collision comes an energy gain, in fact the sign of $cos\theta$ determines whether the particle is accelerated or decelerated. Not only that, but if the first right-hand term of Eq. (1.48) is much greater than the second term, so $\frac{2vV}{c^2}cos\theta >> 2\frac{V^2}{c^2}$, then the acceleration is of type Fermi I, while if $\frac{2vV}{c^2}cos\theta << 2\frac{V^2}{c^2}$ it is of type Fermi II, as in the case of the original Fermi acceleration model.

In particular Fermi I accelerations are usually associated to shocks in a medium, because it is possible to define the angle of collision, and so a $cos\theta$, between the wavefront of the shock and the velocity of the particle; Fermi II accelerations are usually associated with a turbulent medium (G. Brunetti and F. Vazza 2020).

The average efficiency of Fermi acceleration can be calculated by integrating Eq. (1.48) over all θ and in the ultra-relativistic case ($v \approx c$) it is

$$< \beta >= \frac{8}{3}\frac{V^2}{c^2}. \tag{1.49}$$

$< \beta >$ in Eq. (1.49) is the average energy gain per collision and it is only of second order in V (M. S. Longair 2011). In general $V << v$ therefore to reach the highest energies long times or a re-acceleration of pre-existing particles are required.

Let us take Eq. (1.49), if L is the mean free path of the CR then it is possible to define an average rate of energy gain [Eq. (1.50)]

$$\frac{dE}{dt} = \frac{4}{3}\frac{V^2}{cL} = \alpha E \tag{1.50}$$

which is particularly useful as it can allow us to compute the spectrum of CR by substituting it to the energy-loss term $b(E) = -\alpha E$ in the $Diffusion - loss$ $equation$, that being

$$\frac{dN(E)}{dt} = D\nabla^2 N(E) + \frac{\partial}{\partial E}[b(E)N(E)] - \frac{N(E)}{\tau_{escape}} + Q(E) \tag{1.51}$$

where D is the spatial diffusion coefficient, even though this equation is not usually applied to Fermi II models, since a Fokker-Plank equation is preferred (M. S. Longair 2011). The first term in Eq. (1.51) is due to diffusion effects, the second term to losses of energy, the third to CR escaping and the forth and final to injection of particles.

As above mentioned, Fermi II models have very slow gain of energy and they struggle to explain how CR can reach high relativistic energies (higher than GeV), however Fermi I models can overcome these limits because various galactic and extra-galactic media are subjected to strong shocks, allowing the particles to accelerate to relativistic energies rather quickly. The Diffusive Shock Acceleration model is the most studied of how Fermi I shocks may accelerate CR.

1.4.2 Diffusive Shock Acceleration

The Diffusive Shock Acceleration (DSA) is a special case of Fermi I models applied to shocks in a medium. It is particularly useful because it allows to link directly the slope p of the particle distribution to the strength of shocks, not only that but it can calculate E_{max}, the time evolution of $N(E)$ and the possibility of the shock being modified by the CR themselves, that act like a second fluid in the medium.

A shock wave is characterized by its Mach number M

$$M = \frac{v}{c_s} \tag{1.52}$$

where c_s is the sound velocity of the medium, that from now on I will identify with the ICM, as it is the one interesting to this work, even though this model works especially well for SNR too. In Fig. (1.16) we see an illustration for a strong shock with the major quantities of interest before and after the shock. The Mach number of Eq. (1.52) is linked to the compression factor $r = \rho_2/\rho_1 = v_1/v_2$ as we can see in the following equations, obtained through mass and momentum and energy conservation, under the strong shock approximation,

$$r = 1 + \frac{3}{5M_2^2} \tag{1.53}$$

$$r^2 = 1 + \frac{3}{M_2^2} \tag{1.54}$$

for a monoatomic plasma, where M_2 is the downstream Mach number, and by combining Eq. (1.53) and Eq. (1.54) we obtain that the compression factor $r = 4$.

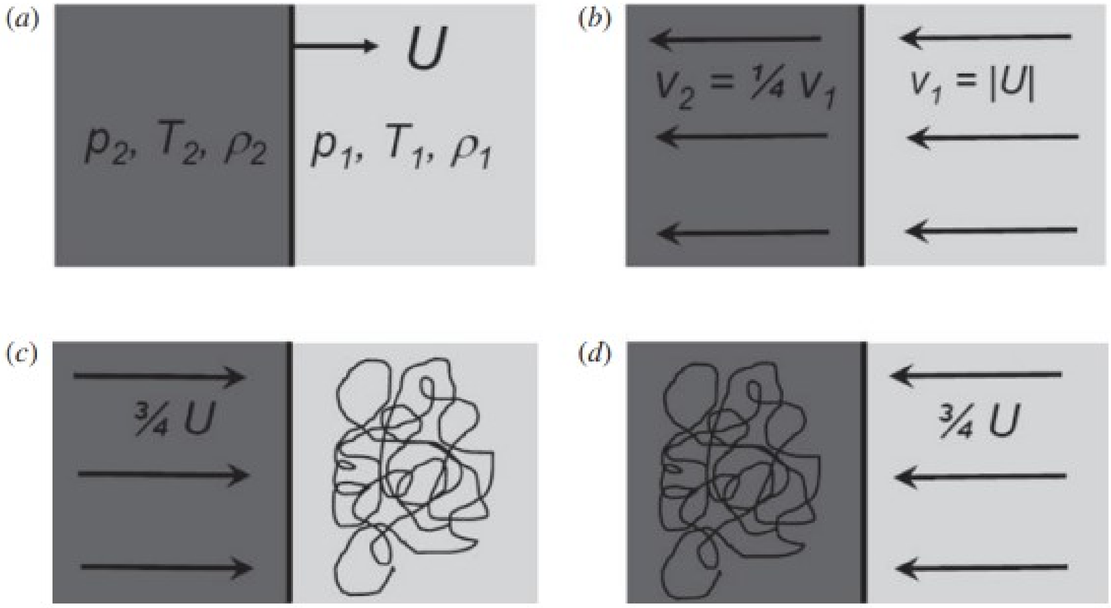

Figure 1.16: Illustration of a strong shock. the pressure p_2, the temperature T_2 and the density ρ_2 are for the ICM after the shock, while p_1, T_1 and ρ_1 are for before the shock; U is the velocity of the shock wave, v_1 and v_2 are the upstream and downstream velocities in the rest frame of the shock wave. Panel *a* is in the rest frame of the ICM, panel *b* is in the rest frame of the shock, panel *c* is in the rest frame of the upstream gas with an isotropic velocity distribution of CR and panel *d* is in the rest frame of the downstream gas with the same velocity distribution (M. S. Longair 2011);

Particle distribution in DSA

Now that this quick overview of shock dynamics is out of the way I can proceed in explaining how the DSA model can derive the slope of the distribution of CR particles. The acceleration of particles happens for particles in the $non-thermal$ tail of the maxwellian distribution of velocities that when they meet the shock they can begin to cross the shock wave front several times, bouncing back and forth from the upstream to the downstream side of the shock and viceversa, increasing their Larmor radius with each crossing. Each crossing brings about a $head-on$ collision between particles and the plasma on the other side of the shock that has a velocity of $V = v_1 - v_2 = 3/4U$, so each crossing causes the particle to accelerate; the particles that stay in the acceleration region the longest are the ones that eventually can reach E_{max}.

Let us consider a non-relativistic shock with relativistic particles ($v \approx c$), then Eq. (1.48) becomes

$$\beta \approx \frac{V}{c} cos\theta \tag{1.55}$$

for each crossing, with $0 < \theta < \pi/2$, and if we integrate Eq. (1.55) over all angles we obtain the average energy gain

$$<\beta> \approx \frac{2V}{3c} \tag{1.56}$$

that doubles if the particles bounce back to the starting region (upstream or downstream). Since $V = v_1 - v_2$ Eq. (1.56) becomes

$$< \beta > \approx 1 + \frac{v_1}{c} \tag{1.57}$$

for a strong shock, where $v_2 = 1/4v_1$.
To derive the probability $1 - P$ of a particle not escaping the region of the shock the rate of the particle crossing the shock $\dot{N}_{in}$ and to be lost downstream $\dot{N}_{out}$ can be compared, and those are respectively

$$\dot{N}_{in} \approx N_{in} c cos\theta \approx \frac{nc}{4\pi}\int_0^{\pi/2} cos\theta sen\theta d\theta \approx \frac{nc}{4} \tag{1.58}$$

assuming a small diffusion, and

$$\dot{N}_{out} \approx nv_2 \tag{1.59}$$

where n is the density of particles and $v_2 = v_1/4$ in the strong shock approximation. Therefore if we divide Eq. (1.59) with Eq. (1.58) we obtain

$$1 - P \approx \frac{v_1}{c}. \tag{1.60}$$

From Eq. (1.60), the probability of a particle staying in the acceleration region can be immediately obtained and that is

$$P = 1 - \frac{v_1}{c} \tag{1.61}$$

so, by substituting Eq. (1.57) and Eq. (1.61) inside Eq. (1.42) we obtain the slope of the particle distribution in a strong shock approximation

$$p = 1 - \frac{lnP}{ln\beta} \approx 2 \tag{1.62}$$

where a second order Taylor expansion has been performed. So the particle distribution is

$$N(E) \propto E^{-2}. \tag{1.63}$$

However, for a generic shock the slope of Eq. (1.62) becomes

$$p = 2\frac{M^2+1}{M^2-1} \tag{1.64}$$

and so Eq. (1.63) becomes

$$N(E) \propto E^{-2\frac{M^2+1}{M^2-1}} \tag{1.65}$$

that it is the prediction of DSA for a CR distribution when the shock remains the same during the acceleration process. In particular Eq. (1.65) tends to Eq. (1.63) when $M \to \infty$.
Now that I have established what is the distribution of CR in a DSA model I can also talk about the minimum energy required to begin the acceleration process, the maximum energy reachable and also, although briefly, the possibility of the CR population modifying the shock that has accelerated them, in what is called a $two - fluid$ model.

Minimum and maximum energy

The minimum energy E_{min} can be narrowed down when applying the *thermal − leakage* model, that is the hypothesis that the "tail" of the Maxwellian distribution of velocities "leaks" its highest energy particles, that from thermal become non-thermal; E_{min}, or conversely its momentum p_{min}, is the critical energy after which CR get accelerated by shocks. A useful parameter is ξ_{inj}, such that

$$p_{min} = \xi_{inj} p_{th} \tag{1.66}$$

where $p_{th} = \sqrt{2mk_bT_1}$ is the momentum of the thermal maxwellian and $\xi_{inj} \approx 3 - 3.5$ (D. Caprioli and A. Spitkovsky 2014a). In Fig. (1.17) we can see the distinction between the thermal particles and the non-thermal particles, because as time progresses after the shock a clear neat turn appears in the spectrum. However, defining E_{min} is not an easy task, also because it is near the tail of the maxwellian, where there is a rapid drop in the distribution, therefore a small change in E_{min} will cause a great difference in the resulting CR spetrum; simulations are often used to try and constrain its value.

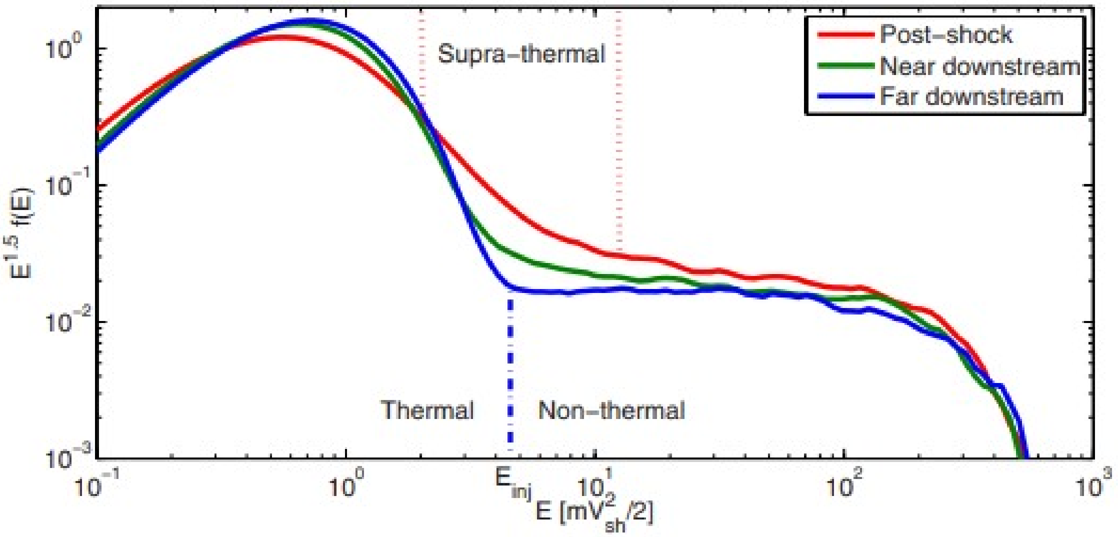

Figure 1.17: Energy distribution of particles immediately after the shock (red), some moments later (green) and far downstream (blue); V_{sh} is the velocity of the shock (D. Caprioli and A. Spitkovsky 2014a);

The maximum energy can be better defined and its value depends on the diffusion coefficient $D(E) = l_d^2/t$, where $l_d = v_1\tau_d$ is the maximum distance swept by the shock through diffusion in a time τ_d. In particular $l_d^2 = D(E)\tau_d$, so

$$\tau_d(E) = \frac{D(E)}{v_1^2} \tag{1.67}$$

and since the energy of the particle only increases with time as it stays inside the shock region we have that $\tau_d \approx \tau_{acc}$, where τ_{acc} is the time required for a CR to reach E_{max}. Therefore, Eq. (1.67) leads to

$$E_{max} \approx (\frac{v_1^2\tau_{acc}}{D_0})^{\alpha} \tag{1.68}$$

where $D(E) = D_0 E^{\alpha}$ so that Eq. (1.68) may have a simplified notation, however D_0 and $D(E)$ are in general unknown. A more precise definition of E_{max}, in Eq. (1.69), is

$$E_{max}(t) \approx \frac{E_{sh}}{3D(E_{max})} D_B(E_{max}) \omega_c t \tag{1.69}$$

where E_{sh} is the energy of the shock, ω_c is the cyclotron pulsation and D_B is the Bohm diffusion coefficient

$$D_B(E) = \frac{E}{m\omega_c} \tag{1.70}$$

commonly used for non-relativistic shocks for which it can be assumed that Bohm diffusion takes place, so that the mean-free path of the particles with mass m is of the order of the gyroradius r_g of the particles (D. Caprioli and A. Spitkovsky 2014b). The diffusion coefficient $D(E)$ is not easily constrained, it could be the Bohm diffusion coefficient, or it could derive from a model of turbulent diffusive magnetic eddies, where particles have a mean-free path $L_0 >> r_g$; in general $D(E)$ cannot be solved with DSA but it needs an independent study.

1.4.3 Modified shocks

In a strong shock regime, for $M >> 10$, CRs are believed to be efficiently accelerated, even to the point where their pressure becomes comparable to that of the shock. Consequentially, the dynamics of the shock is modified.

This regime does not occur for the predicted moderate Mach numbers, $M < 10$, in the intracluster bridge that is of interest for my Thesis. However, this regime is relevant to the case of SuperNova Remnant shocks, but for completeness I give some of the most important features connected to shock modification by CRs in this regime.

One of most prominent features of the CR-modified shock is the formation of a *precursor* to the shock, that slows down the upstream flow because of the pressure and density of the CR fluid (D. Caprioli and A. Spitkovsky 2014a). Some of its ulterior effects are the beginning of a non-linear regime, since the shock is progressively modified by the CR, and also the modification of the normal shock jump conditions and of the particle distribution spectrum from Eq. (1.65). In Fig. (1.18) we see a modified shock and the difference in the compression factor when the inclination between the magnetic fields and the direction of the shock changes, in particular the compression factor is different from the one predicted by DSA for strong shocks because of the pressure and density of the CR fluid.

Let the compression factor r_{sub} be the one for the CR fluid, it depends on the adiabatic index Γ_{eff} of the fluid, that is the effective adiabatic index obtained through Eq. (1.71)

$$\Gamma_{eff} = \frac{\Gamma_{pl} E_{pl} + \Gamma_{CR} E_{CR}}{E_{pl} + E_{CR}} \tag{1.71}$$

where Γ_{pl} and E_{pl} are the adiabatic index and the bulk energy for the plasma component of the two-fluid model and where Γ_{CR} and E_{CR} are their counterpart for the CR component of the system. In particular we take $\Gamma_{pl} = 5/3$ for a non-relativistic

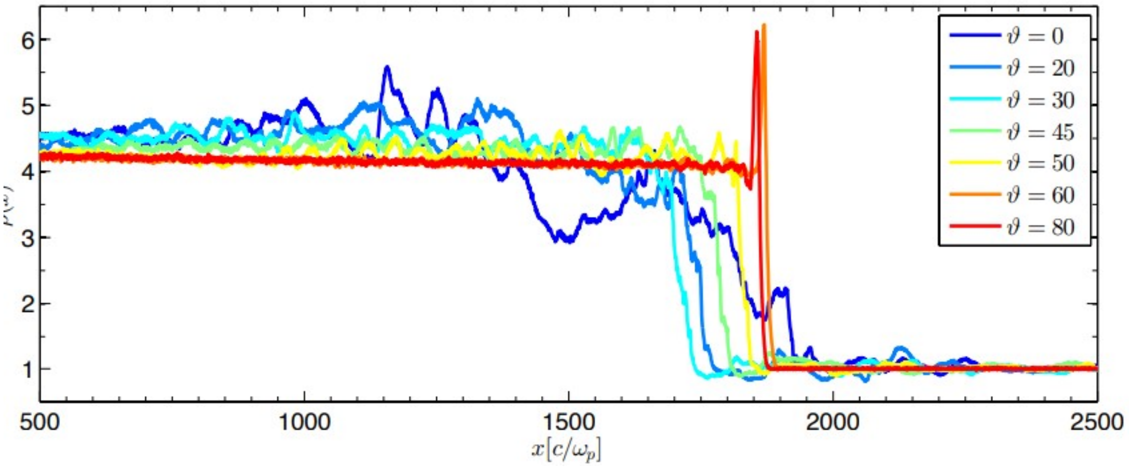

Figure 1.18: Density profile for a shock with $M = 30$ and with different angles of inclination θ between the magnetic field and the direction of the shock (D. Caprioli and A. Spitkovsky 2014a);

medium, and $\Gamma_{CR} = 4/3$ for a relativistic CR fluid, so $4/3 \leq \Gamma_{eff} \leq 5/3$. By using Γ_{eff}, r_{sub} takes the form of Eq. (1.72)

$$r_{sub} = \frac{(\Gamma_{eff} + 1)\tilde{M}_1^2}{(\Gamma_{eff} - 1)\tilde{M}_1^2 + 2} \tag{1.72}$$

where $\tilde{M}_1$ is the Mach number of the fluid immediately upstream in the shock rest frame and where the contribution of magnetic fields has been neglected for simplicity (D. Caprioli and A. Spitkovsky 2014a). The total compression factor r_{tot} for a strong shock in the two-fluid model is

$$r_{tot} \approx r_{sub}(1 + \frac{1}{\Gamma_{eff}\tilde{M}_1^2}) \tag{1.73}$$

where I have neglected to write all numerical factors for brevity (D. Caprioli and A. Spitkovsky 2014a). Eq. (1.73) gives the quantification of how much the CR fluid has modified the shock and with simulations performed in D. Caprioli and A. Spitkovsky (2014a) we have that $r_{tot} \approx 4.23$ so it has a value higher than the DSA prediction for a non-modified shock, as we could expect due to the additional compression that the CR fluid causes on the modified one.

1.4.4 Turbulence in Fermi II models

Turbulent media can be hosts to Fermi II type acceleration, for which the average energy gain and average rate of energy gain are the ones in Eq. (1.49)-(1.50). The random interactions between portions of the clouds in the medium, that again I take as the ICM, lead to a stochastic ensemble of collisions that happen isotropically and lead to the acceleration of CR, often inefficiently due to ionization losses that overwhelm the gains in energy, and because of this turbulence is usually considered to re-accelerate fossil particles in the ICM rather than accelerate a newly injected

population (G. Brunetti and T. W. Jones 2014). For the ICM and for a re-acceleration of a fossil population of CRe to energies in the order of $5-10\ GeV$, the typical re-acceleration time is of $0.4-1\ Gyr$, while a new injected population of electrons would need much more time to reach the same energies (G. Brunetti and A. Lazarian 2007). The acceleration time, if compared to the relatively short life-time of roughly a few 100 Myr for CRe emitting in radio, introduces the problem of the necessity of a continuous acceleration of CRe happening *in situ*, for which the mechanism is not so easily identifiable (G. Brunetti and T. W. Jones 2014).
Fermi II mechanisms can be divided in two major classes: resonant or non resonant. Resonant type mechanisms can accelerate CR through an interaction particle-wave only under a resonant condition, one of the most famous examples of it makes use of Alfvén waves, while non resonant type mechanisms can accelerate CR without requiring that the configuration particle-wave undergoes a narrow condition (R. Kulsrud and W. P. Pearce 1969).
A resonant interaction between CR and Alfvén waves results in a scattering in pitch angles with small energy changes. Now, to better understand the mechanism behind this type of scattering, let us consider a CR moving at an ultra-relativistic velocity ($v \approx c$), for simplicity, around a magnetic field B_0 and let us decompose its velocity in the parallel and perpendicular component, respectively Eq. (1.74)-(1.75),

$$v_{//} = \mu v \tag{1.74}$$

and

$$v_{\perp} = (1-\mu^2)v \tag{1.75}$$

where $\mu = cos\phi$ and ϕ is the pitch angle.
The hydromagnetic wave with which the CR interacts has an Alfvén wave velocity [Eq. (1.76)] of

$$v_A = \frac{B_0}{\sqrt{4\pi\rho_{ICM}}} cos\phi \tag{1.76}$$

(R. Kulsrud and W. P. Pearce 1969).
Now, we can also add a small perturbation $\delta B << B_0$ perpendicular to B_0, and then the resulting equation of motion in the rest frame of the wave is

$$\frac{d\vec{p}}{dt} = q\frac{\vec{v}}{c} \times (\vec{B}_0 + \delta\vec{B}) \tag{1.77}$$

where q is the charge of the particle. In Eq. (1.77) only $v_{\perp}$ has its direction changed by the perturbation δB, as we can see in Eq. (1.78), and since

$$\frac{dp_{//}}{dt} = \frac{q}{c}(v_{\perp} \times \delta\vec{B}) \tag{1.78}$$

with $p_{//} = p\mu$, we have that

$$\frac{d\mu}{dt} = \frac{q(1-\mu^2)^{1/2}B_k}{m\gamma c} cos[(\Omega - kv\mu)t + \phi] \tag{1.79}$$

where $\Omega = qB_0/(m\gamma c)$ is the Larmor frequency, k is the module of the wave number and B_k is the magnetic field in the direction of k. However if we were to average it over all pitch angles then the mean would be null, so I will consider the quadratic terms, integrating Eq. (1.79) in time and averaging over pitch angles. Therefore we obtain

$$D_{\mu\mu} =< \frac{\Delta\mu\Delta\mu}{\Delta t} >= \frac{q^2(1-\mu^2)\pi B_k^2}{m^2\gamma^2c^2}\frac{1}{v\mu}\delta(k - \frac{\Omega}{v\mu}) \tag{1.80}$$

with $D_{\mu\mu}$ being the diffusion coefficient for pitch angles, for a single wave k. Eq. (1.80) has a non-null value, so it grows with time only under the resonant condition of $k = \Omega/(v\mu)$, in that case there is diffusion of pitch angles, a scattering. In this case, we can define

$$\tau_{scatt} = \frac{\mu^2}{D_{\mu\mu}} \tag{1.81}$$

that is the isotropization time [Eq. (1.81)], the time the particles require to completely lose memory of the initial pitch angle.

However, up until now we have considered only a single wave number k, therefore generalizing the results just obtained is of key importance. If we consider the turbulent power spectrum $P(k)$ rather than a single k then Eq. (1.80) takes the form of Eq. (1.82), in which

$$D_{\mu\mu} = \frac{4\pi^2q^2(1-\mu^2)}{m^2\gamma^2c^2}\frac{1}{v\mu}\int dkP(k)\delta(k - \frac{\Omega}{v\mu}) \tag{1.82}$$

where there are multiple resonant scales, depending on each wave $k = \Omega/v\mu$. The scattering time-scale retains the same form of Eq. (1.81), even if $D_{\mu\mu}$ is now generalized for multiple waves.

In the same time τ_{scatt} there is a change in particle momenta. In particular, the diffusion coefficient in momentum space for an isotropic distribution of Alfvén waves and CRe can be written as

$$D_{pp}(k,t) = \frac{2\pi^2e^2v_A^2}{c^3}\int_{k_{min}}^{k_{max}}\frac{P(k,t)}{k}[1-(\frac{v_A}{c}+\frac{\Omega m}{pk})^2]dk \tag{1.83}$$

(G. Brunetti and al. 2004). In Eq. (1.84), k_{min} is the minimum wave number that can allow a CR-particle interaction, and it is

$$k_{min} = \frac{\Omega m}{p}(\frac{1}{1-\frac{v_A}{v}}) \tag{1.84}$$

whilst k_{max} is the maximum wave number that can maintain the frequency of the Alfvén wave under the cyclotron frequency of protons Ω_p and $k_{max} = \Omega_p/v_M$, with v_M being the magnetosonic velocity of the waves (G. Brunetti and al. 2004).

If however, the turbulent power spectrum has the simplifying form of a powerlaw $P(k) \propto k^{-\omega}$, then Eq. (1.83) becomes Eq. (1.85), that is

$$D_{pp}(k) = A_\omega(\delta B)^2v_A^2(\frac{p}{B})^\omega(1-\frac{v_A}{c})^\omega\{\frac{1}{\omega} - \frac{v_A/c}{1+\omega} - \frac{(v_A/c)^2}{\omega(1+\omega)}\} \tag{1.85}$$

where δB [Eq. (1.86)] is

$$\delta B^2 = 8\pi\int P(k)dk \tag{1.86}$$

and where A_ω is a numerical factor depending on ω, the slope of $P(k)$ (G. Brunetti and al. 2004).
The diffusion coefficient in Eq. (1.85) can be used also to define the characteristic time of acceleration of CR, that being

$$\tau_{acc} \approx \frac{p^2}{D_{pp}} \tag{1.87}$$

and if we compare Eq.(1.81)-(1.87) then, in Eq. (1.88), we obtain that

$$\tau_{acc} \approx \tau_{scatt}(\frac{c}{v_{ph}})^2 \tag{1.88}$$

where v_{ph} is the phase speed of the wave; so the time needed for the particles to gain energy via diffusion in particle momentum space is larger than the time needed for the particles of the system to follow an isotropic distribution.
In galaxy clusters a Fermi II mechanism is often applied, based on Transit-Time Damping (TTD) resonance, involving the interaction between magnetosonic/fast modes and particles in a compressive collisionless turbulence (G. Brunetti and A. Lazarian 2007). An example for the resulting acceleration time [Eq. (1.89)], in the particular case of a turbulent power spectrum $P(k) \propto k^{-3/2}$, can be written as

$$\tau_{acc} = \frac{p^2}{4D_{pp}} \approx 2.5 < \frac{\beta_{pl}|B|^2}{16\pi W} >^{-1} f_x^{-1}(\frac{M_0}{1/2})^{-4}(\frac{L_0/300\ kpc}{c_s/1500\ km\ s^{-1}})\ Myr \tag{1.89}$$

where $\beta_{pl} = 2c_s^2/v_A^2$, $< |B_k|^2/W >= 16\pi/\beta_{pl}$, where W is the total energy in the turbulent modes and $f_x \approx 0.02$ (G. Brunetti 2016).
However, in the case of radio bridges G. Brunetti and F. Vazza (2020) have proposed another mechanism based on non-resonant turbulent re-acceleration. This scenario assumes that relativistic particles scatter with magnetic field lines diffusing in super-Alfvénic turbulence, which are in turn amplified in the region by the same turbulence. In this model the diffusion coefficient in the particle momentum space [Eq. (1.90)], from which it is possible to obtain τ_{acc} is

$$D_{pp}(k) \approx \frac{48}{c}\frac{F}{\rho_{ICM}v_A}p^2 \tag{1.90}$$

where F is the turbulent energy flux (G. Brunetti and F. Vazza 2020). We will see more about this in Chapter 3.
We can also make use of the diffusion coefficient from Eq. (1.85) to determine the evolution of CRe populations by using the Fokker-Plank equation, that being

$$\begin{aligned}\frac{\partial N_\pm(p,t)}{\partial t} = \frac{\partial}{\partial p}(N_\pm(p,t)[S_\pm(p) - \frac{p}{3}(\nabla\cdot V)])+\\ \frac{\partial}{\partial p}(D_{pp}\frac{\partial N_\pm(p,t)}{\partial p} - \frac{2}{p}N_\pm(p,t)D_{pp}) + C_\pm\end{aligned} \tag{1.91}$$

where + and − indicate if Eq. (1.91) is referring to CRp or CRe, $S_\pm$ are the net energy losses for the two types of CR and $C_\pm$ is a term that is $-N_+(p,t)/\tau_+$ for

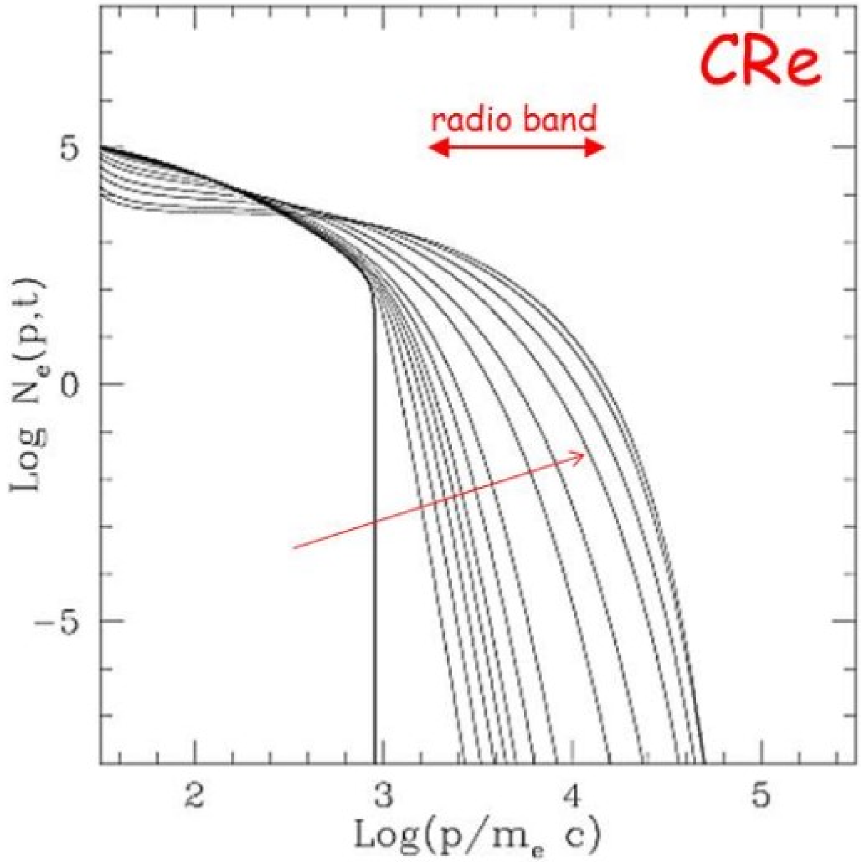

Figure 1.19: Time evolution of a CRe population as a function of its momentum, with a continuous injection of CR (G. Brunetti and T. W. Jones 2014);

the escape rate of primary CRp or it is $Q_-(p,t)$ for the injection of secondary CRe, with $\tau_+ = (n\sigma_{++}c)^{-1}$ being the time-scale of proton-proton collision in the ICM (G. Brunetti and F. Vazza 2020).
We can now use Eq. (1.91) to determine the evolution of the particle distribution with time and in Fig. (1.19) we see an example of it; the population of CRe subtracts energy from the turbulent medium, thus increasing in number up until the energy losses do not become excessively high.
In general, a Fermi II mechanism has to carefully consider whether the acceleration times are bigger than the loss time-scales, as they usually are, and if they are indeed so, a continuous injection of accelerated particles may be needed to explain the presence of radiation, even if the entity of the filling factor may solve the issue in some cases.

Chapter 2

The scientific case of radio bridges

Cosmic Web filaments are yet to be observed, however, in recent years filaments of hot gas connecting galaxy clusters in a pre-merger phase have been observed. This new class of phenomena has been referred to as *radio bridges* and even though they are not believed to provide the physical characteristics for Cosmic Web filaments, radio bridges are the type of structure which is closest to them.

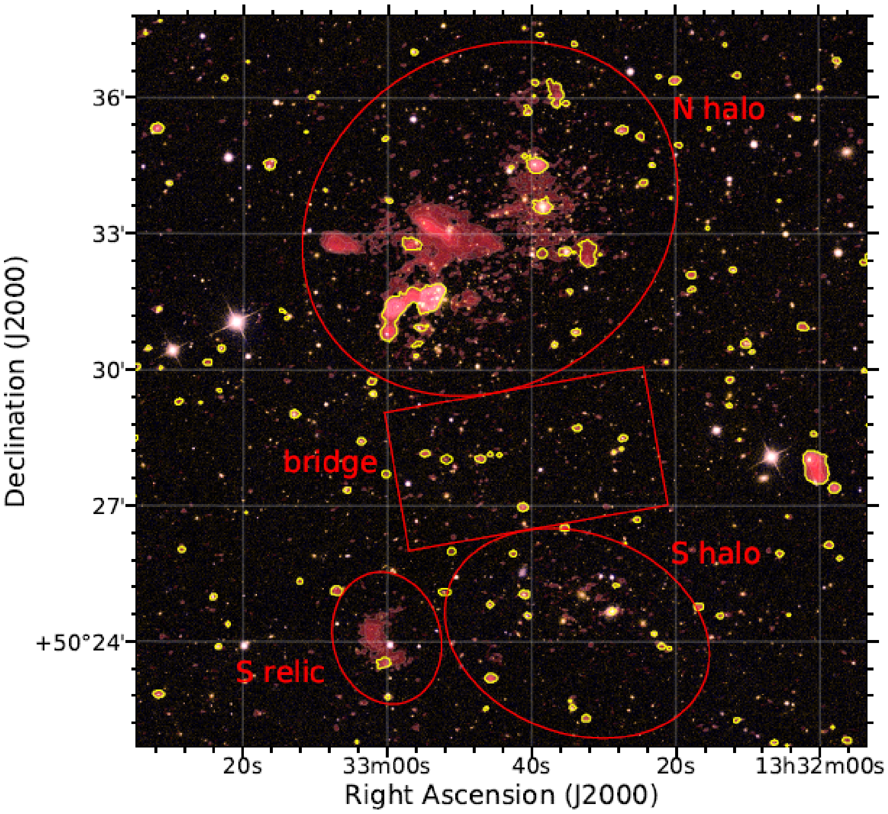

Figure 2.1: Radio bridge A1758N-A1758S observed with LOFAR at 144 MHz (A. Botteon and al. 2020);

Assuming that they are indeed similar in their nature, we can attempt to investigate the physical parameters of filaments even in previous phases and not only in their radio bridge phase. In this Chapter we will see how radio bridges have been observed and what models have been attempted to describe the nature of this extended filament structures.

2.1 Radio bridge observation

Radio bridges are a newly discovered class of extended cosmic radio sources that emit diffuse X-ray and radio light connecting two clusters in a pre-merger phase. They have been recently discovered by LOFAR observations and they have been seen to extend on scales larger than the clusters themselves; the most famous bridges are A399-A401 and the bridge connecting A1758N and A1758S.

A1758N-A1758S and A399-A401 bridge

I briefly show the first example, A1758N-A1758S, in Fig. (2.1) where the bridge between the two clusters has been observed with LOFAR (A. Botteon and al. 2020). However this work is focused on A399-A401, as it is the most spectacular

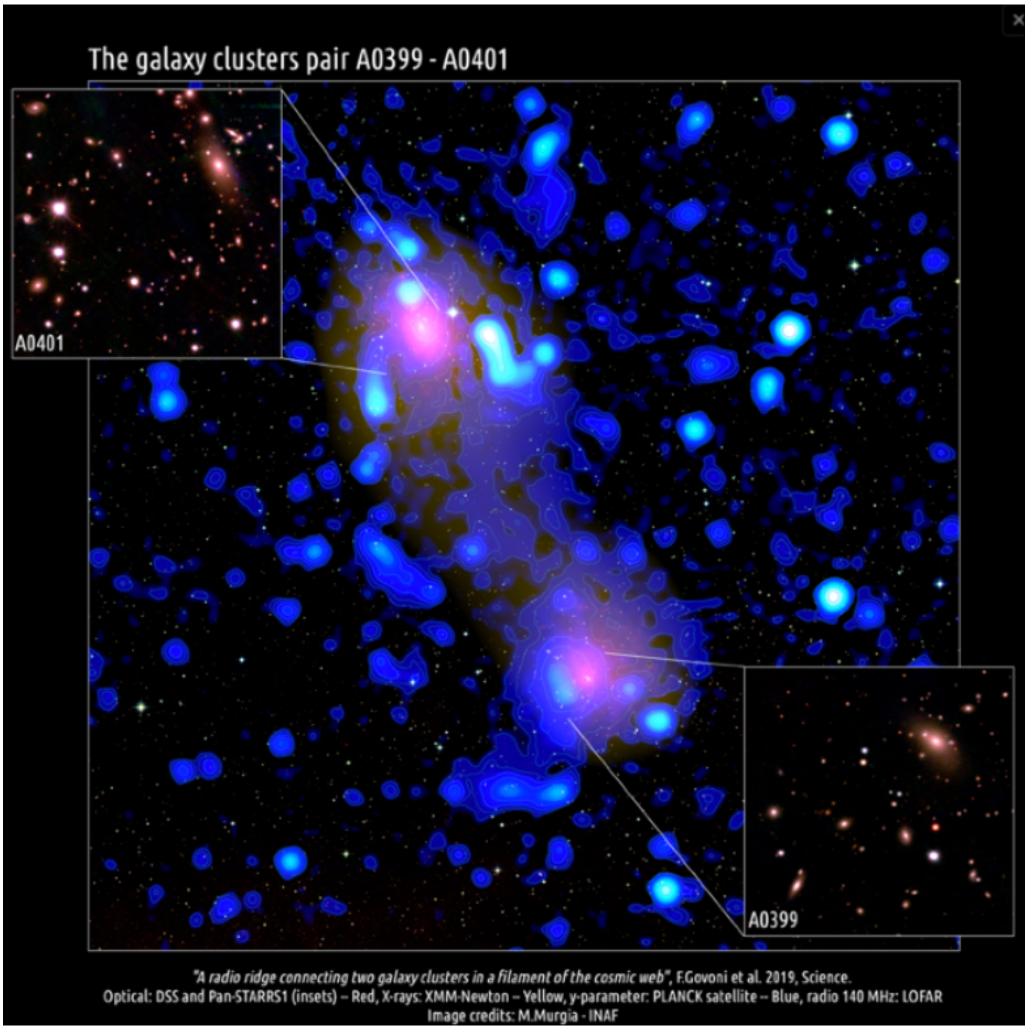
The galaxy clusters pair A0399 - A0401

"A radio ridge connecting two galaxy clusters in a filament of the cosmic web", F.Govoni et al. 2019, Science.
Optical: DSS and Pan-STARRS1 (insets) – Red, X-rays: XMM-Newton – Yellow, y-parameter: PLANCK satellite – Blue, radio 140 MHz: LOFAR
Image credits: M.Murgia - INAF

Figure 2.2: A399-A401 as observed in the X-ray (red) and the radio (blue) bands;

between the two, so I will move onto that.

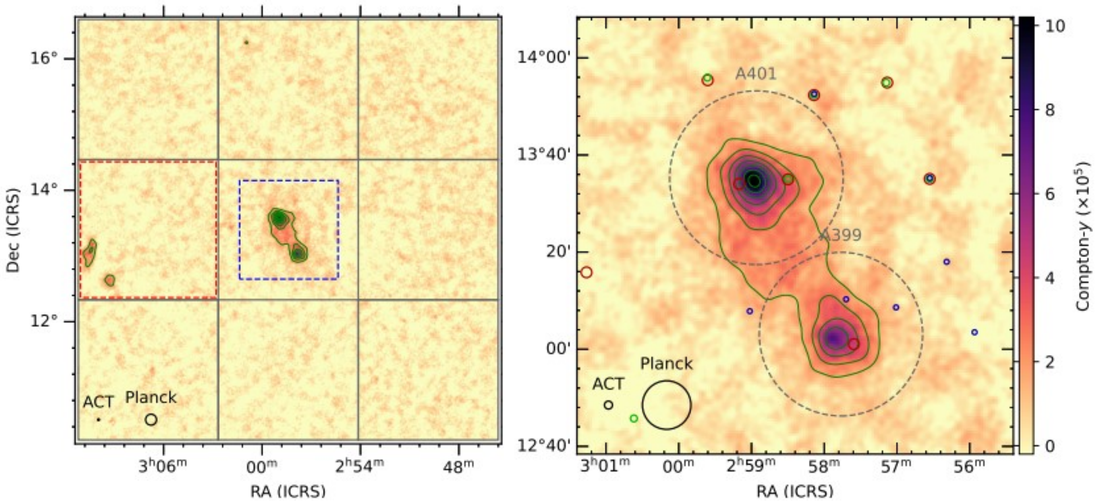

Figure 2.3: Compton map of A399-A401 observed with ACT and *Planck* (A. D. Hincks and al. 2022);

Abell 399 (RA=02h57m56s; DEC=+13°00’59”) and Abell 401 (RA=02h58m57s; +13°34’46”) are two galaxy clusters in an early merger phase joined by a luminous bridge that has been observed with LOFAR, with:

- a central frequency of 0.14 GHz
- a sky projected length of 3 Mpc
- a width of 1.3 Mpc
- a flux density of 822 mJy, to which corresponds a radio power of 10^{25} W/Hz

as reported in F. Govoni and al. (2019).
In Fig. (2.2) we can see an image of the bridge as seen in both the X and the radio bands, in particular the amount of SZ emission is predominantly produced by the two clusters. Fig. (2.3) shows one of the most recent images of the bridge as a Compton map obtained with *Planck* data, where the presence of radiation in the bridge becomes more evident.
To explore in more detail what we are expecting from this type of phenomena, let us consider what are some of the expected characteristics of Cosmic Web filaments and some of the main techniques applied to try and observe them.

2.1.1 X-ray observation of radio bridges

Filaments are thought to host a hot diffuse baryonic gas with a temperature of $10^5 - 10^7$ K. On the other hand, the magnetic field level in filaments is much less constrained and, from theoretical viewpoints, a large range of values spanning from roughly 10^{-3} nG to 0.1 μG, is possible, at least in principle (C. Gheller and F. Vazza 2019). However, the recent modelling of radio detection through stacking emission from Cosmic Web filaments has been used to derive typical values of magnetic field

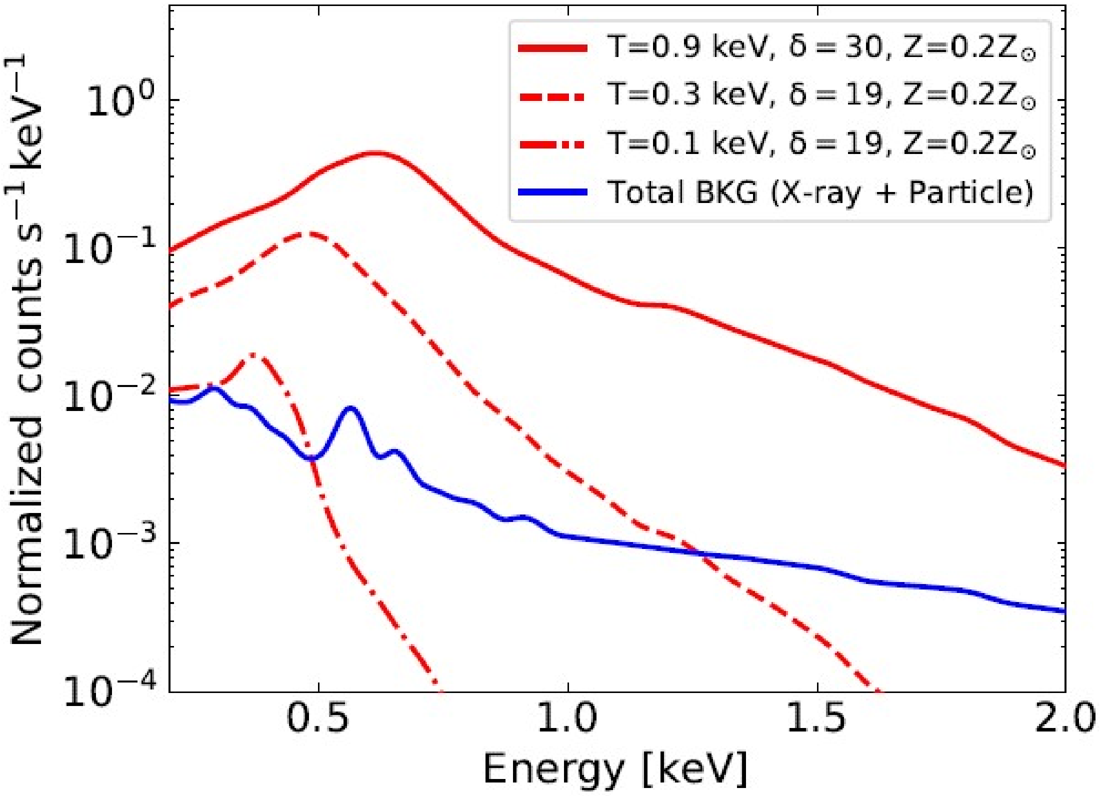

Figure 2.4: X-ray stacking simulated spectrum from gas cores in filaments; the red profiles are simulated spectra for different combination of gas temperature and gas overdensities, the blue profile is a simulated background spectrum (H. Tanimura and al. 2020);

strength of $30 \leq B \leq 60nG$, that in turn may cause synchrotron emission through interaction with a CR population in the region (T. Vernstrom and al. 2021). CR may not be present in the region, however the increasing number of observation of synchrotron emission by independent studies (e.g. F. Govoni and al. 2019; T. Vernstrom and al. 2021) bolsters the hypothesis of a CR population inside radio bridges, even though its acceleration mechanism remains largely unknown. Nonetheless various X-ray observations have been attempted and have been successful.

One exemplary technique used to identify the X-ray emission of radio bridges is X-ray stacking (e.g. H. Tanimura and al. 2020; T. Vernstrom and al. 2021; T. Hodgson and al. 2022). For example, the study of H. Tanimura and al. (2020) utilized 15165 filaments with $0.2 < z < 0.6$ identified with the Sloan Digital Sky Survey (SDSS), then the count-rate maps from $ROSAT$ data used to break the degeneracy between gas density and temperature were stacked, subtracting signals from resolved galaxies and point-like sources independently identified by $Chandra$, $XMM-Newton$ and $ROSAT$. The result was the identification of an X-ray signal with a significance of roughly 4σ in the $0.56-1.21$ keV band (H. Tanimura and al. 2020).

In Fig. (2.4) we may see an example of X-ray stacked simulated spectra, that showcases the important role of the gas temperature-density degeneracy, which can be lifted by independent observations, although the extended and faint nature of filaments is a substantial obstacle to other kind of observational techniques. In particular, as the energy increases so does the difference between different models, even to several orders of magnitudes, resulting eventually in the simulated X-ray emission to fall under the simulated background emission. Perhaps due to this reason, no emission in other bands was observed (H. Tanimura and al. 2020); higher energy bands are more likely to produce only a faint emission that is suppressed by the noise, inhibiting our chances to explore those energies, at least for most of our current instruments.

Another X-ray stacking study uses pairs of Luminous Red Galaxies (LRG) as probes for the presence of Cosmic Web filaments (T. Vernstrom and al. 2021). LRG are usually located in the center of galaxy groups or clusters and the stacking of their emission, together with the subtraction of the estimated background and halo emission can provide us with a relevant signal from the filaments between the pairs of LRG. This results in an X-ray signal in concordance with cosmological thermal simulations and even 5 times higher than the signal predicted by H. Tanimura and al. (2020); also it allowed the identification of a radio signal with a spectral index of $\alpha = -1.0$ (T. Vernstrom and al. 2021). However the stacking technique does not always allow the observation of both X-ray and radio emission, as other works have attempted to replicate the one of T. Vernstrom and al. (2021) but only managed to replicate the X-ray stacked images and not the radio ones (T. Hodgson and al. 2022).

Another way to investigate the X-ray emission of a filament resides in the thermal Sunyaev-Zel'Dovich (tSZ) effect, so a frequency dependent distortion of the Cosmic Microwave Background (CMB) spectrum by IC; its entity depends on the Compton y-parameter, in Eq. (2.1)

$$y = \frac{\sigma_T}{m_e c^2} \int n_e(r) k_B T_e(r) dr \tag{2.1}$$

where $n_e(r)$ is the distribution of electrons (A. D. Hincks and al. 2022). In particular, this effect produces a variation in the CMB temperature, that being

$$\Delta T = T_{CMB}\ y[\frac{h\nu}{k_b T_{CMB}}\ coth(\frac{h\nu}{2k_b T_{CMB}}) - 4]. \tag{2.2}$$

A measurement of the temperature variation, in Eq. (2.2), therefore results in an estimate of the population of particles in the region, since from Eq. (2.1)-(2.2) we gain information on both the distribution of particles $n_e(r)$ and their temperature $T_e(r)$, even if without other independent observation there is a degeneracy between the two.

In the A399-A401 bridge, using a temperature-map taken by *Suzaku*, this technique allowed to constrain the mass of the bridge to $(3.3 \pm 0.7)10^{14}\ M_\odot$, which is around 8% of the total mass of the pair A399-A401 (A. D. Hincks and al. 2022). A previous work, instead estimated a mass of $7.7\ 10^{13}\ M_\odot$, together with a Compton y-parameter of $(14.5 \pm 1.3)10^{-6}$ for the filament and a metallicity $\approx 0.3\ Z_\odot$; spectral modelling for X-ray sky sources, X-ray background and X-ray from the filament were used (H. Akamatsu and al. 2017).

Observations in the X-ray with *Suzaku* have further allowed the formation of a simple model predicting an angle of 16.6 $(-3.8, \ +5.5)$ degrees between the line of sight and the axis of the bridge. This result is still uncertain, but it were true that would mean that the distance between A399 and A401 would not be of 3.2 Mpc but of 11.1 $(-2.6, \ +3.2)$ Mpc , meaning that the bridge would have a significant component along the line of sight and could be treated like a Cosmic Web filament (A. D. Hincks and al. 2022). However, if the bridge were this extended then it would be harder to explain the temperature of 10^8 K of the gas measured in the bridge, that would be one order of magnitude higher than the predicted temperature of a classical filament.

In this work, I have made my analysis with the conservative assumption that the projected distance of ≈ 3 Mpc between A399-A401 and the physical length of the bridge are of similar size.

2.1.2 Radio observation of radio bridges

As above mentioned, one technique to infer the presence of radiation in a radio bridge is stacking, however this technique is not easily performed. In this section I will instead focus in direct observations of radio emission. In particular, two works (F. Govoni and al. 2019; A. Botteon and al. 2020) used LOFAR observations at 140 MHz, with the addition of 53 MHz emission in A. Botteon and al. (2020) that focuses however on the bridge A1758N-A1758S and therefore I will only cite as similar in deployed techniques to the work of F. Govoni and al. (2019), that is my main focus. Another work worth mentioning studied the region of the bridge A399-A401 at 140 MHz and 346 MHz, observing radio emission for both of the frequencies (C. D. Nunhokee and al. 2022). Fig. (2.5) shows a radio image of A399-A401 as obtained from LOFAR at 140 MHz, where the presence of radio emission between the two clusters is evident when compared to the radio emission of surrounding background regions.

The parameters of reference for the bridge A399-A401 in this Thesis come primarily from F. Govoni and al. (2019). In addition to the ones already reported in Section (2.1), I may add that no spectral index was derived in F. Govoni and al. (2019), and also that the emissivity of A399-A401 is a few orders of magnitude lower than the emissivity of the average filament candidate, and that at 1.4 GHz the radio emissivity is $\approx 4.3 \ 10^{-44} erg \ s^{-1} Hz^{-1} cm^{-3}$, assuming that $\alpha = 1.3$. In Section (2.2) I will report how F. Govoni and al. (2019) used shock models to describe the nature of the bridge.

The observation of A399-A401 by C. D. Nunhokee and al. (2022), instead focuses more on the A399-A401 cluster pair, observed at various wavelengths, allowing an estimate of α for the cluster pair and its connecting radio bridge between 140 MHz and 346 MHz with the Westerbork Synthesis Radio Telescope (WSRT). In particular for A399 it has been estimated that $\alpha = 1.75 \pm 0.14$, however this is not the case for the bridge: as we can glean from Fig. (2.6), while contours at 140 MHz show the presence of the bridge, in the 346 MHz image of the region there is no clear evidence of a bridge, since the emission falls under the noise intensity (C. D. Nunhokee and al. 2022). To help and constrain a spectral index value for this re-

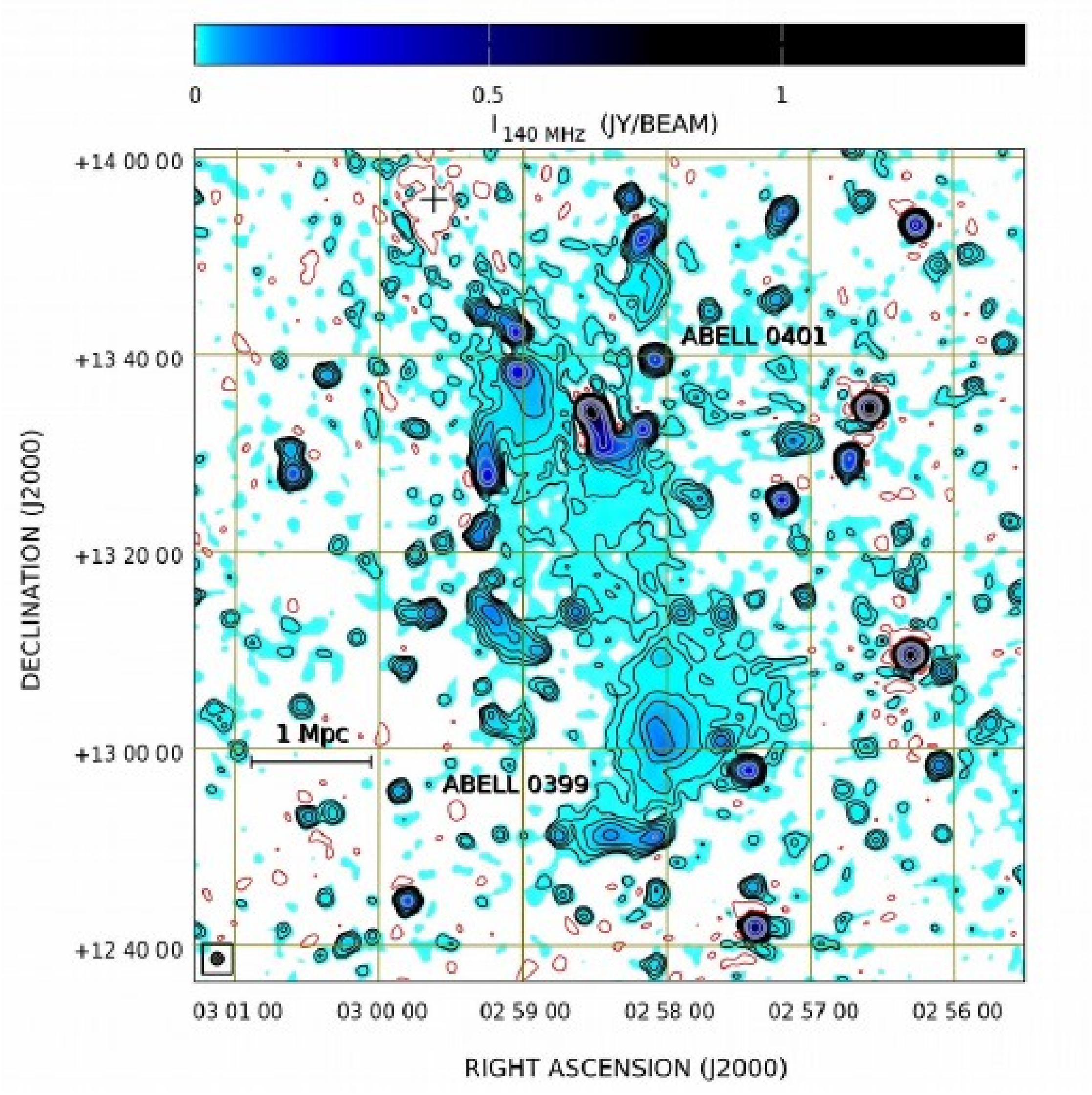

Figure 2.5: Image of the A399-A401 bridge observed with LOFAR at 140 MHz (F. Govoni and al. 2019);

gion, an upper limit for the flux density of the bridge, and therefore a lower limit on α has been investigated through extrapolation of the LOFAR image at 140 MHz. The result is a lower limit on the spectral index of the bridge of $\alpha > 1.5$ at 95% confidence level (C. D. Nunhokee and al. 2022).

Another recent study worth mentioning has investigated the local spatial correlations in the bridge A399-A401 between radio data, X-ray data and the SZ map, which has allowed to better constrain the magnetic field scaling index η, that being the slope of the profile $B(r) \propto n_e(r)^\eta$ for the injection and re-acceleration models (F. Radiconi and al. 2022). If F_{radio} is the measured radio brightness, F_X is the X-ray count rate per solid angle unit and y is the Compton y-parameter, then this quantities are correlated and they follow the relations in Eq. (2.3)-(2.4)-(2.5), which are respectively

$$log(F_{radio}) \propto 0.7 \; log(F_X) \tag{2.3}$$

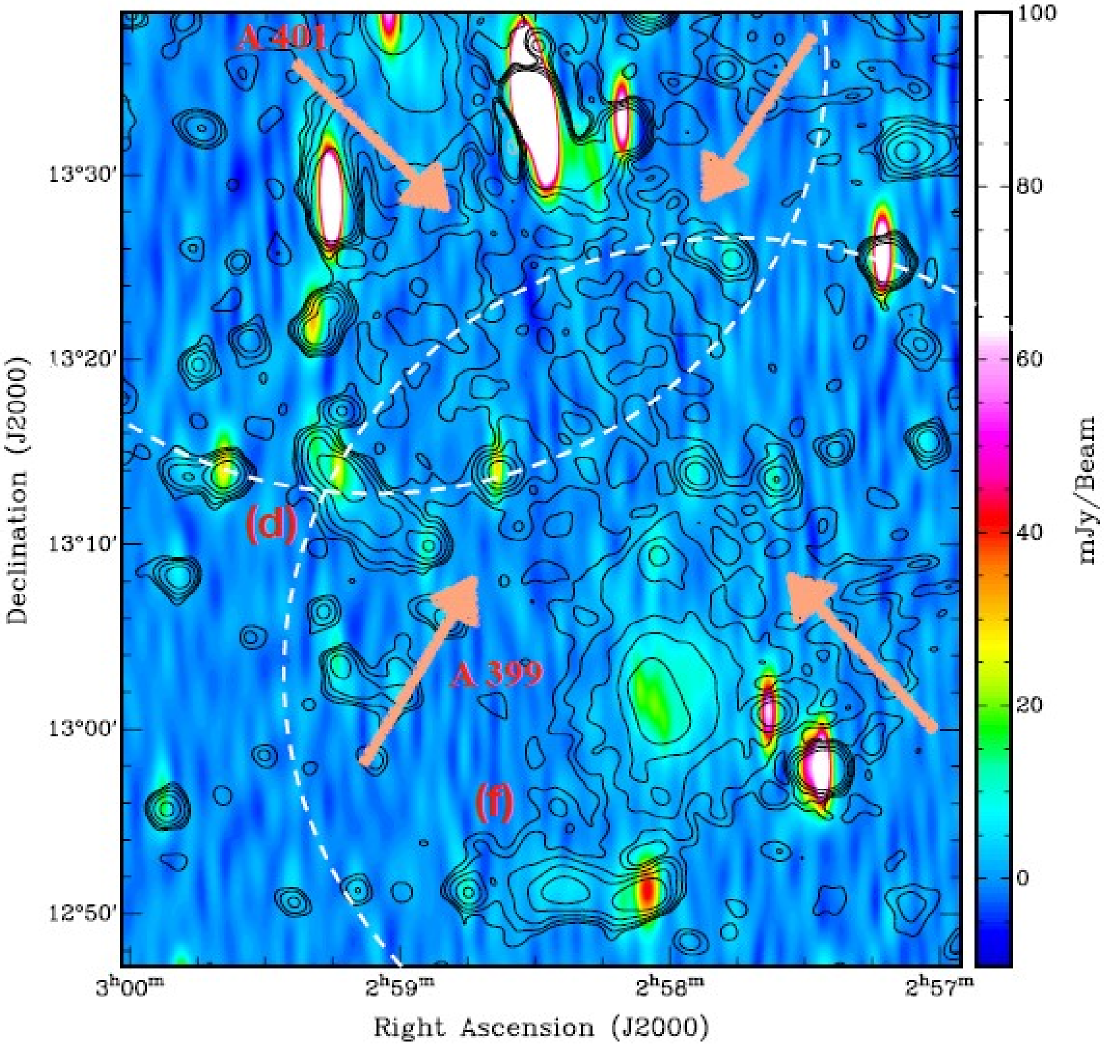

Figure 2.6: Image of A399-A401 cluster pair at 346 MHz with 140 MHz contours overlaid to it; the arrows point at the bridge observed at 140 MHz (C. D. Nunhokee and al. 2022);

for the correlation between the radio brightness and the X-ray count rate,

$$log(F_{radio}) \propto \begin{cases} 2.8\ log(y) & ,\ for\ A399 \\ 1.5\ log(y) & ,\ for\ A401 \end{cases} \tag{2.4}$$

for the correlation between the radio brightness and the y-parameter, and

$$log(y) \propto 0.5\ log(F_X) \tag{2.5}$$

for the correlation between the y-parameter and F_X (F. Radiconi and al. 2022). Using the radio, X-ray and SZ correlations it was possible to define the slope of the radial dependence profile of magnetic fields, and in particular it is between $\eta \approx 0.6 - 0.8$ (F. Radiconi and al. 2022). Although this result is not of particular relevance for my Thesis work, I decided to report it, since it is from one of the latest articles on the matter of the A399-A401 bridge.

Now that we have seen some of the main characteristics of the phenomena we can move on to the various theories that may describe the particular nature of radio bridges. I will focus on particle acceleration models, in particular Fermi I and Fermi II that, respectively, find in shock re-acceleration and turbulent re-acceleration of a population of CRe the means via which these electron can reach relativistic energies and emit by a synchrotron process.

2.2 Shock model for A399-A401 radio bridge

In this section, I will report the DSA acceleration model that F. Govoni and al. (2019) have applied to the bridge A399-A401, with the aim of showing what are the main results from this model and its main limitations.

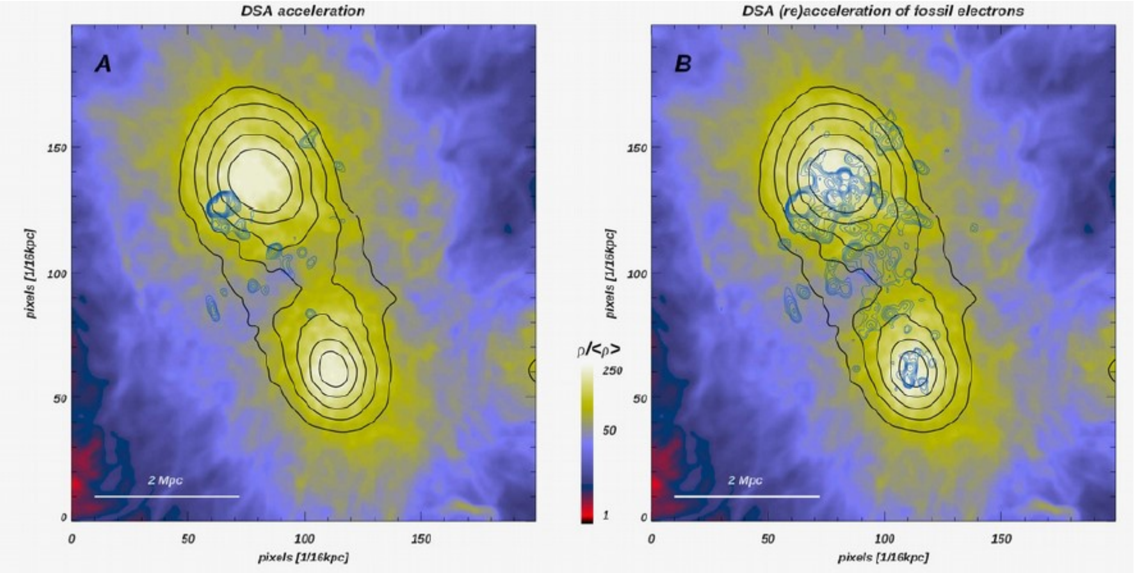

Figure 2.7: Image of the system A399-A401 coloured for its gas density, with black contours from SZ radiation and blue contours from radio emission; the left panel shows the simulated emission for a DSA model for injected electrons, while the right panel shows the simulated emission for a DSA model for a fossil population of relativistic electrons (F. Govoni and al. 2019);

First of all, the pair A399-A401 is in an early stage of merger, where the two clusters are yet to collide, however the presence of radio emission already indicates that a portion of the energy of the merger has been transformed into non-thermal energy. The origin of this emission, in this model, is likely due to CRe that are accelerated via shock waves prior to the merging of the clusters (F. Govoni and al. 2019).
Assuming a homogeneous gas density of roughly $3\ 10^{-4} cm^{-3}$ in the bridge, with a magnetic field less than $1\ \mu G$, we have that the energy losses from synchrotron and IC emission [Eq. (1.16)-(1.28)] cause the life-time of CRe in the region to be only less than $230\ Myr$, which is too low to allow the electrons to cross even a small fraction of the bridge. It is therefore necessary to include a mechanism of continuous injection or re-acceleration of electrons that happens *in situ*.

Let us first consider an injection of new CRe in the region, in this case the emission of the bridge is difficult to describe with a DSA model that accelerates a freshly injected population of electrons, as shown by MHD simulations with $ENZO$ code. In particular, we have that for an isothermal plasma of $\approx 5\ 10^7\ K$ and CRe acceleration only for $M > 3$, the produced radio emission is 1000 times lower than the LOFAR observation, with only the region transverse to the line of sight capable of emitting a detectable emission due to a weak shock (F. Govoni and al. 2019). However, this model does not reproduce the observed emission of the bridge, which is shown in the left panel of Fig. (2.7), and therefore we can move on to consider the next option.

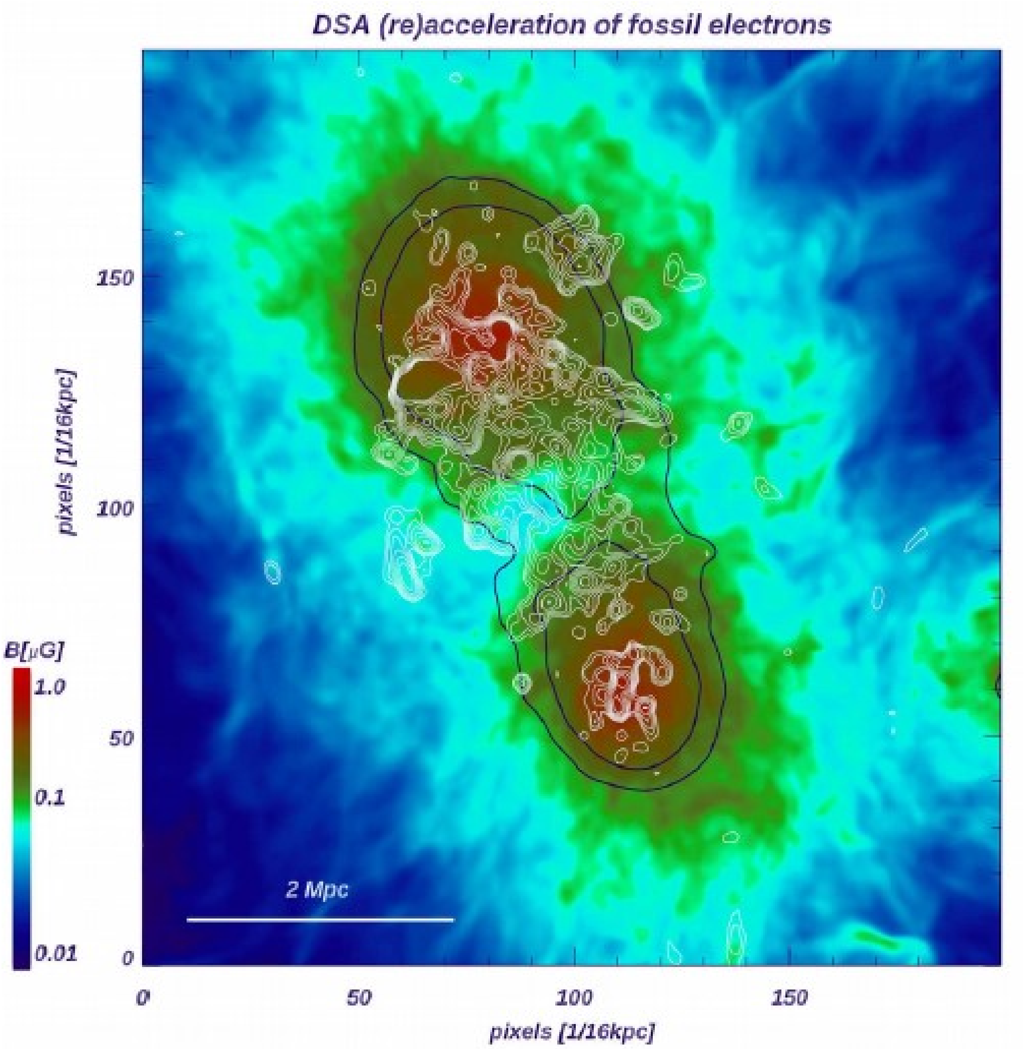

Figure 2.8: Magnetic field distribution for the pair A399-A401; black contours represent SZ emission and white contours represent the simulated radio emission for a DSA model for a re-accelerated population of CRe (F. Govoni and al. 2019);

Still in a DSA model, now it is applied to a fossil population of relativistic electrons that is then re-accelerated to higher energies by shocks happening *in situ*. To meet the necessary requirements, the bulk of the pre-existing population should have a $\gamma \geq 10^3$, which would mean a life-time of roughly 1 Gyr, and it should be re-accelerated by shocks with $M \approx 2-3$. This results in an increment to the DSA acceleration efficiency, that it has been estimated by adding to the standard acceleration efficiency a contribution based on the predicted CRp acceleration efficiency and by assuming a ratio between CRe and CRp energies of 10^{-3}; in particular the acceleration efficiency, which is a function of the Mach number and the temperature of the gas, goes from 10^{-7} to 10^{-5} (F. Govoni and al. 2019). The life-time of the population is, however, still too short so the need for injection of new electrons remains.

Fig. (2.7) shows, in the right panel, the simulated radio emission in blue contours and it can be inferred that it can reproduce the observed emission more accurately than the one due to the previous model of pure injection of new electrons, that is incapable of reproducing the observed emission for a large enough portion of the bridge. In Fig. (2.8) we see instead the distribution of the expected magnetic fields, that can go up to the 0.2 μG mark, over the region of the bridge, where the white contours represent the simulated emission from a DSA model for a pre-existing population of fossil electrons, since it is the most likely model between the two that are shown in this section. The maximum expected magnetic field strength in A399-A401 bridge is of 0.2 μG, as above mentioned, and I will later use its value as a limit to check the likelihood of a Fermi I acceleration model to describe the emission from the bridge, as we will later see in Chapter (3).

2.3 Turbulence model for A399-A401 radio bridge

Another way in which we can hypothesize the nature of the bridge A399-A401 is through a Fermi II turbulent acceleration model, and in this section I will particularly focus on the analysis perpetuated by G. Brunetti and F. Vazza (2020).

In their work, they simulated the emission produced from a pre-existing population of CRe that is then re-accelerated by super-Alfvénic turbulent motions caused by the diffusion of magnetic fields. In particular, Magneto-HydroDynamic (MHD) simulations with *ENZO* code have been attempted to provide a first estimate of the distribution of magnetic fields in a simulated pre-merger galaxy cluster system similar to A399-A401, together with the turbulent energy flux distribution, 60% of which is due to solenoidal motions. These motions in the ICM usually allow the amplification of local magnetic field, however, in a radio bridge the dynamo process, which is responsible for the amplification, cannot be studied through the same simulation because of the limited resolution of it. Nonetheless, the resulting turbulent luminosity from the simulation is of the order of $FV \approx 10^{45}\ erg\ s^{-1}$, which is comparable in magnitude to the luminosity of a merger event, and where $F = 1/2\ \rho_{ICM}\delta V^3/L$ is the turbulent energy flux with a turbulent injection scale of roughly $400\ kpc - 1\ Mpc$ (G. Brunetti and F. Vazza 2020).

An estimate on magnetic field strength can be attempted separately, hypothesizing that after a turbulent eddy reaches its dissipation scale then a fraction of its energy is converted into magnetic field strength, thus amplifying it. Two regimes of growth may be identified for the magnetic fields, a relatively quick exponential regime and a successive linear regime, where in Eq. (2.6) we see the time needed for the transition between the two regimes:

$$\Delta T \approx 60\tau_e Re^{-1/2} ln(\frac{\sqrt{4\pi\rho_{ICM}}\delta V}{B_0 Re^{1/4}}) \tag{2.6}$$

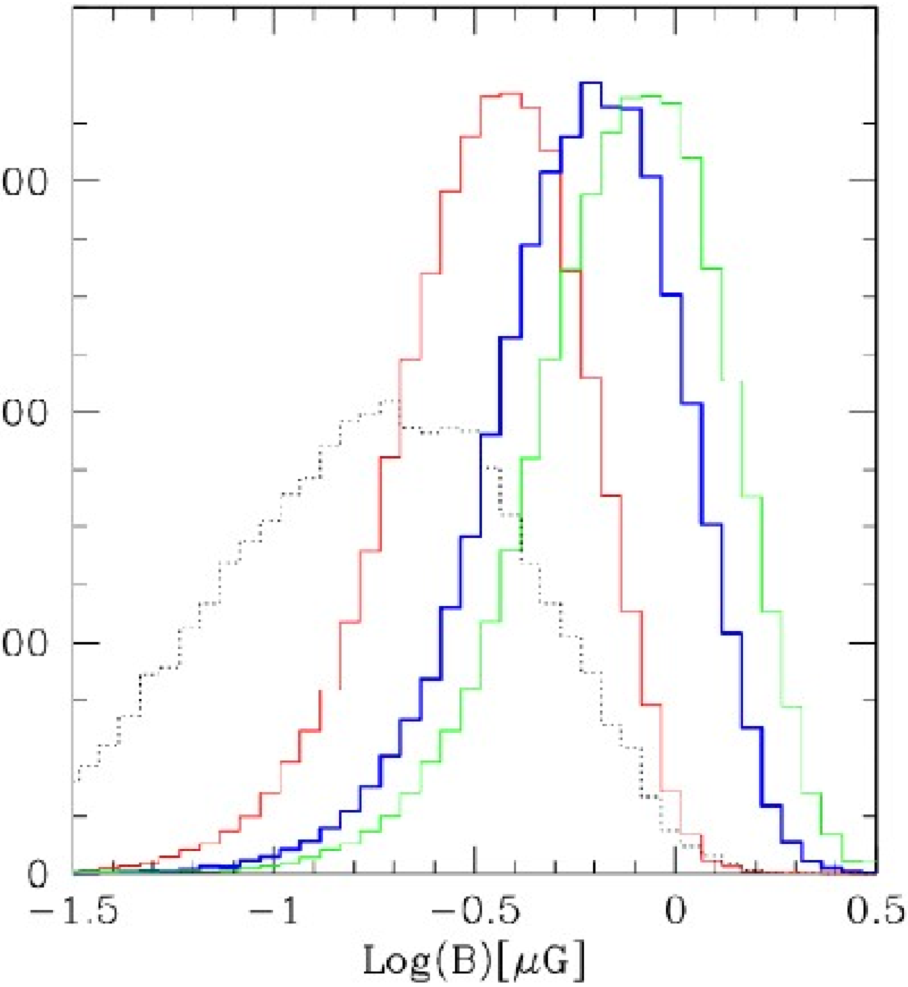

Figure 2.9: Magnetic field distribution for $\eta_B = 0.02,\ 0.03,\ 0.05$, respectively the red, blue and green profiles; the dotted grey line is the seed magnetic field distribution of the simulation (G. Brunetti and F. Vazza 2020);

where Re is Reynolds' number, ρ_{ICM} the density of the ICM and τ_e is the turnover time of an eddie. The transition time in Eq. (2.6) is smaller than a time-scale τ_e for a $Re > 1000$ and since for magnetic fields of the order of 0.1 μG we find ourselves in this regime, the exponential growth phase for the magnetic fields can be neglected. The amplification of magnetic fields provides different results, that we can see in Fig. (2.9), depending on the efficiency of the dynamo process η_B, which is the fraction of turbulent kinetic energy that is responsible to the amplification of B. In particular, G. Brunetti and F. Vazza (2020) take η_B as being 0.02, 0.03 and 0.05.
The mean magnetic field reached with this simulation is $0.5 - 0.6\ \mu G$ which is three or five times smaller than the typical magnetic field strength in an ICM, meaning that the ratio between thermal and magnefic field pressure $\beta_{pl} = P_{th}/P_B \approx 100-200$ is a bit larger than the one for the typical ICM (G. Brunetti and F. Vazza 2020). Also, since the life-time of $1 - 1.5\ Gyr$ of radio bridges is relatively short, we have that it is only slightly larger that the eddy turnover time of $0.4-1.0\ Gyr$. Therefore the assumption that magnetic fields can be amplified in only an eddy turnover time

is reasonable.
In Chapter (3), I will later use this magnetic field value as a limit to infer the likelihood of the Fermi I acceleration model that I will introduce. Although the estimate on magnetic field has been obtained for a Fermi II re-acceleration model, we can still use it to gain an idea on the likelihood of certain magnetic field strengths. In particular if a magnetic field for a model is higher than the ones predicted by G. Brunetti and F. Vazza (2020) and F. Govoni and al. (2019) then the prediction on magnetic fields of the new model, in Chapter (3), would be unlikely.

Chapter 3

Constraints from the Inverse Compton flux

One first step to assess which models are the most adequate ones to explain the radio properties of the A399-401 bridge is to use the available IC limits from this region and to constrain different model's predictions on the average magnetic field in the region. Depending on the population of electrons, their distribution and injection spectrum, and the magnetic fields, we may obtain different theoretical limits on the IC luminosity for the different scenarios of cosmic rays acceleration. We can then compare them with the current observational constraints; if the predicted levels of IC luminosity are above the latter, then the model or the utilized set of parameters must be recalibrated, while otherwise they may provide a viable explanation to the emission in the region. Here we will mainly consider shock accretion models, and we will discuss what they imply on the nature of the local magnetic fields (G. Brunetti and T. W. Jones 2014).

3.1 Inverse Compton limits on Fermi I models

This chapter focuses on how to apply already defined models and processes to predict limits on the IC flux of the A399-A401 bridge. I begin by reporting the equations for the two main loss mechanisms in our energy range of interest ($0.1 - 2.4\ keV$), namely IC and synchrotron radiation, which may provide us with a clearer insight on how the possible configurations of parameters in our model influence the validity of the to be determined IC flux constraints.

The loss rate for IC and synchrotron emission may be written as

$$[\frac{dp}{dt}]_{rad} = -4.8\ 10^{-4}\ p^2[(\frac{B_{\mu G}}{3.2})^2 + (1+z)^4]\ \ s \tag{3.1}$$

where $B_{\mu G}$ represents the magnetic field of the bridge in units of μG, under the assumption of it being isotropic, where z is the redshift and where p is the momentum of CRe (G. Brunetti and T. W. Jones 2014). In particular Eq. (3.1) tells us that, at a fixed energy, the higher the magnetic field the bigger the losses. This also has an immediate impact on the lifetime of the CRe, which gets shorter with the increase in losses and it does especially so when we consider that in the bridge synchrotron emission is present, being one of the few observational measures on the region. Here, in Eq. (3.2) I show how the intensity of magnetic fields may influence the lifetime of the CRe population

$$[\frac{p}{dp/dt}]_{rad} \approx 10^4 \frac{1}{p[(\frac{B_{\mu G}}{3.2})^2 + (1+z)^4]} \quad s \tag{3.2}$$

so a $B_{\mu G} > 3.2$ will result in a short lifetime of the population, implying that it should be either continuously injected by new CRe or that the magnetic field estimate is too high to allow us to see synchrotron emission as we do in the bridge.

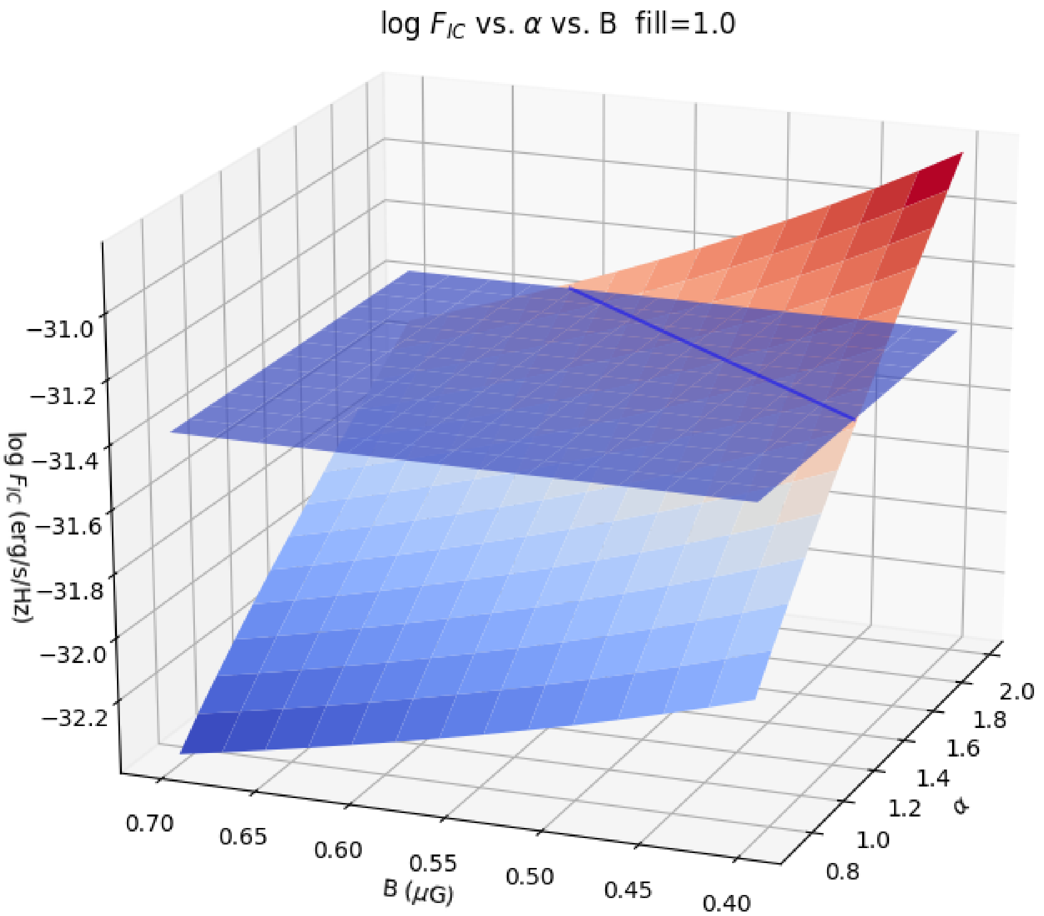

Figure 3.1: IC flux as a function of α and $B_{\mu G}$ with radiation being emitted by the whole volume (fill=1.0); the horizontal plane represents the current upper limit on the flux, represented by the inclined plane, while the blue line roughly signals which combinations of the free parameters meet that limit;

In the case of the A399-A401 bridge we are considering a system where ultra-relativistic CRe are undergoing IC scattering with CMB photons and are emitting synchrotron radiation. In the simplest scenario (e.g. following from direct shock acceleration of the radio emitting particles), we assume a powerlaw type energy distribution of the form $N(E) = K_e E^{-\delta}$, which provides us with a radio spectral index

$\alpha = (\delta - 1)/2$. We can link the IC flux with the observed synchrotron flux through the following relation:

$$\frac{F_{ICS}(\nu_X)}{\nu_{20keV}} = 1.38\ 10^{-34}\ (\frac{F_{syn}(\nu_R)}{Jy})\frac{(1+z)^{\alpha+3}}{\langle B_{\mu G}^{1+\alpha}\rangle}(\frac{\nu_X/keV}{\nu_R/GHz})^{-\alpha}\ C(\alpha) \tag{3.3}$$

expressed in c.g.s units (G. Brunetti and T. W. Jones 2014). The numerical factor derives from the current upper limit on IC emission; also we have that ν_X is the equivalent in erg of 20 keV, $\nu_R = 0.14\ GHz$, $F_{syn} = 0.822\ Jy$, and that the redshift of A399 is 0.071806 and that of A401 is 0.073664, so in our calculation we utilized a mean $z = 0.072735$ (F. Govoni and al. 2019).

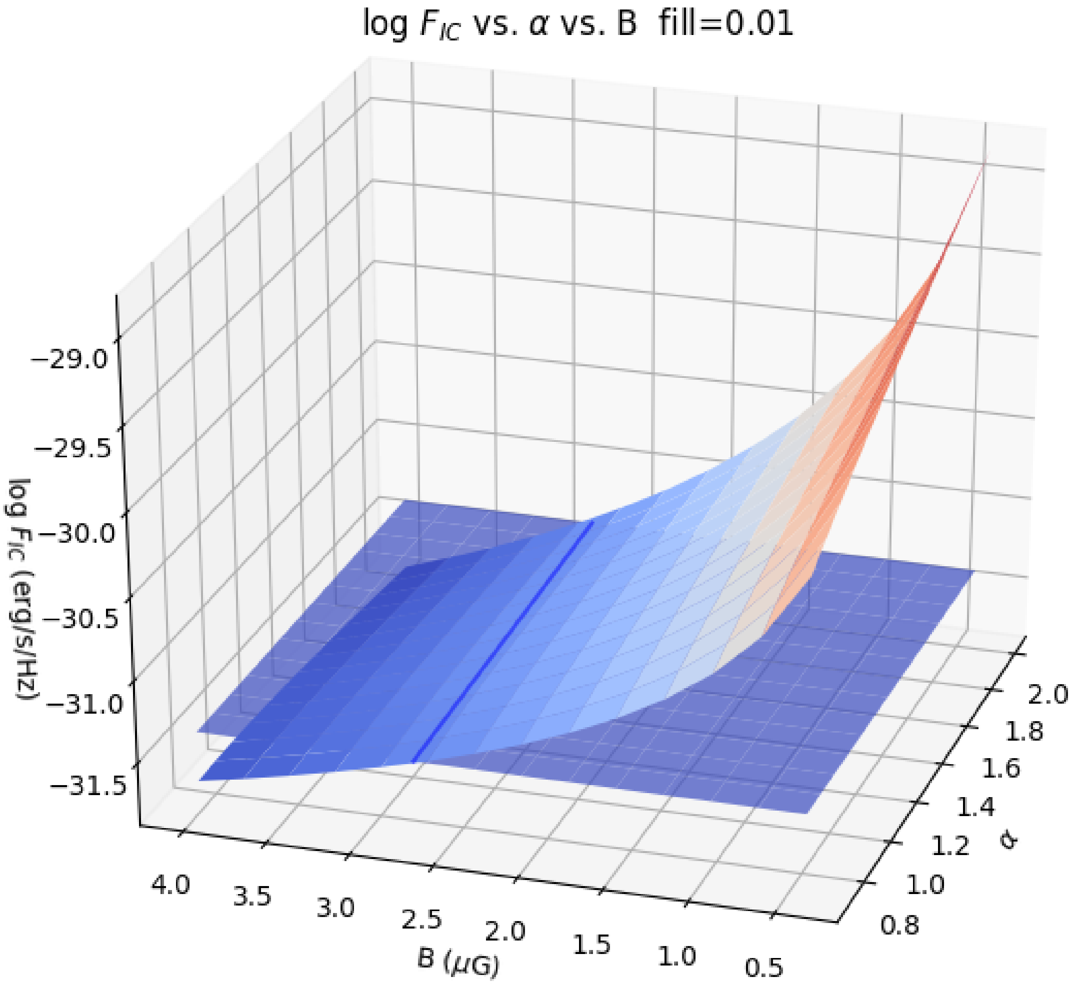

Figure 3.2: IC flux as a function of α and $B_{\mu G}$ with $fill = 0.01$;

Using Eq. (3.3), we analyzed how the IC flux varies in regards to both $B_{\mu G}$ and α, which are our most relevant free parameters. In particular, we consider values of α that range between 0.7 and 2.0, corresponding to values of $C(\alpha)$ given by Table 1 in G. Brunetti and T. W. Jones (2014). The observational limit that we used for the IC flux corresponds to $4.135\ 10^{-32}\ \ erg/s/Hz/cm^2$.

The behaviour of the IC flux can be seen in Fig. (3.1) and in particular we can see how it is below the observational limit if the combination of B and α is to the left of the segment in blue, $B = 0.35\alpha - 0.06$, that has for extremes ($\alpha = 1.3,\ B = 0.40$) and ($\alpha = 2.0,\ B = 0.65$), for a simple case in which we assume that the synchrotron emission is produced by the entire volume of the bridge, albeit this is probably an overly simplistic scenario.

We have also computed the IC flux for different values of the filling factor $fill$, a parameter describing which fraction of the volume we consider to be producing synchrotron radiation.

Since in a shock model we have that the shocks are roughly 2D surfaces that fill the extensive volume of the bridge we expect to obtain a few percentiles for the filling factor, and in particular MHD simulations suggest that for bridges of this nature we expect a $fill < 1 - 10$ %, this means that only a low portion of the bridge is able to produce synchrotron radiation that fills the entirety of the volume uniformly (G. Brunetti and F. Vazza 2020). At the same time the IC radiation is produced also by the remaining portion of the volume so to have correct estimates for the IC we multiply its flux for $1/fill$.

For brevity, we display with Fig. (3.2) only the case in which $fill = 1/100$, since it showcases the effect of a diminishing filling factor, so an increment in IC flux, and an issue associated with this first attempt at constraining $B_{\mu G}$ and α.

As we can see in Fig. (3.2) we meet our criteria, an IC flux less than the observational limit, roughly for $B < 3\ \mu G$ while there's almost no dependence on α. This is due to the fact that we are freezing one parameter while the other is allowed to vary and this causes the unwanted convergence of the IC flux around $B = 3\ \mu G$.

In general, an increasing magnetic field and a decreasing index α both cause a diminishing IC flux; concerning the expected values, since we are considering a shock model, we expect $\alpha = 1.3$, corresponding to a particle spectrum of $\delta = 3.6$. Also, since $\delta = 2(M^2+1)/(M^2-1)$, we expect a typical Mach number of $M = \sqrt{3.5}$.

Despite all of its limits, the analysis above still gives us a rough estimate of which values of $B_{\mu G}$ and α could replicate an IC flux that falls under the observational constraints for a powerlaw distribution of CRe. However a more complex test is needed.

3.2 Inverse Compton limits for powerlaw distributions

In this section I will consider how the IC flux varies as a function of the magnetic field B, while at the same time applying all our models on a volume of 1 Mpc^3, as a first estimate of the volume of the bridge. In particular I will study the case in which B remains constant over the whole volume and then I will move on to different distributions of the magnetic field over the bridge.

By assuming a powerlaw distribution we can define simple expressions for the IC and synchrotron flux, which in turn can be used in combination with the observed synchrotron flux of 0.822 Jy (or 10^{25} W/Hz at the luminosity distance of roughly 290 Mpc for this object, which gives a certain value of K_e) to define more realistic

values of K_e than the initial guess.
For the IC we have that

$$\frac{dE}{dt\ d\epsilon_1} = \frac{1}{\pi}\ \frac{r_0^2}{\hbar^3\ c^2} K_e (k_b\ T)^{\frac{\delta+5}{2}} F(\delta) \epsilon_1^{-\frac{\delta-1}{2}} \tag{3.4}$$

is the emissivity, where ϵ_1 is the energy of the scattered photons and $F(\delta) = 2^{(\delta+3)}\ [(\delta^2 + 4\delta + 11)/(\delta + 3)^2(\delta + 1)(\delta + 5)]\ \Gamma[\frac{1}{2}(\delta + 5)]\zeta[\frac{1}{2}(\delta + 5)]$ (G. R. Blumenthal and R. J. Gould 1970). In Fig. (3.3) I show the variation that the emissivity goes through when δ, and so the flatness of the spectrum, changes, in particular the difference is of 16 order of magnitudes and the steeper the spectrum the lower the emissivity. Also $\delta = 1$ is the discriminant between the δ for which the emissivity increases with the energy, lower δ, and decreases with the energy, higher δ. Between the values of δ considered for Fig. (3.3) I will take $\delta = 3.5$ for most of my successive analysis, as its the closest value to the 3.6 assumed by F. Govoni and al. (2019).

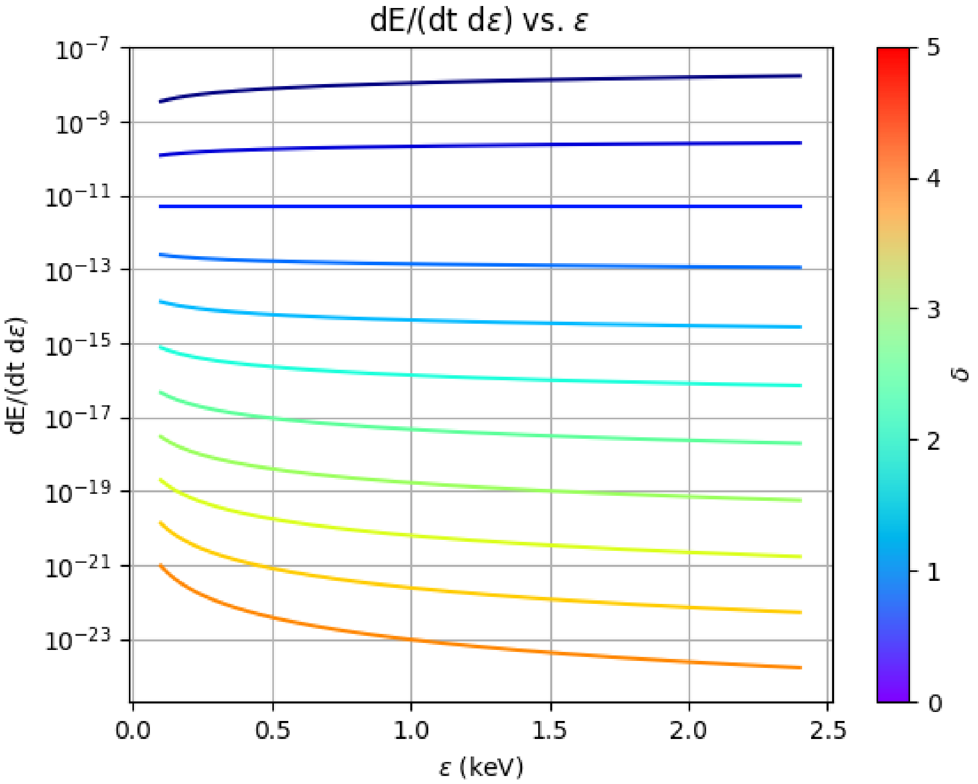

Figure 3.3: IC emissivity as a function of energy and δ;

Our observational constraint was measured in the energy range of $0.1 - 2.4\ keV$ by our collaborators (M. Balboni and F. Gastadello), that informed us through private communication. Our collaborators analyzed the XMM observation 0112260201, centered on the bridge and then extracted a spectrum from a box of 15×11 *arcmin*. Then, they modeled the background component of the spectrum and fitted the intercluster emission with a thermal component in the range $0.5-10\ keV$, finding a result

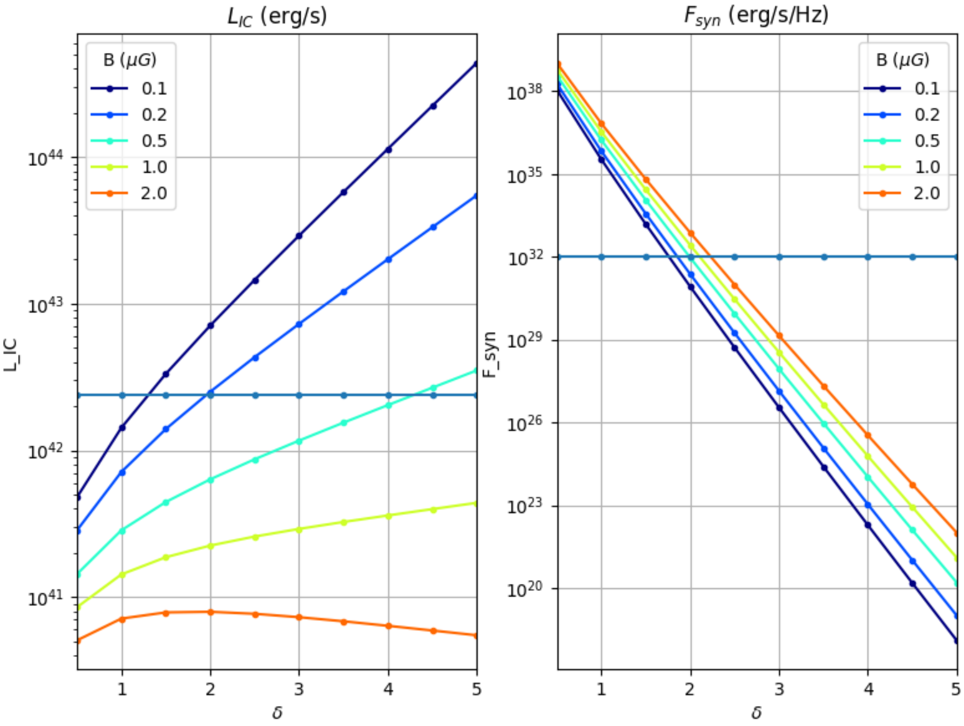

Figure 3.4: IC luminosity (left) and synchrotron flux (right) as a function of δ and $B_{\mu G}$, in the energy band $20-80$ keV. For L_{IC} each δ value has an associated K_e, while for F_{syn} we have assumed $K_e = 10^{64}$. The orizontal lines represent the observational limits for L_{IC} in the corresponding band and the observed F_{syn};

that agrees with the work of H. Akamatsu and al. (2017). Our collaborators have then added the IC emission as a powerlaw with a photon spectral index of 2.5 and then fitted this model to obtain an upper limit on its normalization and flux. In particular, it is equal to $1.4553\ 10^{-14}\ (+0.1476, -0.2839)\ (c.l.99.7\%)\ erg/s/Hz/cm^2$ which then becomes $1.31\ 10^{41}\ erg/s$ when we take into account a luminosity distance of 290 Mpc (M. Balboni and al.; in preparation). So, we have to integrate the IC emissivity for that same range: to do that we can use Eq. (3.5):

$$L_{IC} = \frac{1}{\pi}\frac{r_0^2}{\hbar^3\ c^2}K_e(k_b\ T)^{\frac{\delta+5}{2}}F(\delta)\frac{2}{3-\delta}(\epsilon_f^{\frac{3-\delta}{2}} - \epsilon_i^{\frac{3-\delta}{2}}) \tag{3.5}$$

where ϵ_f is the equivalent in erg of 2.4 keV and where ϵ_i is the equivalent in erg of 0.1 keV, the end and the start of the energy range of interest.
For the synchrotron emissivity we have instead that:

$$\frac{dE}{dt\ d\epsilon_1} = \frac{\sqrt{3\pi}}{2}\frac{e^3K_e}{mc^2(\delta+1)}(\frac{2\pi mc}{3e})^{-\frac{\delta-1}{2}}B^{\frac{\delta+1}{2}}(\frac{\Gamma(\frac{\delta}{4}+\frac{19}{12})\Gamma(\frac{\delta}{4}-\frac{1}{12})\Gamma(\frac{\delta}{4}+\frac{5}{4})}{\Gamma(\frac{\delta}{4}+\frac{7}{4})})\nu_1^{-\frac{\delta-1}{2}} \tag{3.6}$$

where $\nu_1 = \epsilon_1/h$ and Γ is the Gamma function (G. R. Blumenthal and R. J. Gould 1970). We do not have to do the same operation we did for the IC luminosity for the

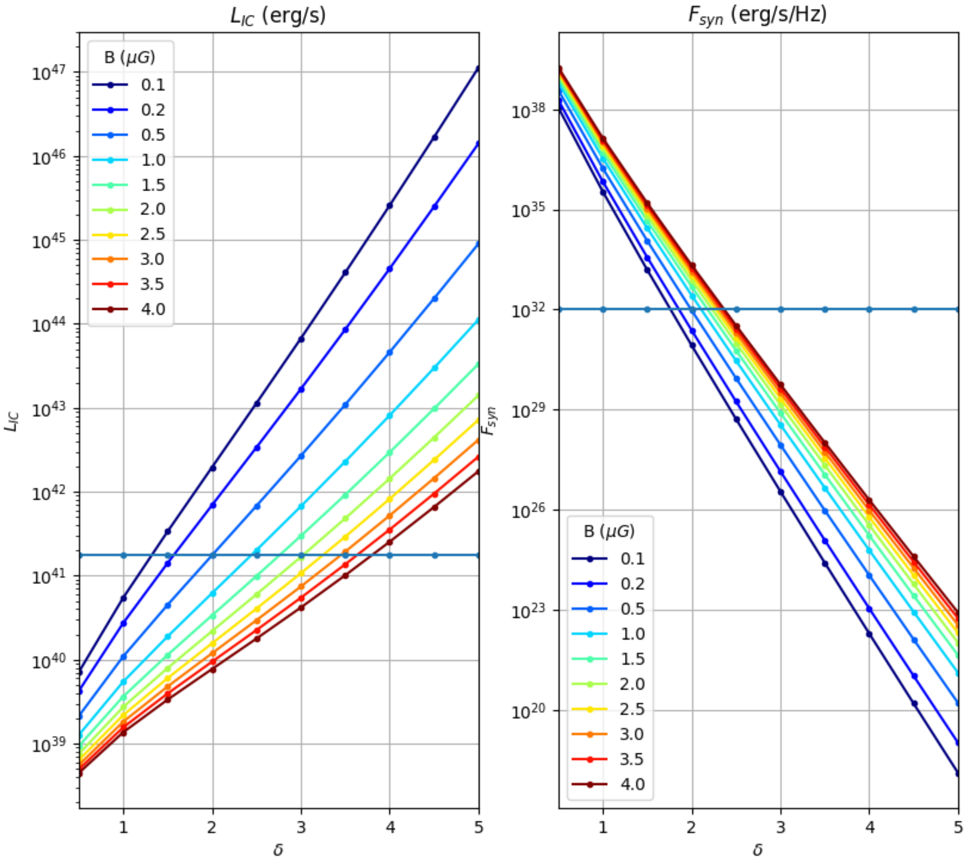

Figure 3.5: IC luminosity (left) and synchrotron flux (right) as a function of δ and $B_{\mu G}$, in the energy band $0.1 - 2.4$ keV. For L_{IC} each δ value has an associated K_e, while for F_{syn} we have assumed $K_e = 10^{64}$. The orizontal lines represent the observational limits for L_{IC} in the corresponding band and the observed F_{syn};

synchrotron emissivity since we only need to use the latter to estimate the entity of the constant K_e, which can be simply obtained by dividing the observed synchrotron flux at 0.14 GHz by Eq. (3.6).

Although the energy band $0.1 - 2.4$ keV is the one studied in this work I think it is useful to report here a brief comparison between the IC luminosity and the synchrotron flux obtained in this band and the band $20 - 80$ keV, that was the first band considered for this work, with an associated IC limit of $2\ 10^{-13}$ $erg/s/Hz/cm^2$, before I switched to the $0.1 - 2.4$ keV for having a more recent and accurate IC limit. For an easier identification of the two limits that I have considered I collect them in Tab. (3.1).

Before proceeding on what is the main focus of this section I report in Fig. (3.4)-(3.5) how Eqs. (3.5)-(3.6) vary as a function of δ and B, with a particular interest in how a difference in the spectral index influences the generated fluxes.

In particular, Eqs. (3.5)-(3.6) depend on K_e, which in turn is related to the amount

Table 3.1: IC observational limits used in my Thesis; the left column represents the energy band and the right column the corresponding limit

Energy band	IC limit	
$20 - 80\ keV$	$2\ 10^{-13}$	$erg/s/Hz/cm^2$
$0.1 - 2.4\ keV$	$1.4553\ 10^{-14}$	$erg/s/Hz/cm^2$

of the population of CRe inside of the volume of the bridge; we can obtain an estimate for K_e for each couple (δ, B) by measuring the observed synchrotron emission and dividing it for Eq. (3.6). However, if we want to observe how the variation of δ and B influence the synchrotron flux then we cannot use this K_e in Eq. (3.6), otherwise we would obviously obtain the observed flux; this is the reason why in Fig. (3.4)-(3.5) we have assumed $K_e = 10^{64}$ for each δ in the F_{syn} graph.

We can now proceed in our analysis; in particular we can observe in Fig. (3.4)-(3.5) how a steeper spectra causes a decrement in the synchrotron flux while it weakly increments the IC luminosity, in fact it is the magnetic field that is the main cause of increment for the IC luminosity, while B weakly influences the synchrotron flux. Therefore the magnitude of the magnetic field inside the region of the bridge is a key factor in establishing the validity of our models. The main difference between Fig. (3.4) and Fig. (3.5) is that in the band $0.1 - 2.4\ keV$ the IC luminosity is much steeper and that for a given B in this band the luminosity always increases with δ, while in the band $20 - 80\ keV$ we have that as the magnetic field increases the steepness of the synchrotron flux decreases and that for $B \geq 2.0\ \mu G$ the IC luminosity even decreases as δ increases. It is therefore much simpler for us to work in the band $0.1-2.4\ keV$ because a slight increment of δ, almost independently from the magnetic field, would increase the IC luminosity and viceversa; considering this band going forward, together with the fact that the IC limit is more accurate than in the band $20 - 80\ keV$, would be our best course of action.

In this particular regard, in Fig. (3.5) we can observe how in our range of B possibly all values of δ could reproduce a luminosity that falls under the observational IC limit; however, higher magnetic field strengths allow for a wider range of viable δ and, viceversa, a higher δ allows for a narrower range of viable magnetic field strengths. For our future analysis with this simple model (so with a $\delta = 3.5$) we have that magnetic fields larger than $3.0\ \mu G$ produce an IC luminosity that does not defy the observational constraint; this is also a much more stringent magnetic field limit rather than the $0.5\ \mu G$ in the band $20 - 80\ keV$, that from now on I will no longer consider. This is already a result that may show how a shock model for acceleration is unlikely to describe the emission of the bridge, however a more complex distribution of magnetic fields may still save this model.

3.2.1 Inverse Compton from different distributions of magnetic fields

Now that I have given a rough estimate of how the synchrotron and IC fluxes vary with δ, I can consider precisely how different spatial distributions of B may influence

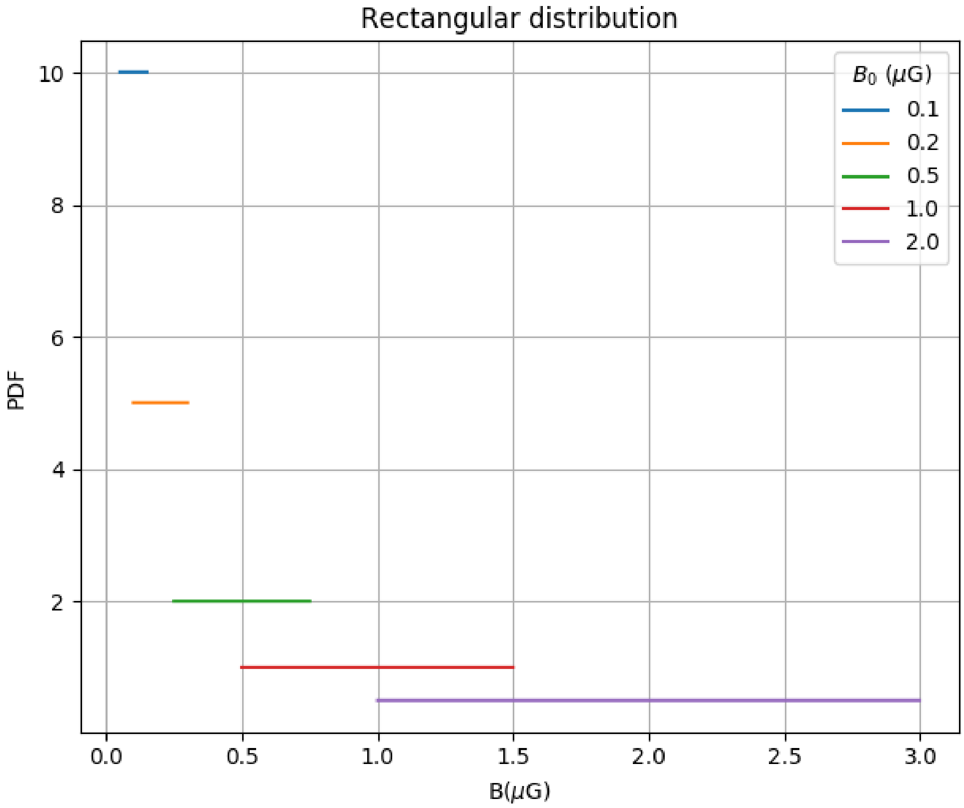

Figure 3.6: Probability distribution function (PDF) for different box functions, which vary accordingly to the length of the range on the magnetic fields, and different B_0;

the aforementioned observables. We will also see how a different filling factor may shift the critical B (B_{crit}), for which the IC luminosity matches the observational limit.

Such an analysis is necessary, considering the very little information available on the magnetisation of intra-cluster bridges, both from observations (lacking of Faraday Rotation measurements, for example) and from direct numerical simulations (which struggles to properly resolve the process of dynamo amplification of magnetic fields in this rarefied environment, and hence only give a lower limit on the plausible magnetisation of the A399-401 bridge).

I mark with B_0 what is the mean value of B over the bridge, and so I will show what are the two distributions for the magnetic field that I have considered, apart from the uniform one: the simplest one is the rectangle distribution, as seen in Eq. (3.7):

$$\Pi(B) = \begin{cases} \frac{1}{B_{max}-B_{min}} & if \quad |B - B_0| > \frac{B_0}{n} \\ 0 & if \quad |B - B_0| > \frac{B_0}{n} \end{cases} \tag{3.7}$$

where n is a parameter which defines the extension of the available values of B; I also show in Fig. (3.6) some of the different instances of this distribution that I have

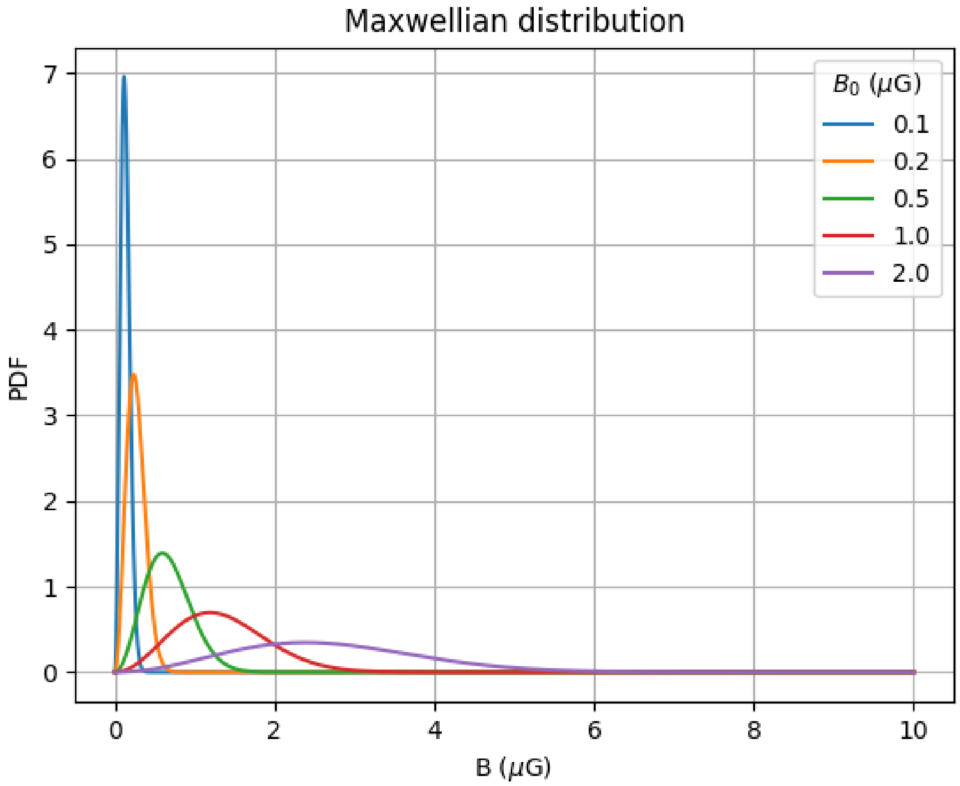

Figure 3.7: PDF for different maxwellian distributions which vary accordingly to the wideness of the main "bell" of the PDF and to B_0;

used.

It is important to say that this first distribution is not considered as a very realistic one yet it gives us a first idea into how a distribution of magnetic fields may change the IC luminosity compered to a uniform distribution, as we will see later on.

The second magnetic field model is a maxwellian distribution, with its Probability Distribution Function (PDF) written in Eq. (3.8):

$$f_{Max}(B) = \sqrt{\frac{2}{\pi}}\,\frac{B^2}{\sigma^3}\ \exp -\{\frac{B^2}{2\sigma^2}\} \tag{3.8}$$

where $\sigma = \sqrt{\frac{3\pi-8}{2}}\,B_0$ defines the standard deviation of the distribution, with its value given by M. Murgia and al. (2019); its behaviour is shown in Fig. (3.7) where each distribution varies in the dispersion of the central value. I also report the expression for the Cumulative Distribution Function (CDF) of the maxwellian distribution, in Eq. (3.9), since it will be used to calculate the synchrotron flux later on, and that is

$$cdf_{Max}(B) = erf(\frac{B}{\sqrt{2}\sigma}) - \sqrt{\frac{2}{\pi}}\,\frac{B\exp\{-B^2/2\sigma^2\}}{\sigma} \tag{3.9}$$

where erf is the error function.

The maxwellian distribution can be expected to better represent the distribution

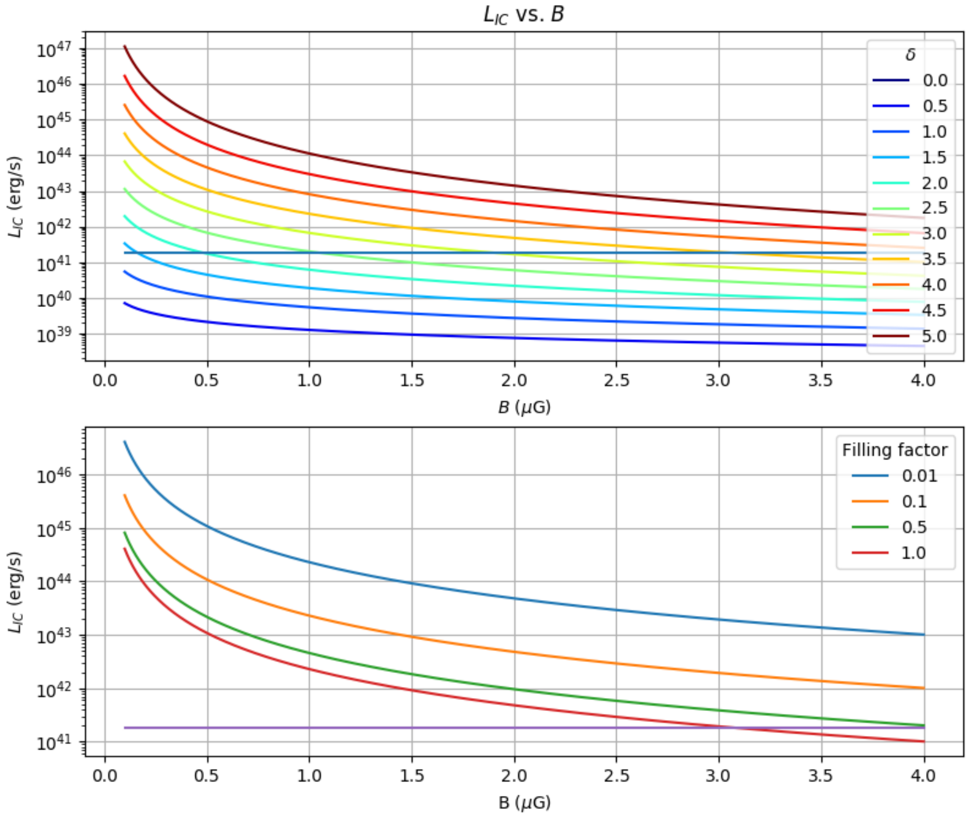

Figure 3.8: IC luminosity obtained from a uniform distribution of B under a variation on δ; the lower graph assumes a $\delta = 3.5$; the horizontal line represents the observational constraint.

of magnetic fields in the region and it can be inferred through the Faraday RM, whether it is internal or foreground, since it can provide insight on the distribution of magnetic fields in a radio source. If the RM is internal then the gas is mixed with the radio emitting region whilst if it is foreground then it is due to the material surrounding the region of interest. Therefore measuring the RM can help to constrain the magnetic field strength and distribution P. C. Tribble (1991). In particular, following the works of P. C. Tribble (1991) and M. Murgia and al. (2019), it can be shown via numerical simulations that each component of the magnetic field is Gaussian distributed, meaning that the distribution of B itself is maxwellian (M. Murgia and al. 2019).

As in the case of the box distribution, the maxwellian one will be compared to a uniform distribution of B over the whole volume of the bridge, however I will also treat the results from this comparison as physically more realistic, since I expect the maxwellian to reflect the real distribution of magnetic fields over the bridge, resulting from the turbulent dynamo amplification of magnetic fields and as above mentioned (G. Brunetti and F. Vazza 2020).

Before comparing the luminosities obtained for the different distributions for a fixed

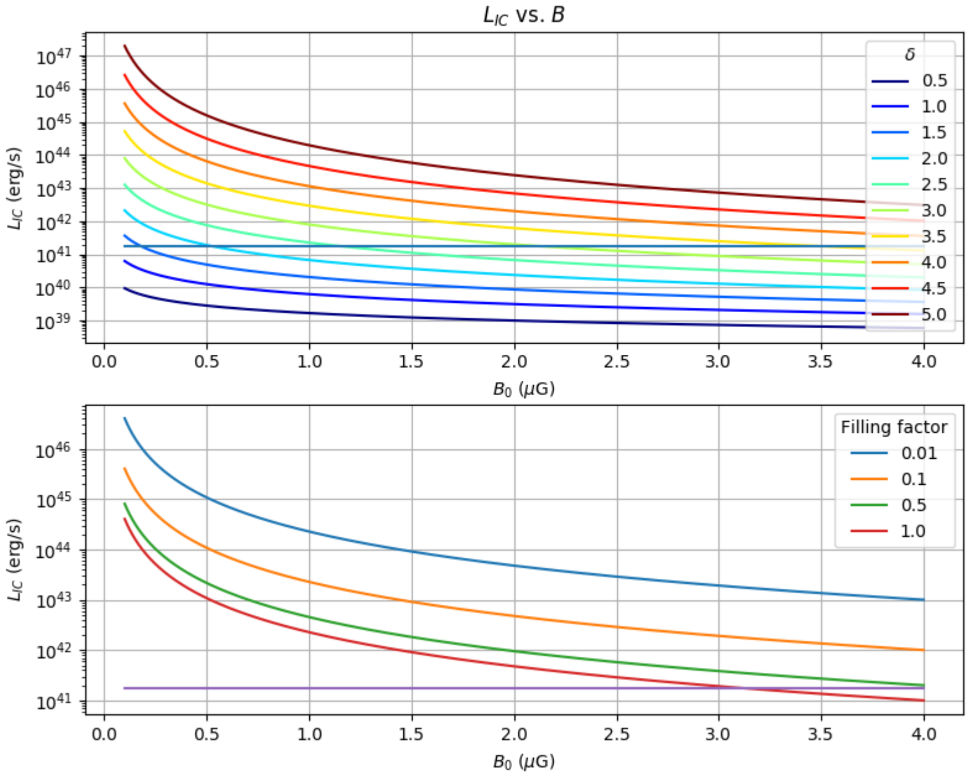

Figure 3.9: IC luminosity obtained from a rectangle distribution of B under a variation on δ; the lower graph assumes a $\delta = 3.5$; the horizontal line represents the observational constraint.

particle spectrum, it is useful to see how a variation in δ may affect our system for each distribution that I report: uniform, box, maxwellian. It is important to know that the upper and lower graphs in Fig. (3.8) through (3.10) have been obtained by comparing Eq. (3.6) with the observed synchrotron flux to obtain the constant K_e to insert into Eq. (3.5), which gives us the IC luminosity.

In the simpler case of a uniform distribution, as we can see in Fig. (3.8), an increasing δ causes a steeper profile of IC while B increases, in particular this implies that the critical value of B is shifted to the right as δ increases. However, even if the change in IC luminosity between two close δ is not large, if we are looking for a first estimate of B_{crit}, choosing between two adjacent δ, where their values are written in the caption of Fig. (3.8), may change the magnitude of B_{crit} of ≈ 1 μG, since as the strength of B_0 increases the flatness of the profile does too. In particular, for a $\delta = 3.5$ then $B_{crit} \approx 3.12$ μG, in accordance with what we obtained from Fig. (3.5). A different filling factor may significantly change B_{crit} because it can increase the IC luminosity up to two orders of magnitude (since the smaller filling factor used is 0.01); this means that the maximum B_{crit} that I have obtained are actually much greater than 3.12 μG, those being respectively 8.65 μG and 24.08 μG for filling factors 0.10 and 0.01, even though that is hard to explain by the sole physics of

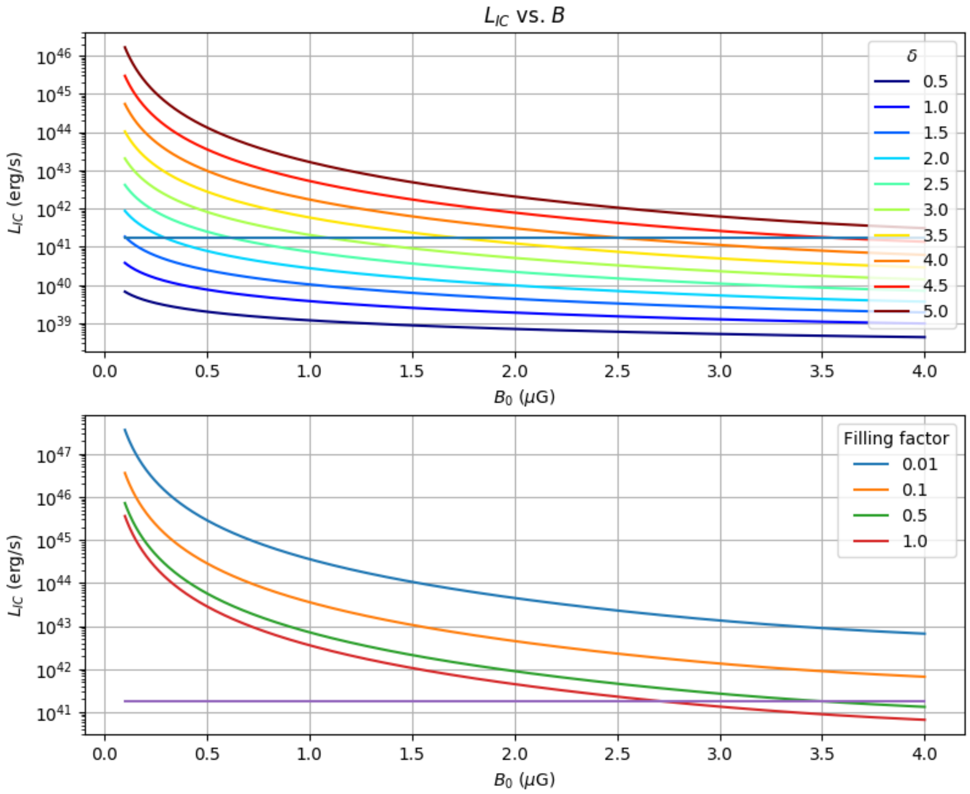

Figure 3.10: IC luminosity obtained from a maxwellian distribution of B under a variation on δ; the lower graph assumes a $\delta = 3.5$; the horizontal line represents the observational constraint.

magnetic field amplification.

A similar behaviour can be seen in Fig. (3.9) where I consider a box distribution of magnetic fields, however the obtained IC luminosities are in general slightly fainter than the ones obtained for a uniform distribution. For a given δ, B_{crit} is of the same order of magnitude, even if it is slightly lower than the one obtained through the previous distribution. The box distribution decreases the expected IC luminosity produced by the bridge but it follows the same steepness of the IC luminosity profile for a uniform distribution of magnetic fields.

On the other hand the maxwellian distribution in Fig. (3.10) produces spectra that are roughly one order of magnitude less than the ones from the uniform distribution and $B_{crit} \approx 2.09\ \mu G$. At the same time the IC luminosities produced vary less with δ, for the maxwellian distribution produces luminosities that are steeper for lower B_0 and flatter for higher B_0 as compared to the ones from the other distributions.

3.2.2 IC limits for a fixed spectrum

In the following, I will stick to a $\delta = 3.5$ spectrum, which means having a Mach number $M = \sqrt{11/7}$. In particular, we expect to obtain $B_{crit} \approx 3.12,\ 2.97,\ 2.09\ \mu G$

respectively for a uniform, box and maxwellian distribution of magnetic fields, as we gleaned from Fig. (3.8) to (3.10). However, I will explore different instances of our distributions of magnetic fields and I will extend the range on B_0 to infer what the entity of B_{crit} may be for lower filling factors.
I begin by showing how the three distributions (uniform, rectangle and maxwellian) behave when compared to one another. As we see in Fig. (3.11), the uniform distribution produces the higher IC luminosity for a fixed B_0, while the maxwellian produces the lower one, also the rectangle distribution, which has a range on B in the bridge of $B_0 - B_0/2 < B_0 < B_0 + B_0/2$, is much closer to the uniform one, while the luminosity obtained with the maxwellian, which is independent on the range of B, is systematically lower than the other two. This overall gives us the idea of the uncertainty associated with the spatial distribution of B, which is presently not constrained by observations. Also the difference in magnitude between the three analysed distribution remains roughly the same.
I can now analyse how the individual distributions behave, and we start with the rectangle one of Eq. (3.7), compared to the uniform distribution. We can immedi-

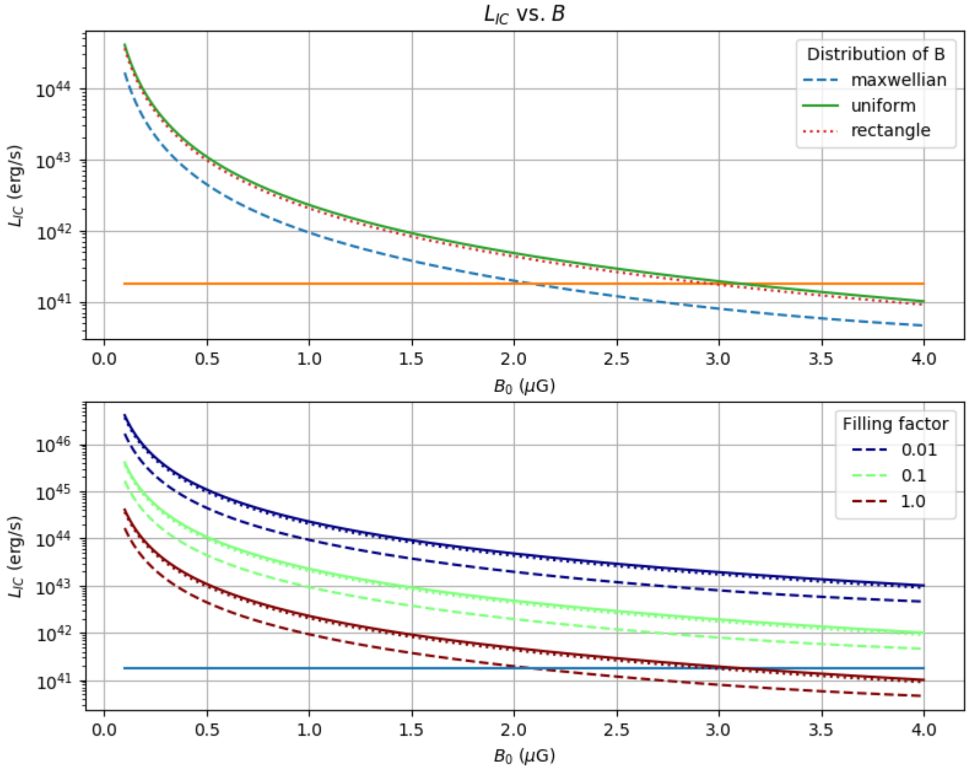

Figure 3.11: In the upper graph we assumed a filling factor of 1.0 and the IC luminosity changes with the type of distribution; In the lower graph (we assumed a range of $B_0 - B_0/2 < B_0 < B_0 + B_0/2$ for the rectangle distribution) the IC luminosity changes with the filling factor; the horizontal lines represent the observational constraint.

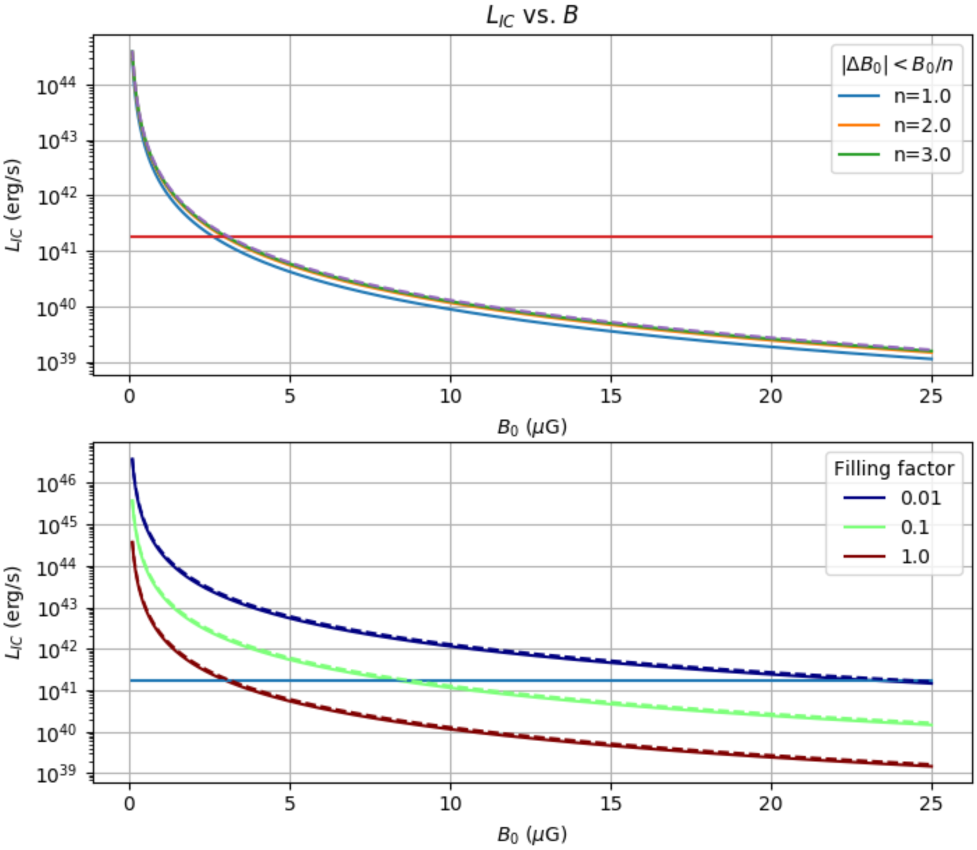

Figure 3.12: In the upper graph we assumed a filling factor of 1.0 and the IC luminosity changes with the range on B, solid lines represent a rectangle distribution while the dashed line represents the uniform distribution; In the lower graph we assumed a value $n = 2.0$ and the IC luminosity changes with the filling factor; the horizontal line represents the observational constraint.

ately see that in the upper graph of Fig. (3.12) the rectangle distribution always produces a fainter IC luminosity than that of the uniform distribution, and also that the narrower the range on B the closer the two fluxes are, as we could expect. The range on B changes the IC luminosity because the rectangle distribution is the simplest approximation for a distribution of magnetic field that is not uniform, it is not realistic.

I obtain the IC luminosity profile by assuming a range of B outside of which there is no emission, then I divide the volume of the bridge in a large enough number of 1000 sub-volumes where each of them has a different value of B assigned, let us call it B_{sub}, with the magnetic field strength varying in the range of allowed B. I then consider the each sub-volume of the bridge to emit IC as with a uniform distribution of magnetic field with a magnetic field strength equal to the B_{sub} corresponding to the sub-volumes. Finally I sum all the contributions of IC luminosity from each sub-volume to obtain the IC luminosity from the whole bridge. For a fixed number

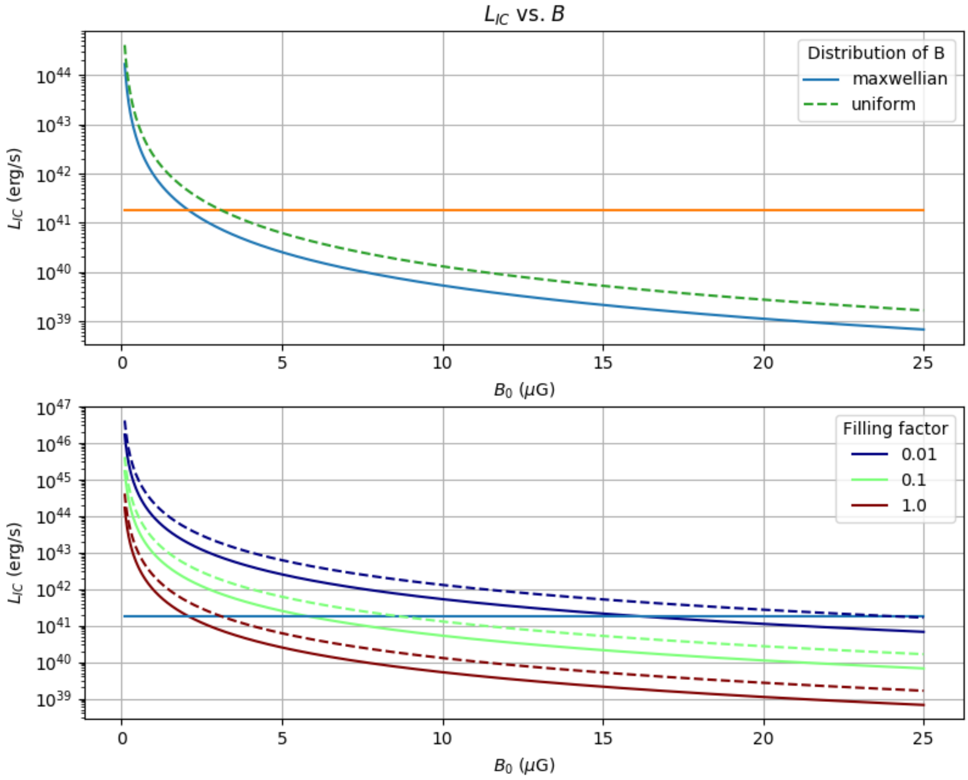

Figure 3.13: In the upper graph I assumed a filling factor of 1.0 and the IC luminosity changes with B_0, solid lines represent a maxwellian distribution while the dashed line represents the uniform distribution; In the lower graph the IC luminosity changes with the filling factor; the horizontal line represents the observational constraint.

of sub-volumes, the narrower the range on B the smaller the difference between each B_{sub}, thus approaching a uniform distribution of magnetic fields, and viceversa.
Since the highest IC luminosity is from the uniform distribution, I can say that the upper limit for B_{crit} is approximately 3.12 μG, to which the box distribution approaches for as the range on B gets narrower, at least if the radiation is produced by the whole volume (filling factor = 1.0). For a range $0 < B < 2B_0$ then $B_{crit} \approx 2.61$ μG, for $B_0/2 < B < 3/2B_0$ then $B_{crit} \approx 2.97$ μG and for $2/3B_0 < B < 4/3B_0$ we have that $B_{crit} \approx 3.04$ μG.
If we move to the lower graph of Fig. (3.12) we see that for a range of $|\Delta B| < B_0/2$, as the filling factor the IC luminosity increases, for a fixed value of B_0, the IC luminosity increases, so instead in this case 3.12 μG is the minimum value of B_{crit} that we obtain; for a filling factor of 0.1 we have that $B_{crit} \approx 8.25$ μG and while we have a filling factor of 0.01 we have that $B_{crit} \approx 22.93$ μG, which is too high of a value to be plausible, as we will see in a later section.
We have seen now what are the generic changes that a variation in range of B and in filling factor might produce, however the rectangle distribution is not a very plausible model for the distribution of B so to further improve our analysis I will switch

to the maxwellian distribution of Eq. (3.8), for which the results can be observed in Fig. (3.13).
I obtain the IC luminosity profile for this distribution by letting the magnetic field strength B vary through a sufficiently large range, that may cover the whole PDF of the maxwellian, centered around B_0. Using Python, I integrated the synchrotron flux, F_{syn} in Eq. (3.6), by summing the F_{syn} obtained from each B weighted by the maxwellian PDF in Eq. (3.8) and the step of the integral on B, after that I divided the sum by the CDF of the maxwellian in Eq. (3.9). Having now the total F_{syn}, I can obtain the constant K_e to insert inside Eq. (3.5) to obtain the IC luminosity. The Python program used to this end is reported in Appendix A.
In the upper graph we find that $B_{crit} \approx 2.09\ \mu G$ for a filling factor of 1.0, so it is less than the B_{crit} for the rectangle distribution, also the luminosity that we obtain does not depend on the range of B, but only on the dispersion of the distribution, which varies only with B_0. Moving on to the lower graph we see that the IC luminosity increases with the filling factor and so does B_{crit}, in particular $B_{crit} \approx 5.81\ \mu G$ for a filling factor of 0.10 and $B_{crit} \approx 16.18\ \mu G$ for a filling factor of 0.01. As previously stated, it is likely that the filling factor is between 0.01 and 0.1 so, since the only available range of B_0 inside the bridge would need to be greater than 5.81 μG in order to produce an IC luminosity lower than the constraint, this current model is highly unlikely. A filling factor of 1.0 or 0.1, between the ones that I have considered is more likely since it allows a wider range of viable B_0.

3.2.3 Results on critical magnetic field strengths

Now that I have established how different magnetic field distributions may influence the production of synchrotron emission, and in turn IC emission from the same population of electrons, I can summarise the main results. The strength of the critical magnetic fields is of particular interest, since it is the main quantity that we can use to determine the likelihood of our shock acceleration model, where a power-law type particle distribution has been assumed. We will see how B_{crit}, so the critical value of B above which the IC luminosity falls under the observational limit, changes with the filling factor, which is the other free parameter in my analysis.

Table 3.2: Critical magnetic field strength (in μG) as a function of filling factor and magnetic field distribution for a spectral index $\delta = 1.3$; on the top row are different filling factor values (fill.) and on the left column are the magnetic field distributions (distr.);

distr./fill.	0.01	0.10	1.00
uniform	24.08	8.65	3.12
rectangle	22.93	8.25	2.97
maxwellian	16.18	5.81	2.09

In Table (3.2), I summarise the various B_{crit} that I have obtained for the three distributions considered in the previous Section. It can be seen how the the critical magnetic field for the uniform and the rectangle distribution have a maximum difference between their B_{crit} of roughly 1 μG for a filling factor of 0.01 while of roughly 0.1 μG for the maximum filling factor of 1.00; this means that for smaller filling factors the difference between this two distributions increases, even if only slightly. As said already, the maxwellian distribution is probably the most realistic and, in particular, we can immediately see the significant difference between the other two distributions. Perhaps due to the more realistic nature of the maxwellian, B_{crit} is significantly lower than the ones obtained through the other, simpler, distributions, even 8 μG lower. Nevertheless, in all of the cases the B_{crit} implied even by the maxwellian model are extremely large, and well above any realistic estimate of a plausible magnetic field in the bridge volume as long as the filling factor is assumed to be smaller than 1.00. This overall makes the shock acceleration model physically unlikely, despite potentially able to explain the synchrotron emission detected by LOFAR.

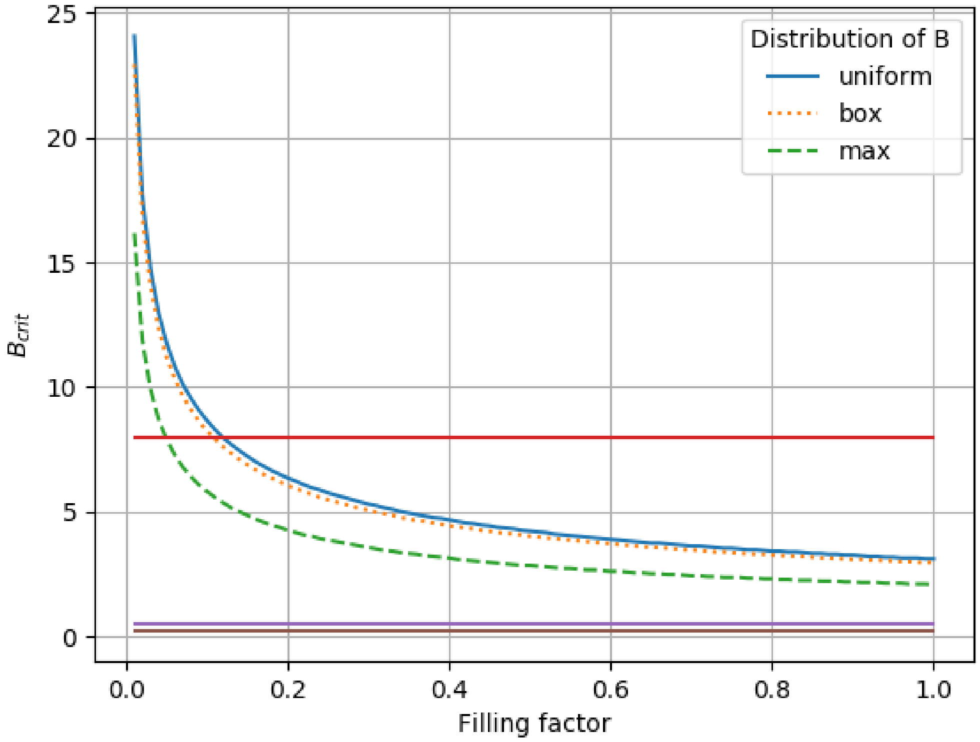

Figure 3.14: Critical magnetic field strength as a function of filling factor for a uniform, a rectangle and a maxwellian distribution of magnetic fields, with $\alpha = 1.3$; respectively, the lower, the middle and the higher horizontal lines are the 0.2 μG magnetic field limit from G. Brunetti and F. Vazza (2020), the 0.5 μG limit from F. Govoni and al. (2019) and the 8 μG limit from the equivalence between the thermal and magnetic pressure;

To gain a clearer picture on the issue of the likelihood of this acceleration model I have extended the previous reasoning to all filling factors between 0.01 and 1.00 in

Fig. (3.14), where the three horizontal lines are the three magnetic field limits that I have presented in Chapter (2); to recap those limits, the lower ones are due to the simulations performed by F. Govoni and al. (2019) and G. Brunetti and F. Vazza (2020). The higher limit on the magnetic field can be computed as the equipartition (magnetic energy/thermal energy ~ 1) value of the magnetic field strength, in particular if we take the limit of 0.5 μG which corresponds to a $\beta_{pl} \approx 100 - 200$, from the work of G. Brunetti and F. Vazza (2020), then $B \approx 0.5\sqrt{\beta_{pl}} \approx 8\ \mu G$ is roughly the limit on B due to the equivalence between thermal and magnetic field pressure. In Fig. (3.14), we see that B_{crit} is a monotonous decreasing function of the filling factor, as we would expect, since a lower filling factor means an increase in IC luminosity and therefore a shift to the right of the critical magnetic field for which the IC luminosity meets the observational limit.

Each one of the distributions has a minimum B_{crit}, that can be found for a filling factor of 1.00, much higher than the two limits expected from the simulations of G. Brunetti and F. Vazza (2020) and F. Govoni and al. (2019). This is already a very important result since it shows well that the Fermi I shock re-acceleration model cannot reproduce IC luminosities that fall under the observational constraint, while at the same time using a magnetic field and a filling factor compatible with the results by dynamical, MHD simulations.

The highest limit on B comes from the equivalence on the thermal and magnetic field pressure and, considering that limit, we have that $B_{crit} < 8\ \mu G$ if the filling factors are higher than 0.12, 0.11, 0.05 respectively for the uniform, the rectangle and the maxwellian distribution. In particular, for the B_{crit} obtained from the maxwellian distribution, we have a filling factor of 0.05 that is the only one still under the 0.1 expectation on filling factors from MHD simulations in G. Brunetti and F. Vazza (2020).

The spectral index of 1.3 is a first assumption made by F. Govoni and al. (2019), however in the work of C. D. Nunhokee and al. (2022) what seems to be a more accurate prediction is made, albeit limited to a smaller fraction of the bridge emission visible with LOFAR. In particular, the spectral index of A399 should be around 1.75, whilst for the bridge a lower limit of $\alpha > 1.5$ has been established (C. D. Nunhokee and al. 2022). In Fig. (3.15) we may see how B_{crit} changes for $\alpha = 1.3$, 1.5 and 1.75, and as we could expect it grows monotonously with α, since a steeper spectral radio slope means an higher IC luminosity, and therefore a shift of B_{crit} to greater magnetic field strengths.

We can infer that for this lower limit on α the shock acceleration model becomes already even more unlikely than before, unlikelihood that would only increase if the spectral index were higher, given that an increase in α always means an increment in IC luminosity for the energy band $0.1 - 2.4\ keV$, as stated in Section (3.2). It shall also be remarked that an even steeper radio spectral slope implies an even steeper distribution of radio emitting electrons from the bridge area, making it even harder for the shock re-acceleration scenario to explain the radio emission from A399-A401, given the typical population of shocks formed by the numerical simulation of this system.

To give a more quantitative result, I will try and compare the values of B_{crit} that can be obtained for the maxwellian distribution of magnetic fields, the most realis-

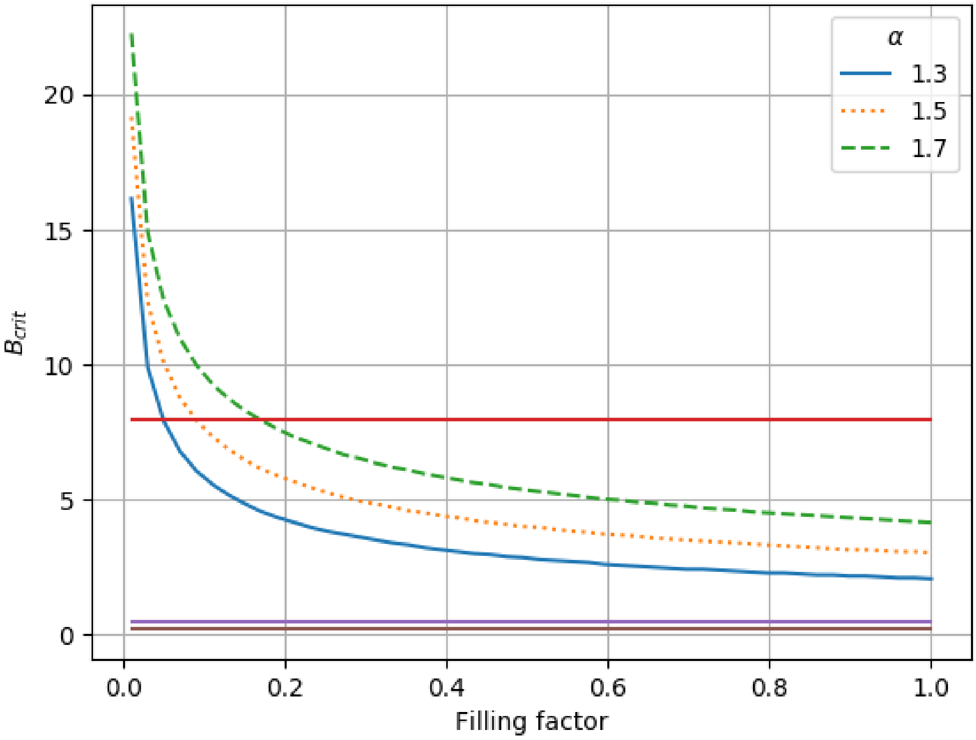

Figure 3.15: Critical magnetic field strength as a function of filling factor for a maxwellian distribution of magnetic fields, and changing with α; respectively, the lower, the middle and the higher horizontal lines are the 0.2 μG magnetic field limit from G. Brunetti and F. Vazza (2020), the 0.5 μG limit from F. Govoni and al. (2019) and the 8 μG limit from the equivalence between the thermal and magnetic pressure;

tic distribution amongst the ones that I have considered in this work, as stated in Section (3.2.1), and as they vary with $\alpha = 1.3,\ 1.5,\ 1.75$. In Tab. (3.3), I report the values of B_{crit} obtained for these different values of α and for the filling factors used in this work.
The increment of B_{crit} is more significant for the lower filling factors, up to roughly 6 μG for a filling factor of 0.01, so the major differences that a change in α causes manifest themselves for the lower filling factors. The higher ones vary less, however since we expect the filling factor of the bridge to be less than 0.1, from the work of G. Brunetti and F. Vazza (2020), we can focus our attention in this range of filling factors < 0.1 when considering how B_{crit} may varies with α. This holds, especially if in the future more stringent constrains on α were to be measured.
In particular, we find that for all of the cases studied in this Section, the upper limits on the magnetic field in the bridge that have been found from F. Govoni and al. (2019) and G. Brunetti and F. Vazza (2020) have been far exceeded by B_{crit} which, to recall, is the minimum strength of magnetic fields in the bridge that can lead to the production of an IC luminosity lower than the observational constraint.

Table 3.3: Critical magnetic field strength (in μG) as a function of filling factor and different α values, for maxwellian magnetic field distributions; on the top row are different filling factor values (fill.) and on the left column are the values of *alpha*;

α/fill.	0.01	0.10	1.00
1.3	16.18	5.81	2.09
1.5	19.17	7.64	3.03
1.75	22.27	9.62	4.16

Therefore, a shock re-acceleration model is unlikely. The only limit on magnetic field strength that may allow this model to describe the emission from the bridge is the 8 μG limit. The values of filling factors for which $B_{crit} = 8\ \mu G$ are $0.05,\ 0.09$ and 0.17, respectively for $\alpha = 1.3,\ 1.5,\ 1.75$.

A spectral index of 1.75 would therefore need a filling factor too high to explain the undetection of the IC emission in the bridge and, at the same time, to keep to the magnetic field in the region from becoming too high itself. The lower limit on α of 1.5, with a filling factor of 0.09 could still barely remain under the 0.1 filling factor upper limit predicted by G. Brunetti and F. Vazza (2020), while an $\alpha = 1.3$ produces more likely results, but its value is a first estimate made by F. Govoni and al. (2019), and a more stringent value for α can be found in C. D. Nunhokee and al. (2022). However, this results are for an upper limit on magnetic field strengths of 8 μG, which is much higher than the 0.2 μG and 0.5 μG limits found by F. Govoni and al. (2019) and G. Brunetti and F. Vazza (2020), which have been far exceeded from all of the models that I have presented.

Comparison between IC from a Fermi I and a Fermi II model

Since the previous analysis have convincingly shown that attempts to explain with a shock model the radio emission from A399-A401 are hardly compatible with the IC limits, in a last step of my Thesis, I will briefly discuss how different models compare with the same IC limits. In particular, I compare a subset of the possible Fermi II turbulent re-acceleration models, in particular the ones used in Fig. 3 of G. Brunetti and F. Vazza (2020), with the IC luminosity produced by a shock re-acceleration model, with the purpose of explaining the observed radio emission in the bridge. I have superposed to the IC luminosities obtained in that work one of the IC luminosity obtained in my Thesis work, and the resulting spectra can be seen in Fig. (3.16).

Firstly, let us consider the models from G. Brunetti and F. Vazza (2020), these are Fermi II turbulent re-acceleration models for populations of fossil CR electrons and CR protons, with $\eta_B = 0.02$ for the red lines, $\eta_B = 0.03$ for the blue line and $\eta_B = 0.05$ for the green lines. The dashed lines represent models that take into account only a primary electron spectrum. It can be inferred that the predictions of the models vary little with the initial population, that might be because of the turbulent re-acceleration mechanisms, which imply that after an isotropization time the system loses memory of the initial conditions.

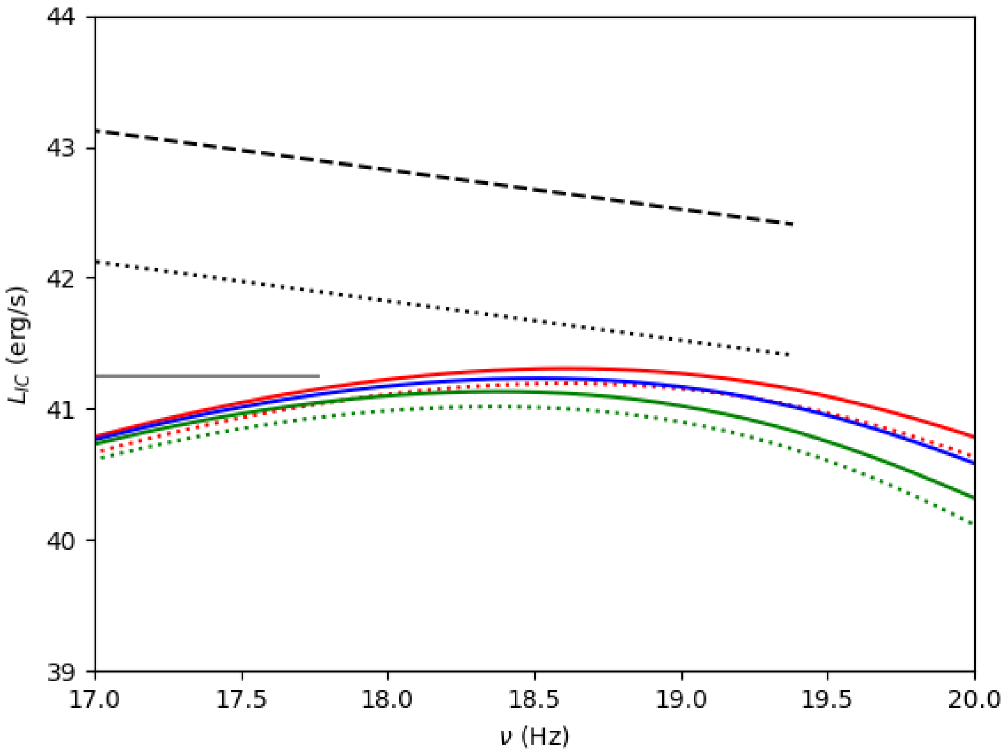

Figure 3.16: IC luminosity by a CRe and CRp population as a function of frequency; the red, blue and green lines represent the models used in G. Brunetti and F. Vazza (2020), respectively for $\eta_B = 0.02$, $\eta_B = 0.03$ and $\eta_B = 0.05$, also the dashed coloured lines represent spectra produced only by primary electrons; The horizontal and obliques black lines represent the IC observational limit and the IC luminosity from a Fermi I re-acceleration model with a maxwellian distribution of magnetic fields, the lower one has a filling factor of 1.0 and the higher one has a filling factor of 0.1;

In Fig. (3.16), the horizontal solid grey line represents the IC observational constraint in the energy range $0.1 - 2.4\ keV$, while the black lines represent a Fermi I model from a maxwellian distribution of magnetic fields with $\alpha = 1.3$, $B = 0.5\ \mu G$ and filling factors of 1.0 (pointed black line) and 0.1 (dashed black line), that go up to 100 keV to better show how the models behave and compare them to the turbulent ones, also at higher energies. I chose a magnetic field strength of $0.5\ \mu G$ to be consistent with the predictions used in G. Brunetti and F. Vazza (2020).
Fermi I models produce a powerlaw type spectrum which implies a higher emission for lower energies, since the majority of the population of particles is at those energies. Instead, Fermi II models manifest a bump around the $10^{18.5}$ Hz mark, thus producing less emission for energies that are lower or higher than the peak one. Because of this, the predictions for Fermi II models are more realistic and less constrained by the IC; investigating the IC emission in the energy band of the peak may provide a better insight on the likelihood of Fermi II models to describe the

bridge.

Returning to Fig. (3.16), we have that for a filling factor of 1.0 we should expect the IC by Fermi I to be almost equal to the peak emission of the IC by turbulent re-acceleration, however it is slightly higher. This is because, although the mean magnetic field is 0.5 μG, its distribution amongst the volume of the bridge is not uniform and a variety of magnetic fields populates the volume, therefore a decrease in IC emission should occur, considering also that the magnetic field determines the acceleration efficiency, as seen in Eq. (1.90) given by the model in G. Brunetti and F. Vazza (2020), and so also the radio and IC spectrum.

The main comparison between the powerlaw Fermi I models and the turbulent Fermi II models is that, with the used combination of parameters, the shock models are way higher than the observational limits, as previously stated, while the turbulent models are below it.

This means that, while using magnetic field strengths and a filling factor that are under the predicted simulated limits by G. Brunetti and F. Vazza (2020), a Fermi I model is unlikely to describe the emission of the bridge but turbulent re-acceleration models may still be able to describe it and to justify the undetection of IC radiation in the region of the bridge. However, this exercise also shows that deeper limits from IC in the hard-X band ($> 5-10$ keV) or from much deeper XMM integrations in the soft-band will also have the potential of representing a tough stress test for the turbulent re-acceleration model, considering that all of the investigated model variations are consistently producing estimates which are just below the currently available IC constraints.

Chapter 4

Conclusion

In this work, I have investigated the possible origin of the synchrotron emission in the radio bridge A399-A401 at a luminosity distance of roughly 290 Mpc as observed with LOFAR at 140 MHz, for a total flux of 0.822 mJy. The presence of synchrotron radiation in such a large scale structure, as it extends for at least the projected distance of 3 Mpc, also implies the presence of very faint IC radiation, that has remained undetected up until now. From the available limits on the total IC flux from this object, in the X-ray band, it is thus possible to put additional strong constraints on the acceleration model to produce the relativistic electrons responsible for the radio emission detected by LOFAR.

For this Thesis work, my collaborators have derived updated limits on the IC, using either ROSAT or XMM-Newton, within the energy bands $20-80$ keV and $0.1-2.4$ keV, respectively $2\ 10^{-13}$ $erg/s/Hz/cm^2$ and $1.4553\ 10^{-14}$ $erg/s/Hz/cm^2$ [1]. Some of the differences between the first and the second energy band are that the first limit is also the oldest amongst the two of them and that in the $0.1-2.4$ keV range the IC luminosity produced has a monotonous increase with δ.

I have then assumed that the synchrotron emission from the bridge is produced by a Fermi I model that re-accelerates a pre-existing population of CRe to relativistic energies. The only data in our possession were the observed synchrotron flux, based on F. Govoni and al. (2019), and the undetection of IC emission. Therefore, I compared the observed synchrotron flux to the one predicted by the Fermi I shock re-acceleration model [Eq. (3.6)] by dividing them and thus obtaining a value for K_e, the number of radiating particles expected to be located in the region of the bridge. Obviously a variation in filling factor, the portion of the bridge responsible of producing synchrotron emission, will lead to a direct change in K_e, which I then insert into Eq. (3.5) to compute the predicted IC emission. The magnetic field in the bridge region is a key ingredient here, whose variation in amplitude affects the ratio between the IC and the radio emission, assuming both emissions come from the same distribution of relativistic electrons. For magnetic field strengths higher than a critical value, called B_{crit}, the IC luminosity falls under the observational constraint, and from a decrease in filling factor the IC luminosity increases as does

---

[1] I would like to thank Marco Balboni and Fabio Gastadello for producing and sharing their X-ray limits on the non-detection of IC emission that I have used here.

the consequent B_{crit}.
The main results of my Thesis can be summarized as follows:

- The predicted limits on the magnetic field strength of the bridge for a $\delta = 3.5$ are around 0.5 μG and 3.1 μG, respectively for the $20 - 80$ keV and the $0.1 - 2.4$ keV energy bands. All this considered I choose the lower energy band to proceed in my analysis. Therefore, all of my successive Thesis work refers to the energy band $0.1 - 2.4$ keV;

- The next step was to investigate how different distributions of magnetic fields over the volume of the bridge may change the predicted IC luminosity. I have considered distributions of magnetic fields of increasing realism: a uniform, a rectangle [Eq. (3.7)] and a maxwellian [Eq. (3.8)]. The first two distributions served as a preliminary analysis to provide an element of comparison between the simplest assumption of a uniform distribution and the effects of a more complex one, in particular the effect is a decrement on the IC luminosity. The maxwellian distribution is the one which is expected to be more realistic from previous works (P. C. Tribble 1991; M. Murgia and al. 2019) so I used it as the main source of results to verify the likelihood of the hypothesized Fermi I re-acceleration model;

- I was able to infer the B_{crit} values obtained from the maxwellian distribution under different combinations of filling factor and radio spectral index α. From simulations and calculations it was possible to obtain upper limits on the magnetic field strength in the bridge, those being roughly 0.2 μG, from simulations in F. Govoni and al. (2019), 0.5 μG, from simulations in G. Brunetti and F. Vazza (2020), and 8 μG as a computed value coming from the equality between thermal and magnetic pressure. A range of plausible filling factors could be < 0.1, coming from simulations in the work of G. Brunetti and F. Vazza (2020). The expected values on α were taken from the work of F. Govoni and al. (2019), who inferred $\alpha = 1.3$, and from the work of C. D. Nunhokee and al. (2022), who instead inferred a lower limit on the radio spectral index of 1.5, to be compared with the 1.75 value obtained for the A399 cluster;

- I checked under which combination of filling factors and α the Fermi I model that I used was able to produce a B_{crit} that would fall under the above mentioned upper limits, and under no conditions it was able to give a B_{crit} under the limits of F. Govoni and al. (2019) and G. Brunetti and F. Vazza (2020). We obtain very large values of B_{crit} in all cases, and even larger than the 8 μG magnetic field limit corresponding to the equipartition with the thermal gas energy, a scenario which would not be explained by any known dynamical model. If $\alpha = 1.3$ then the filling factor would need to be ≥ 0.05, but if $\alpha = 1.5$, whose value is backed by simulations, then the filling factor would need to be ≥ 0.09, bordering the 0.1 upper limit computed by G. Brunetti and F. Vazza (2020), and thus already making this result unlikely. More than this, the limit of 8 μG comes from a simple analytical computation and not from more complex simulations like the ones in F. Govoni and al. (2019) and G. Brunetti and F. Vazza (2020).

Therefore, a Fermi I re-acceleration through shocks is highly unlikely to describe the origin of the observed emission of the radio bridge A399-A401, making it necessary to consider other models with which to glean its nature.

In particular, a Fermi II turbulent re-acceleration model may instead be able to describe the emission from the bridge and the undetection of the IC radiation, while still respecting the limits predicted by G. Brunetti and F. Vazza (2020) on the magnetic field strength and the filling factor.

Appendix A

Python code to compute Inverse Compton

In this Appendix, I give a relevant example of the Python program that I compiled to produce Fig. (3.11) specifically, even if by selecting the portions of the code that calculate the IC luminosity for a single magnetic field distribution it is possible to reproduce the programs that I created to calculate the graphs in Fig. (3.12)-(3.13). Also, by adding a *for loop* that goes through the possible values of δ, which are represented here specifically by the numpy array d, it can be seen how the IC luminosity changes with δ, thus obtaining the graphs of Fig. (3.8) through Fig. (3.10). I do not report all the different programs that I used to obtain the graphs above mentioned since the code written in this Appendix can function as a summary of the other programs, that can be obtained easily with some modifications.
In the code written below every sentence preceded by the symbol # is not part of the code itself but a comment to it.

```
import numpy as np
import matplotlib.pyplot as plt
from matplotlib import cm
import scipy.constants as sp
from scipy import special
from scipy.stats import maxwell
import astropy.constants as ap
from astropy.coordinates import Distance
from astropy.cosmology import FlatLambdaCDM
import math
mpl_toolkits.mplot3d import Axes3D
from matplotlib.collections import LineCollection

# Definition of physical constants
```

```
Pi=sp.pi
c=ap.c.cgs.value
c_nc=ap.c.value
G=ap.G.cgs.value
e=ap.e.value*2.998e9 #in cgs
h=ap.h.cgs.value
h_nc=ap.h.value
k_b=ap.k_B.cgs.value
m_e=ap.m_e.cgs.value
m_p=ap.m_p.cgs.value
s_T=ap.sigma_T.cgs.value
s_sb=ap.sigma_sb.cgs.value
L_sun=ap.L_sun.cgs.value
T_cmb=2.73
r0=sp.physical_constants[’classical electron radius’][0]*100
cosmo = FlatLambdaCDM(H0=72, Om0=0.258)

# Finished the definition of the constants

# Definition of parameters used during the production of the graph

d=np.arange(0.0, 5.5, 0.5) #values of delta from 0 to 5.5
Fd=np.array([3.48, 3.00, 3.20, 3.91, 5.25, 7.57, 11.54, 18.44, 30.62, 52.57, 92.90])
#numerical factor depending on the value of delta
z_1=1.072735 #z_1 = 1+z
dl=Distance(z=z_1-1, unit=’Mpc’, cosmology=cosmo).value*3.086e24 # luminosity
distance (from Mpc to cm)
bg_IC =1.4553e-14*4*Pi*dl*dl #IC limit in erg/s in the band 0.1-2.4 keV
keV_erg = 1.60218e-9 #conversion factor from keV to erg
en = np.linspace(0.1, 2.4, 1000) #energy range from 0.1 to 2.4 keV (to put in erg)
nu=140e6 #frequency of observation of the bridge of 140 MHz
J_erg = 1e7 #conversion factor from J to erg
L140 = 1e25*J_erg #Synchrotron luminosity as observed by Govoni 2019 in erg/s/Hz
at 140 MHz
B0=np.linspace(0.1e-6, 4e-6, 1000) #B_0 in G
normalization=1.38e-34 #normalization factor in erg/s/cmˆ 2
fill=np.array([0.01, 0.10, 1.00]) #filling factor
N=1000 #number used to define the step of integration
nu_i=0.1 #initial frequence of the energy band in keV
nu_f=2.4 #final frequence of the energy band in keV
delta=d[7] #delta=3.5
n_value=2.0 #number that defines the range on the rectangle magnetic field distri-
bution

g_factor=np.empty([len(d)]) #function composed of multiple gamma functions
```

```
for i, s_d in enumerate(d):
    g_factor[i] = special.gamma(s_d/4+19/12) * special.gamma(s_d/4-1/12) * special.gamma(s_d/4+5/4)/special.gamma(s_d/4+7/4)

# Finished the definition of the parameters


n = len(d)
colors = plt.cm.jet(np.linspace(0,1,n)) # colormap
fig, ax = plt.subplots(2, 1)

Ke=np.empty([len(B0)]) #volume constant
F_syn_part=np.empty([len(B0)]) #array of partial values of synchrotron flux used
during integration
F_syn_box=np.empty([len(B0)]) #array of partial values of synchrotron flux used
during integration
F_syn=np.empty([len(B0)]) #synchrotron flux
F_IC=np.empty([len(B0)]) #IC luminosity


#Production of the higher graph

#IC luminosity from a maxwellian distribution

B=B0/(N*B0)*1e-6 #starting value for the integration
sigma=np.sqrt((3*Pi-8)/2)*B0 #dispertion on B
for i in range(0, 10*N-1):
    F_syn_part=0
    pdf_max = np.sqrt(2/Pi) * np.float_power(B, 2) * np.exp(-np.float_power(B,
2)/(2*sigma*sigma))/(sigma*sigma*sigma) #maxwellian PDF
    deltaB=B0/(N*B0)*1e-6 #step of integration
    F_syn_part=np.sqrt(3*Pi)/2*(e**3)/(m_e*(delta+1)*c**2)*np.float_power(2*Pi*m_e*c
/(3*e), -(delta-1)/2) * np.float_power(B, (delta+1)/2) * g_factor[7] * np.float_power(nu,
-(delta-1)/2)
    F_syn_box += F_syn_part*pdf_max*deltaB
    B=(B0/(N*B0)+B0/(N*B0)*(i+1))*1e-6
B_i=B0/(N*B0)*1e-6
cdf_max=special.erf(B/(np.sqrt(2)*sigma))-np.sqrt(2/Pi)*B * np.exp( -np.float_power(
B, 2)/(2*sigma*sigma))/sigma-special.erf(B_i/(np.sqrt(2)*sigma))+np.sqrt(2/Pi)*B_i
* np.exp( -np.float_power(B_i, 2)/(2*sigma*sigma))/sigma #maxwellian CDF
F_syn = F_syn_box/cdf_max
Ke=L140/(F_syn)
F_IC=(r0**2)/(Pi*(c**2)*(h/(2*Pi))**3)*Ke*np.float_power(k_b*T_cmb*z_1, (delta+5)/2)
* Fd[7] * (2/(3-delta))*(np.float_power(nu_f*keV_erg, (3-delta)/2) -np.float_power(
nu_i*keV_erg, (3-delta)/2))
ax[0].plot(B0*1e6, F_IC, linestyle=’–’, label=’maxwellian’)
```

```
ax[0].set_yscale(’log’)
ax[0].plot(B0*1e6, [bg_IC]*len(B0))
ax[0].grid()
ax[0].set_title(r’$L_IC$ vs. $B$’)
ax[0].set_xlabel(r’$B_0$ ($\mu$G)’)
ax[0].set_ylabel(’$L_IC$ (erg/s)’)


#IC luminosity from a uniform distribution

F_syn=0
F_IC=0
Ke=0

F_syn = np.sqrt(3*Pi)/2*(e**3)/(m_e*(delta+1)*c**2)*np.float_power(2*Pi*m_e*c
/(3*e), -(delta-1)/2)*np.float_power(B0, (delta+1)/2)*g_factor[7]*np.float_power(nu,
-(delta-1)/2)
Ke = L140/F_syn
F_IC = (r0**2)/(Pi*(c**2)*(h/(2*Pi))**3)*Ke * np.float_power( k_b*T_cmb*z_1,
(delta+5)/2) * Fd[7]*(2/(3-delta)) * (np.float_power(nu_f*keV_erg, (3-delta)/2) -
np.float_power(nu_i*keV_erg, (3-delta)/2))
ax[0].plot(B0*1e6, F_IC, linestyle=’-’, label=’uniform’)
ax[0].set_yscale(’log’)
ax[0].grid()
ax[0].set_title(r’$L_IC$ vs. $B$’)
ax[0].set_xlabel(r’$B_0$ ($\mu$G)’)
ax[0].set_ylabel(’$L_IC$ (erg/s)’)


#IC luminosity from a rectangle distribution

F_syn=0
F_syn_part=0
F_syn_box=0
F_IC=0
Ke=0
B=B0-B0/n_value #starting value of B for the integration

for i in range(0, 2*N+1):
    F_syn_part=0
    F_syn_part=np.sqrt(3*Pi)/2*(e**3)/(m_e*(delta+1)*c**2)*np.float_power(2*Pi*m_e*c
/(3*e), -(delta-1)/2) * np.float_power(B, (delta+1)/2) * g_factor[7] * np.float_power(nu,
-(delta-1)/2)
    F_syn_box += F_syn_part*B0/(N*n_value)
    B=B0-B0/n_value+B0/(n_value*N)*i
B_i=B0-B0/n_value
```

```
F_syn=F_syn_box/(B-B_i)
Ke=L140/F_syn
F_IC=(r0**2)/(Pi*(c**2)*(h/(2*Pi))**3) * Ke * np.float_power( k_b*T_cmb*z_1,
(delta+5)/2) * Fd[7]*(2/(3-delta)) * (np.float_power(nu_f*keV_erg, (3-delta)/2) -
np.float_power( nu_i*keV_erg, (3-delta)/2))
ax[0].plot(B0*1e6, F_IC, linestyle=’:’, label=’rectangle’)
ax[0].set_yscale(’log’)
ax[0].grid()
ax[0].set_title(r’$L_IC$ vs. $B$’)
ax[0].set_xlabel(r’$B_0$ ($\mu$G)’)
ax[0].set_ylabel(’$L_IC$ (erg/s)’)
ax[0].legend(title=’Distribution of B’)


#Production of the lower graph

#IC luminosity from a maxwellian distribution and changing for the filling factor

n = len(fill)
colors = plt.cm.jet(np.linspace(0,1,n)) # colormap

for j, f in enumerate(fill):
    F_IC=0
    F_syn_box=0
    F_syn=0
    B=B0/(N*B0)*1e-6
    for i in range(0, 10*N-1):
        F_syn_part=0
        pdf_max = np.sqrt(2/Pi) * np.float_power(B, 2) * np.exp(-np.float_power(B,
2)/(2*sigma*sigma))/(sigma*sigma*sigma)
        deltaB=B0/(N*B0)*1e-6
        F_syn_part = np.sqrt(3*Pi)*f/2*(e**3)/(m_e*(delta+1)*c**2) * np.float_power(
2*Pi*m_e*c/(3*e), -(delta-1)/2) * np.float_power(B, (delta+1)/2) * g_factor[7] *
np.float_power(nu, -(delta-1)/2)
        F_syn_box += F_syn_part*pdf_max*deltaB
        B=(B0/(N*B0)+B0/(B0*N)*(i+1))*1e-6
    B_i=B0/(N*B0)*1e-6
    cdf_max=special.erf(B/(np.sqrt(2)*sigma))-np.sqrt(2/Pi)*B*np.exp(-np.float_power(
B, 2)/(2*sigma*sigma))/sigma-special.erf(B_i/(np.sqrt(2)*sigma))+np.sqrt(2/Pi)*B_i
* np.exp( -np.float_power(B_i, 2)/(2*sigma*sigma))/sigma
    F_syn = F_syn_box/cdf_max
    Ke=L140/(F_syn)
    F_IC=(r0**2)/(Pi*(c**2)*(h/(2*Pi))**3)*Ke * np.float_power(k_b*T_cmb*z_1,
(delta+5)/2) * Fd[7] * (2/(3-delta)) * (np.float_power(nu_f*keV_erg, (3-delta)/2)-
np.float_power(nu_i*keV_erg, (3-delta)/2))
```

```
    ax[1].plot(B0*1e6, F_IC, linestyle=’–’, label=’maxwell’, color=colors[j])
ax[1].plot(B0*1e6, [bg_IC]*len(B0))


#IC luminosity from a uniform distribution and changing for the
filling factor

for j, f in enumerate(fill):
    F_syn = np.sqrt(3*Pi)*f/2*(e**3)/(m_e*(delta+1)*c**2)*np.float_power(2*Pi*m_e*c /(3*e), -(delta-1)/2) * np.float_power(B0, (delta+1)/2) * g_factor[7] * np.float_power(nu, -(delta-1)/2)
    Ke = L140/F_syn
    F_IC = (r0**2)/(Pi*(c**2)*(h/(2*Pi))**3)*Ke * np.float_power(k_b*T_cmb*z_1, (delta+5)/2) * Fd[7]*(2/(3-delta)) * (np.float_power(nu_f*keV_erg, (3-delta)/2) - np.float_power( nu_i*keV_erg, (3-delta)/2))
    ax[1].plot(B0*1e6, F_IC, linestyle=’-’, label=’uniform’, color=colors[j])


#IC luminosity from a rectangle distribution and changing for the filling factor

for j, f in enumerate(fill):
    F_IC=0
    F_syn_box=0
    F_syn=0
    B=B0-B0/n_value
    for i in range(0, 2*N+1):
        F_syn_part=0
        F_syn_part=np.sqrt(3*Pi)*f/2*(e**3)/(m_e*(delta+1)*c**2) * np.float_power( 2*Pi*m_e*c/(3*e), -(delta-1)/2) * np.float_power(B, (delta+1)/2) * g_factor[7] * np.float_power(nu, -(delta-1)/2)
        F_syn_box += F_syn_part*B0/(N*n_value)
        B=B0-B0/n_value+B0/(n_value*N)*i
    B_i=B0-B0/n_value
    F_syn=F_syn_box/(B-B_i)
    Ke=L140/F_syn
    F_IC=(r0**2)/(Pi*(c**2)*(h/(2*Pi))**3)*Ke * np.float_power(k_b*T_cmb*z_1, (delta+5)/2) * Fd[7]*(2/(3-delta)) * (np.float_power(nu_f*keV_erg, (3-delta)/2) - np.float_power(nu_i*keV_erg, (3-delta)/2))
    ax[1].plot(B0*1e6, F_IC, linestyle=’:’, label=’rectangle’, color=colors[j])
ax[1].set_yscale(’log’)
ax[1].grid()
ax[1].set_xlabel(r’$B_0$ ($\mu$G)’)
ax[1].set_ylabel(r’$L_IC$ (erg/s)’)
ax[1].legend(fill, title=’Filling factor’)
plt.show()
```

Appendix B

Python code to infer critical magnetic fields

In this Appendix, I show the Python program that I created to produce the Fig. (3.14)-(3.15), that manifest what is the interaction between the critical value of magnetic field B_{crit}, for a certain distribution of magnetic fields, and the filling factor. The values of B_{crit} in the two figures differ because of the chosen value of δ, so to switch between the programs used to produce Fig. (3.14) and Fig. (3.15) it is only necessary to change the value of *delta*, and the corresponding Fd, to the desired one.
In the program written below, sentences that are comments to the text are preceded by the symbol #.

```
import numpy as np
import matplotlib.pyplot as plt
from matplotlib import cm
import scipy.constants as sp
from scipy import special
from scipy.stats import maxwell
import astropy.constants as ap
from astropy.coordinates import Distance
from astropy.cosmology import FlatLambdaCDM
import math
mpl_toolkits.mplot3d import Axes3D
from matplotlib.collections import LineCollection

# Definition of physical constants

Pi=sp.pi
c=ap.c.cgs.value
```

```
c_nc=ap.c.value
G=ap.G.cgs.value
e=ap.e.value*2.998e9 #in cgs
h=ap.h.cgs.value
h_nc=ap.h.value
k_b=ap.k_B.cgs.value
m_e=ap.m_e.cgs.value
m_p=ap.m_p.cgs.value
s_T=ap.sigma_T.cgs.value
s_sb=ap.sigma_sb.cgs.value
L_sun=ap.L_sun.cgs.value
T_cmb=2.73
r0=sp.physical_constants[’classical electron radius’][0]*100
cosmo = FlatLambdaCDM(H0=72, Om0=0.258)

# Finished the definition of the constants

# Definition of parameters used during the production of the graph

d=np.arange(0.0, 5.5, 0.5) #values of delta from 0 to 5.5
Fd=np.array([3.48, 3.00, 3.20, 3.91, 5.25, 7.57, 11.54, 18.44, 30.62, 52.57, 92.90])
#numerical factor depending on the value of delta
z_1=1.072735 #z_1 = 1+z
dl=Distance(z=z_1-1, unit=’Mpc’, cosmology=cosmo).value*3.086e24 # luminosity distance (from Mpc to cm)
bg_IC =1.4553e-14*4*Pi*dl*dl #IC limit in erg/s in the band 0.1-2.4 keV
keV_erg = 1.60218e-9 #conversion factor from keV to erg
en = np.linspace(0.1, 2.4, 1000) #energy range from 0.1 to 2.4 keV (to put in erg)
nu=140e6 #frequency of observation of the bridge of 140 MHz
J_erg = 1e7 #conversion factor from J to erg
L140 = 1e25*J_erg #Synchrotron luminosity as observed by Govoni 2019 in erg/s/Hz at 140 MHz
B0=np.linspace(0.1e-6, 30e-6, 1000) #B_0 in G
normalization=1.38e-34 #normalization factor in erg/s/cmˆ 2
fill=np.linspace(0.01, 1.00, 10) #filling factor
N=1000 #number used to define the step of integration
nu_i=0.1 #initial frequence of the energy band in keV
nu_f=2.4 #final frequence of the energy band in keV
delta=d[7] #delta=3.5
n_value=2.0 #number that defines the range on the rectangle magnetic field distribution

g_factor=np.empty([len(d)]) #function composed of multiple gamma functions
for i, s_d in enumerate(d):
    g_factor[i] = special.gamma(s_d/4+19/12) * special.gamma(s_d/4-1/12) * special.gamma(s_d/4+5/4)/special.gamma(s_d/4+7/4)
```

```
# Finished the definition of the parameters


F_IC=np.empty([len(B0)]) # IC luminosity
B_crit_max=np.empty([len(fill)]) #array of critical B from the maxwellian distribution
B_crit_uni=np.empty([len(fill)]) #array of critical B from the uniform distribution
B_crit_box=np.empty([len(fill)]) #array of critical B from the rectangle distribution

# Production of the profiles of B_crit as the filling factor changes

# B_crit from the uniform distribution

for j, f in enumerate(fill):
    F_syn = np.sqrt(3*Pi)*f/2*(e**3)/(m_e*(delta+1)*c**2)*np.float_power( 2*Pi*m_e*c /(3*e), -(delta-1)/2) * np.float_power(B0, (delta+1)/2) * g_factor[7] * np.float_power(nu, -(delta-1)/2)
    Ke = L140/F_syn
    F_IC = (r0**2)/(Pi*(c**2)*(h/(2*Pi))**3)*Ke * np.float_power(k_b*T_cmb*z_1, (delta+5)/2) * Fd[7]*(2/(3-delta)) * (np.float_power(nu_f*keV_erg, (3-delta)/2) - np.float_power(nu_i*keV_erg, (3-delta)/2))
    diff=(F_IC-bg_IC)*(F_IC-bg_IC) #to find what is the value of B that more closely reproduces the IC observational limit
    crit=diff.argmin() #to obtain the index of the array element corresponding to B_crit
    B_crit_uni[j]=B0[crit]*1e6

# B_crit from the rectangle distribution

for j, f in enumerate(fill):
    F_syn_box=0
    B=B0-B0/n_value #starting value for the integration
    for i in range(0, 2*N+1):
        F_syn_part=np.sqrt(3*Pi)*f/2*(e**3)/(m_e*(delta+1)*c**2) * np.float_power( 2*Pi*m_e*c/(3*e), -(delta-1)/2) * np.float_power(B, (delta+1)/2) * g_factor[7] * np.float_power(nu, -(delta-1)/2)
        F_syn_box += F_syn_part*B0/(N*n_value)
        B=B0-B0/n_value+B0/(n_value*N)*i
    B_i=B0-B0/n_value
    F_syn=F_syn_box/(B-B_i)
    Ke=L140/F_syn
    F_IC=(r0**2)/(Pi*(c**2)*(h/(2*Pi))**3)*Ke * np.float_power(k_b*T_cmb*z_1, (delta+5)/2) * Fd[7]*(2/(3-delta)) * (np.float_power(nu_f*keV_erg, (3-delta)/2) - np.float_power(nu_i*keV_erg, (3-delta)/2))
    diff=(F_IC-bg_IC)*(F_IC-bg_IC)
```

```
    crit=diff.argmin()
    B_crit_box[j]=B0[crit]*1e6

# B_crit from the maxwellian distribution

for j, f in enumerate(fill):
    F_syn_box=0
    B=B0/(N*B0)*1e-6 #starting value for the integration
    sigma=np.sqrt((3*Pi-8)/2)*B0 #dispersion of B
    for i in range(0, 100*N-1):
        pdf_max = np.sqrt(2/Pi)*np.float_power(B, 2) * np.exp( -np.float_power(B, 2)/(2*sigma*sigma))/(sigma*sigma*sigma) #maxwellian PDF
        deltaB=B0/(N*B0)*1e-6 #step of the integration
        F_syn_part=np.sqrt(3*Pi)*f/2*(e**3)/(m_e*(delta+1)*c**2) * np.float_power( 2*Pi*m_e*c/(3*e), -(delta-1)/2) * np.float_power(B, (delta+1)/2) * g_factor[7] * np.float_power(nu, -(delta-1)/2)
        F_syn_box += F_syn_part*pdf_max*deltaB
        B=(B0/(N*B0)+B0/(B0*N)*(i+1))*1e-6
    B_i=B0/(N*B0)*1e-6
    cdf_max=special.erf(B/(np.sqrt(2)*sigma)) -np.sqrt(2/Pi)*B*np.exp( -np.float_power(B, 2)/(2*sigma*sigma))/sigma -special.erf(B_i/(np.sqrt(2)*sigma))+np.sqrt(2/Pi)*B_i*np.exp( -np.float_power(B_i, 2)/(2*sigma*sigma))/sigma #maxwellian CDF
    F_syn = F_syn_box/cdf_max
    Ke=L140/(F_syn)
    F_IC=(r0**2)/(Pi*(c**2)*(h/(2*Pi))**3)*Ke * np.float_power(k_b*T_cmb*z_1, (delta+5)/2) * Fd[7]*(2/(3-delta)) * (np.float_power(nu_f*keV_erg, (3-delta)/2) - np.float_power(nu_i*keV_erg, (3-delta)/2))
    diff=(F_IC-bg_IC)*(F_IC-bg_IC)
    crit=diff.argmin()
    B_crit_max[j]=B0[crit]*1e6


plt.plot(fill, B_crit_uni, label=’uniform’, linestyle=’-’)
plt.plot(fill, B_crit_box, label=’box’, linestyle=’:’)
plt.plot(fill, B_crit_max, label=’max’, linestyle=’–’)
plt.plot(fill, [8.0]*len(fill)) #limit on B due to the equilibrium between magnetic and thermal pressure
plt.plot(fill, [0.5]*len(fill)) #limit on B from Brunetti and Vazza 2020
plt.plot(fill, [0.2]*len(fill)) #limit on B from Govoni and al. 2019
plt.xlabel(’Filling factor’)
plt.ylabel(’$B_crit$’)
plt.grid()
plt.legend(title=’Distribution of B’)
plt.show()
```

Bibliography

E. Fermi (Apr. 1949). “On the Origin of the Cosmic Radiation”. In: *Physical Review.*

R. Kulsrud and W. P. Pearce (May 1969). “The effect of wave-particle interactions on the propagation of cosmic rays”. In: *Astrophysical Journal.*

G. R. Blumenthal and R. J. Gould (Apr. 1970). “Bremsstrahlung, Synchrotron Radiation, and Compton Scattering of High-Energy Electrons Traversing Dilute Gases”. In: *Reviews of Modern Physics.*

G. B. Rybicki and A. P. Lightman (1985). *Radiative processes in Astrophysics.* Wiley-VCH.

P. C. Tribble (Jan. 1991). “Depolarization of extended radio sources by a foreground Faraday screen”. In: *Monthly Notices of the Royal Astronomical Society.*

F. Govoni and L. Feretti (Oct. 2004). “Magnetic fields in Clusters of Galaxies”. In: *International Journal of Modern Physics.*

G. Brunetti and al. (Oct. 2004). “Alfvénic reacceleration of relativistic particles in galaxy clusters: MHD waves, leptons and hadrons”. In: *Monthly Notices of the Royal Astronomical Society.*

G. Brunetti and A. Lazarian (June 2007). “Compressible Turbulence in Galaxy Clusters: Physics and Stochastic Particle Re-acceleration”. In: *Monthly Notices of the Royal Astronomical Society.*

J. Binney and S. Tremaine (2008). *Galactic dynamics: Second Edition.* Princeton University Press.

W. Hanlon (2008). *Cosmic ray spectra of various experiments.* URL: `https://web.physics.utah.edu/~whanlon/spectrum.html`.

M. S. Longair (2011). *High Energy Astrophysics.* Cambridge University Press.

Planck Collaboration and al. (Aug. 2012). “Planck intermediate results. VIII. Filaments between interacting clusters”. In: *Astrophysics & Astronomy.*

D. Caprioli and A. Spitkovsky (Feb. 2014a). “Simulations of ion acceleration at non-relativistic shocks. I. acceleration efficiency”. In: *Astrophysical Journal.*

— (Oct. 2014b). “Simulations of ion acceleration at non-relativistic shocks. III. acceleration efficiency”. In: *Astrophysical Journal.*

G. Brunetti and T. W. Jones (Jan. 2014). “Cosmic rays in galaxy clusters and their non-thermal emission”. In: *International Journal of Modern Physics D.*

G. Brunetti (2016). “The challenge of turbulent acceleration of relativistic particles in the intra-cluster medium”. In: *Plasma Physics and Controlled Fusion.*

H. Akamatsu, Y. Fujita and al. (Apr. 2017). “Properties of the cosmological filament between two clusters: A possible detection of a large-scale accretion shock by Suzaku”. In: *Astronomy & Astrophysics.*

R. Aloisio (July 2017). “Acceleration and propagation of ultra highenergy cosmic rays”. In: *Progress of Theoretical and Experimental Physics*.

A. de Graaff and al. (Apr. 2019). “Probing the missing baryons with the Sunyaev-Zel’dovich effect from filaments”. In: *Astronomy & Astrophysics*.

C. Gheller and F. Vazza (June 2019). “A survey of the thermal and non-thermal properties of cosmic filaments”. In: *Monthly Notices of the Royal Astronomical Society*.

F. Govoni and al. (2019). “A radio ridge connecting two galaxy clusters in a filament of the cosmic web”. In: *Science*.

L. Ambrogi, R. Zanin and al. (Mar. 2019). “Spectral and morphological study of the gamma radiation of the middle-aged supernova remnant HB 21”. In: *Astronomy & Astrophysics*.

M. Murgia and al. (Sept. 2019). “Magnetic Fields and Faraday Rotation in Clusters of Galaxies”. In: *Astronomy & Astrophysics*.

R. J. van Weeren, F. de Gasperin and al. (Jan. 2019). “Diffuse Radio Emission from Galaxy Clusters”. In: *Space Science Reviews*.

A. Botteon, R. J. van Weeren and al. (Dec. 2020). “A giant radio bridge connecting two galaxy clusters in Abell 1758”. In: *Monthly Notices of the Royal Astronomical Society*.

A. Cimatti F. Fraternali, C. Nipoti (2020). *Introduction to galaxy formation and evolution: from primordial gas to present day galaxies*. Cambridge University Press.

G. Brunetti and F. Vazza (Jan. 2020). “Second order Fermi reacceleration mechanisms and large scale synchrotron radio emission in intra-cluster bridges”. In: *Astronomy & Astrophysics*.

H. Tanimura, N. Aghanim and al. (Nov. 2020). “First detection of stacked X-ray emission from cosmic web filaments”. In: *Astronomy & Astrophysics*.

F. Vazza and al. (Nov. 2021). “Magnetogenesis and the Cosmic Web: a joint challenge for radio observations and numerical simulations”. In: *MDPI*.

T. Vernstrom, G. Heald and al. (Aug. 2021). “Discovery of Magnetic Fields Along Stacked Cosmic Filaments as Revealed by Radio and X-Ray Emission”. In: *Monthly Notices of the Royal Astronomical Society*.

A. Bonafede and G. Brunetti (Mar. 2022). “The Coma cluster at LOFAR frequencies II: the halo, relic, and a new accretion relic”. In: *Astrophysical Journal*.

A. D. Hincks and al. (Mar. 2022). “A high-resolution view of the filament of gas between Abell 399 and Abell 401 from the Atacama Cosmology Telescope and MUSTANG-2”. In: *Monthly Notices of the Royal Astronomical Society*.

C. D. Nunhokee, G. Bernardi and al. (Feb. 2022). “Radio multifrequency observations of galaxy clusters. The Abell 399-401 pair”. In: *Monthly Notices of the Royal Astronomical Society*.

F. Radiconi, V. Vacca and al. (June 2022). “The thermal and non-thermal components within and between galaxy clusters Abell 399 and Abell 401”. In: *Monthly Notices of the Royal Astronomical Society*.

T. Hodgson and al. (May 2022). “Searching for the Synchrotron Cosmic Web Again: A replication attempt”. In: *Astronomical Society of Australia*.